2021

Shape-shifting and instabilities of plates and shells

BOSTON UNIVERSITY

COLLEGE OF ENGINEERING

Dissertation

SHAPE-SHIFTING AND INSTABILITIES OF PLATES AND SHELLS

by

LUCIA STEIN-MONTALVO

B.S., Davidson College, 2015
M.S., Boston University, 2021

Submitted in partial fulfillment of the

requirements for the degree of

Doctor of Philosophy

2021

Approved by

First Reader

Douglas P. Holmes, PhD
Associate Professor of Mechanical Engineering
Associate Professor of Materials Science and Engineering

Second Reader

Harold S. Park, PhD
Professor of Mechanical Engineering
Professor of Materials Science and Engineering

Third Reader

Paul E. Barbone, PhD
Professor of Mechanical Engineering
Professor of Materials Science and Engineering

Fourth Reader

Sheila Russo, PhD
Assistant Professor of Mechanical Engineering
Assistant Professor of Materials Science and Engineering

La duda es uno de los nombres de la inteligencia.
Doubt is one of the names of intelligence. Jorge Luis Borges

Acknowledgments

I would like to express my gratitude to the National Science Foundation (CMMI- CMMI-1824882) for supporting my graduate studies.

To my advisor, Doug: I will never know how my naïve 2016 self got so lucky. Thank you for teaching me to see the big picture, plot the right things, get more data, and tell a story. Mostly, thank you for being so exceptionally caring.

I am grateful for the mentorship and warmth of Gwennou Coupier and Catherine Quilliet, and for the support and guidance of my committee members: Harold Park and Sheila Russo, and Paul Barbone, whose encouragement changed the course of my PhD.

Thank you to these MOSSers and dear friends: Matteo Pezzulla, whose patience and kindness pulled me through my early days. Xin Jiang, Yi Yang, Arman Guerra, Casey Lautzenhizer, Martin Brandenbourger, Paul Costa, and Jay Schunter. I am so grateful for the generosity, joy, brightness, thoughtfulness, perspective, adventures, and philosophy (respectively). Thank you to supportive friends in the Fluid Lab, and the lively crew at LIPhy.

Thank you endlessly to my family. In particular: Mom, Dad and Linda for constant support; my best friend and, luckily, sister, Sofie; my impressive and loving siblings Henry and Francesca; Jane and Adam, Lee, and Annie and Becca.

SHAPE-SHIFTING AND INSTABILITIES OF PLATES AND SHELLS

LUCIA STEIN-MONTALVO

Boston University, College of Engineering, 2021

Major Professor: Douglas P. Holmes, PhD
Associate Professor of Mechanical Engineering
Associate Professor of Materials Science and Engineering

ABSTRACT

Slender structures like plates and shells – for which at least one dimension is much smaller than the others – are lightweight, flexible, and offer considerable strength with little material. As such, these structures are abundant in nature (e.g. flower petals, eggshells, and blood vessels) and design (e.g. bridge decks, fuel tanks, and soda cans). However, with slenderness comes suceptibility to large and often sudden deformations, which can be wildly nonlinear, as bending is energetically preferable to stretching. Though once considered categorically undesirable, these *instabilities* are often coveted nowadays in the engineering community. They provide mechanical explanations for observations in nature like the wrinkled structure of the brain or the snapping mechanism of the Venus fly trap, and when precisely controlled, enable the design of functional devices like artificial muscles or self-propelling microswimmers. As a prerequisite, these achievements require a thorough understanding of how thin structures “shape-shift" in response to stimuli and confinement. Advancing this fundamental knowledge is the goal of this thesis.

In the first two chapters, we consider the shape-selection of shells and plates that are confined by their environment. The shells are made by *residual swelling* of silicone elas-

tomers, a process that mimics differential growth, and causes initially flat structures to irreversibly morph into curved shapes. Flattening the central region forces further reconfiguration, and the confined shells display multi-lobed buckling patterns. These experiments, finite element (FE) simulations, and a scaling argument reveal that a single geometric confinement parameter predicts the general features of this shape-selection. Next, in experiments and molecular dynamics (MD) simulations, we constrain intrinsically flat sheets in the same manner, so that their center remains flat when we quasi-statically force them through a ring. In the absence of planar confinement, these sheets form a well-studied conical shape (the developable cone or *d-cone*). Our *annular d-cone* buckles circumferentially into patterns that are qualitatively similar to the confined shells, despite the distinct curvatures and loading methods. This is explained by the dominant role of confinement geometry in directing deformation, which we uncover *via* a scaling argument based on the elastic energy. There are also marked differences between the way plates and shells change shape, which we highlight when we investigate the rich dynamics of reconfiguration.

In the final two chapters, we demonstrate how mechanics, geometry, and materials can inform the design of structures that use instabilities to function. We observe in experiments that dynamic loading causes a spherical elastomer shell to buckle at ostensibly subcritical pressures, following a substantial time delay. To explain this, we show that viscoelastic creep deformation lowers the critical load in the same predictable, quantifiable way that a growing defect would in an elastic shell. This work offers a pathway to introduce tunable, time-controlled actuation to existing mechanical actuators, e.g. pneumatic grippers. The final chapter aims at reducing the energy input required for bistable actuators, wherein snap-through instability is typically induced by a stimulus applied to the entire shell. To do so, we combine theory with 1D finite element simulations of spherical caps with a non-homogeneous distribution of stimuli–responsive material. We demonstrate that restricting the active area to the shell boundary allows for a large reduction in its size, while preserving

snap-through behavior. These results are stimulus-agnostic, which we demonstrate with two sets of experiments, using residual swelling of bilayer silicone elastomers as well as a magneto-active elastomer. Our findings elucidate the underlying mechanics, offering an intuitive route to optimal design for efficient snap-through.

Contents

List of Figures

List of Abbreviations

DE	.....	Dielectric elastomer
DMV	.....	Donnell-Mushtari-Vlasov
FE	.....	Finite Element
FEM	.....	Finite Element Method
FvK	.....	Föppl-von Kármán
MD	.....	Molecular Dynamics
MEMS	.....	Micro-electromechanical systems
NEP	.....	Non-Euclidean Plate
PDMS	.....	Polydimethylsiloxane
SLS	.....	Standard Linear Solid
VPS	.....	Vinylpolysiloxane

Chapter 1

Introduction and background

When an elastic body must deform, it will seek to do so in a way that minimizes the total potential energy, which is the elastic strain energy plus the potential from external loads. For slender structures like rods, plates, and shells, wherein at least one dimension is much smaller than the others, the strain energy $\mathcal{U}$ may be quantified as the sum of two terms: one that penalizes stretching, $\mathcal{U}_s$, and one that accounts for the cost of bending, $\mathcal{U}_b$. The stretching energy depends linearly on the the thickness, h, whereas the bending term scales with its cube, h^3 [106]. Thus, if the thickness of a structure is small, the cost of bending is much less that of stretching, i.e. $\mathcal{U}_b \ll \mathcal{U}_s$. As a result, slender structures readily "shape-shift", undergoing large, nonlinear, bending-dominated deformations. Such contortions are cheaper than even small amounts of stretching or compression.

In many cases, the route [188] to an energy-minimizing configuration relies on an *elastic instability*, i.e. a sudden, large change in the deformation, which is disproportionate to the change in the applied force or stimulus. Examples include lateral railway buckling [100], which can occur as heat causes tracks to expand, or the snap-through collapse of masonry arches [19]. The catastrophic potential of these failures has driven engineers for many decades to seek accurate predictions for when an instability will occur. These problems are inherently nonlinear, but linearized approximations often suffice for capturing the critical load or displacement that will cause a structure to lose stability [11].

It is generally more difficult, however, to understand what happens following the onset of instability. In more recent decades, this has become a major goal of the mechanics

community for two primary reasons. First, technological advancements, e.g. in medical imaging, have inspired research aimed at providing mechanical explanations for morphologies in biology and nature. Buckling due to differential growth [60] explains the wrinkled structure of the brain [61] and the rippled edge of a leaf [168, 116, 167] alike. In some pathological cases, understanding the mechanical root of an instability can inform solutions. Circumferential buckling, or “mucosal folding", can constrict multi-layered, tubular biological structures like blood vessels and airways, and has been linked directly to the increased thickness of an inflamed inner wall [193, 201]. Surface tension can even drive pulmonary airways to collapse completely [72] (pulmonary surfactant can prevent this buckling [68]). In other cases, instabilities are advantageous. Snap-through instability is a crucial step of morphogenesis for the optic cup [114] and the Volvox embryo [77]. To capture food, the Venus fly trap [50] and the hummingbird [173] both rely on snapping as well. Helical buckling helps to propel climbing plants against gravity [126], and some bacteria gain motility from flagellar buckling [174].

The increased understanding of these adaptive deformations in nature is largely to thank for inspiring a major paradigm shift among engineers: In recent years, controllable instabilities are often sought out, rather than avoided, in design [78]. This new collective “buckliphilic" [153] mindset has been bolstered by advances in materials science, such as the prevalence of robust, easy-to-prepare [111] soft elastomers, and a flourishing landscape of smart, stimulus-responsive [31] materials [154]. These materials are conducive to reversible deformations, and can often tolerate high strains in doing so, thus enabling the design of devices across scales that rely on instabilities for functionality. Among the many examples are soft robotic actuators [63, 139] and artificial muscles [200], reprogrammable Braille [32], switching optical devices [79], mechanical swimmers [41], self-assembling colloids [158], snapping micro-electromechanical systems (MEMS)-based accelerometers [69], adaptive architectural façades [175], flow– [82, 59] and drag– [179]

control devices, *4D printing* [16, 180], wherein a pre-determined 3D structure forms upon activation from a stimulus, and *mechanical metamaterials* [13, 49], which exhibit tunable properties beyond those of their constituent materials.

These two complementary goals – to *describe* and *prescribe* instabilties – continue to motivate a more complete understanding of their nature. The seemingly limitless design space advances along with our essential understanding of these large, nonlinear deformations, and despite the enormous progress made in recent decades, many questions remain. The primary aim of this thesis is to address some of these unsolved, fundamental problems.

In the following two Chapters, we examine how slender structures respond to external confinement. Because seemingly slight changes to boundary conditions dramatically change the nature of instabilities, this area of research is vast. Particularly for naturally curved shells, very little is understood about the response to external confinement (though the indentation response of positively curved shells is somewhat of an exception [134]). Accordingly, we ask broad questions in Chapter 2: How do shells of diverse intrinsic and extrinsic curvatures respond when their central region is forced to flatten? What happens when some of this in-plane confinement is released? We address these questions primarily with experiments, but also with finite element (FE) simulations. In experiments, we combine planar confinement with *residual swelling* of silicone elastomers, wherein diffusion of free polymer chains leads a structure to morph in response to an evolving natural curvature. Across four types of shells that differ in their extrinsic and intrinsic curvatures, we observe that the general features of shape-selection are surprisingly alike. Each shell buckles periodically, and the number of waves increases with increasing confinement. We explain this robust response with a scaling argument based on the elastic energy, which reveals that the wavenumber is set by a single geometric parameter that compares the overall size of the shell to the length scale of confinement.

Compared to shells, much more is known about how intrinsically flat sheets respond

to external confinement. In particular, extensive theoretical [24, 22] and numerical [117] studies have addressed the geometry [163] and mechanics of the canonical problem in this realm, the developable cone, or *d-cone* [3]. The d-cone emerges when a sheet is pushed into an open cup or cylinder *via* indentation at its center with a sharp point. The structure is so-named because it remains developable (or isometric to the flat sheet; see Appendix A) everywhere except for a small sacrificial region at the tip of the indentor. This an example of *stress-focusing* [194]. The d-cone forms the basis for crumpling, which is relevant to e.g. DNA packing [151] and insect wing folding [65]. Experimental works [27, 26] in this area have been scarce, despite that even in the limited geometric range studied, differences from the idealized theoretical structure are evident. Further, beyond this model conical packing problem, less-ideal scenarios emerge [162] that are not as well-understood. In Chapter 3, we simultaneously address the needs for studies of "perturbed" d-cone configurations, and for thorough experiments in this area. To do so, we constrain sheets to remain centrally flat (as we did for the shells in Chapter 2), thus creating an *annular d-cone*, which exhibits an extreme sensitivity to the added confinement. Our experiment-driven approach is enhanced by molecular dynamics (MD) simulations. Like for the confined shells, the annular d-cone buckles periodically, and we find that the confinement geometry plays a dominant role in dictating shape selection. We also report rich dynamics observed in our quasi-static experiments and simulations, e.g. sequential wave formation and unexpected wrinkling, which separate our confined packing problem both from confined shells and the traditional d-cone.

The next two chapters are aimed at providing a physical basis for mechanics-driven design. In Chapter 4, we study dynamically-loaded, defect-seeded spherical elastomer shells. We observe in experiments that the shells buckle at pressures below the experimentally-determined elastic critical load, often following a significant time delay. Silicone elastomers are popular in mechanics research precisely because they behave elastically in most

settings. However, these materials are inherently viscoelastic, meaning that they exhibit a fluid-like time-dependence under certain loading conditions. Viscoelastic creep deformation explains our findings, and we show that the reduced critical load follows directly from the material properties. We then introduce an analogy, wherein we claim that creep deformation lowers the critical load in the same way a growing defect would in an elastic shell. This leads to intuitive and predictive explanations for both the critical time and deformation at which buckling occurs. Our model relies on easily measurable quantities, and thus offers an accessible path to tunable time-dependence for existing elastomer actuators, e.g. pneumatic grippers. This work simultaneously serves the *creep buckling* [70, 71] community, to which our experiments using full spheres and soft materials are novel.

The aim of the work in Chapter 5 is to reduce the energy input needed for bistable snapping devices. In such devices, e.g. dielectric elastomer (DE) actuators [165], snap-through instability is typically induced by a stimulus applied to an entire shell surface. In this work, we demonstrate that restricting the active area to the shell boundary allows for a large reduction in its size, while preserving snap-through behavior. We do so by combining theory with 1D finite element simulations of spherical caps with a non-homogeneous distribution of stimuli-responsive material. Our findings are stimulus-agnostic, which we demonstrate with two sets of experiments, using residual swelling of bilayer silicone elastomers as well as a magneto-active elastomer. These results elucidate a mechanics-informed route to optimal design for efficient snap-through.

Each of Chapters 2 through 5 of this thesis is a self-contained, slightly modified version of either a peer-reviewed journal publication, or a manuscript intended for publication. Chapter 6 contains concluding remarks, including a brief discussion of possible future directions related to the work herein. Before proceeding, the remainder of this Introduction will provide basic knowledge of the mathematics behind elastic instabilities, and introduce some concepts and theories that we rely on throughout this thesis.

1.1 Elastic instabilities

The principle of minimum potential energy informs the arguments we rely on throughout this thesis, and energy methods [11] can be used to determine elastic stability. In what follows, we present some basic concepts and examples using this approach.

The total potential energy of a system consists of the elastic or internal strain energy and the potential from external loads, i.e. $\mathcal{V} = \mathcal{U}_e + P$. This energy *functional* (a function of functions) graphed as an *energy landscape* may be comprised of various peaks and valleys. A ball traveling on such a surface can rest at the top or bottom of a hill, or on a flat surface, i.e. anywhere there is zero slope. Similar to seeking a stationary first derivative in calculus, we consult the first variation of the potential energy to locate these critical points. If a structure is in equilibrium, the first variation of the total potential energy, evaluated with respect to its degrees of freedom, will equal zero, i.e. $\delta\mathcal{V} = 0$.

Often, we want to know how a system in equilibrium would respond to a perturbation. The first variation gives no information, after all, about which of the three zero-slope landforms the ball rests upon. Such a stability analysis requires that we consider the second variation (analogous to the second derivative, which reveals the concavity of a function).

A positive-definite second variation, i.e. $\delta^2\mathcal{V} > 0$, indicates a stable equilibrium. This corresponds to the ball resting in a valley – after a perturbation, the ball will return to the same position. If $\delta^2\mathcal{V} = 0$, we say that a structure is in neutral equilibrium. In this case, a ball rests on a flat surface, and the energy does not change in response to a perturbation. An unstable equilibrium state corresponds to a negative second variation, $\delta^2\mathcal{V} < 0$. Here, the ball rests on top of a hill – a small nudge causes it to roll off and not return. Instead, it lands in a new configuration.

In elastic structures under conservative loading, instabilities fall into two categories: bifurcation (“buckling", pertinent to Chapters 2, 3, and 4) and limit point (“snapping", Chapter 5). To illustrate their differences, we will briefly study simple, introductory exam-

ples.

1.1.1 Bifurcation (buckling)

The canonical discrete buckling problem is a rigid column of length L with a rotational spring of stiffness k at its base, axially loaded at its free end by a constant force P. Suppose the beam is perfectly straight initially, i.e. its angle of inclination θ is 0 (see Fig. 1·1a). Then the total potential energy is

$$\mathcal{V} = \frac{1}{2}k\theta^2 - LP(1-\cos(\theta)). \tag{1.1}$$

The first variation is taken with respect to θ, the only degree of freedom:

$$\delta\mathcal{V} = k\theta - LP\sin(\theta). \tag{1.2}$$

Setting (1.2) equal to zero and solving for P gives an equilibrium condition

$$P(\theta) = \frac{k}{L}\frac{\theta}{\sin(\theta)}, \tag{1.3}$$

which is plotted in Fig. 1·1b. One solution is $\theta = 0$, (i.e. the column stays perfectly straight) which intersects with the second solution branch, on which θ can be nonzero. Next, we can investigate the stability of the nontrivial solution. The second variation of (1.1) is

$$\delta^2\mathcal{V} = k - LP\cos(\theta). \tag{1.4}$$

Inserting (1.3) into (1.4), we arrive at the expression $\delta^2\mathcal{V} = k - k\theta\cot\theta$ for the equilibrium path, which is positive for all $\theta \neq 0$. Thus, the equilibrium path is stable for all non-zero θ.

We also can find the critical buckling force by setting (1.4) equal to zero:

$$P_c = \frac{k}{L\cos\theta}. \tag{1.5}$$

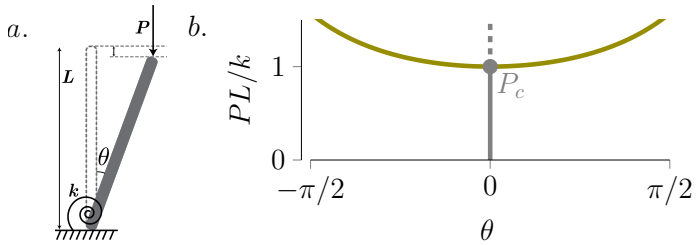

Figure 1·1: *a*. Schematic of the stable, symmetric bifurcation of an axially loaded rigid beam. The initial state is indicated by the dashed gray line. *b*. The equilibrium curves corresponding to a. The load increases but the angle of inclination θ remains zero up to the critical point P_c (equation (1.5), with $\theta = 0$). Here, the beam buckles and stability is transferred to the green bifurcation curve (equation (1.3)).

The interpretation is this: for $P < P_c$, the column will remain vertical. When $P \geq P_c$, the bar breaks symmetry, buckling either right or left. This corresponds to an exchange of stability at the intersection between the two equilibrium paths. After the bifurcation, the load still can increase, and the column will be stable in the buckled state. Because the bifurcation in this example is stable and is symmetric about the critical point, it is categorized as a *stable-symmetric bifurcation*. Two other types of elementary bifurcation instabilities exist [11]. If instead the bifurcation path in Fig. 1·1b decreases symmetrically with displacement, i.e. the bifurcation itself is unstable, the bifurcation is termed *unstable symmetric*. Unlike the stable symmetric bifurcation, this type is very sensitive to imperfection. In addition, frames and shells often exhibit *asymmetric bifurcations*, where, for example, imperfections lead to very different reactions depending on the direction of loading. These are, of course, imperfection-sensitive.

Wrinkling is also a type of buckling instability which appears when a thin, stiff structure is compressed atop the support of a soft substrate traditionally modeled as an elastic (i.e. Winkler) foundation, the latter of which resists deformation [40]. A linear stability analysis leads to the critical buckling stress and the resulting wavelength, each of which are set by the balance between moduli of the plate and the foundation (see Section 2.2). Wrinkles can

also develop as a free elastic sheet is pulled in tension. An analogy between the stretching energy and the energy in an elastic foundation reveals an *effective* foundation stiffness, allowing for a traditional wrinkling analysis to be performed even for free sheets [23].

1.1.2 Limit point (snapping)

A fourth type of elementary instability, which differs notably from bifurcations, is the limit point, or snap-through instability. The von Mises two-bar truss, shown in Fig.1·2a, is the simplest snapping structure. Let each bar have axial stiffness $EA/(L/\cos\alpha)$, where α is the initial inclination angle of the bars and $L/\cos\alpha$ the initial length of each bar. A force P applied to the apex and directed inward will change the inclination angle to θ, and the axial strain of the bars will be $\varepsilon = (L\cos\alpha/\cos\theta - L)/L$, so we can write the total potential energy as:

$$\mathcal{V}(\theta) = \frac{EAL}{cos\theta}\left(\frac{\cos\alpha}{\cos\theta} - 1\right)^2 - PL(\tan\alpha - \tan\theta). \tag{1.6}$$

Setting the first variation, taken with respect to θ, equal to zero and solving for P gives the equilibrium condition:

$$P = 2EA(\sin\theta - \cos\alpha\tan\theta), \tag{1.7}$$

which is plotted in Fig 1·2b.

We can evaluate the stability of the equilibrium states by substituting (1.7) into the second variation:

$$\delta^2\mathcal{V} = \frac{2EAL}{\cos^4\theta}(\cos\theta - \cos^3\alpha). \tag{1.8}$$

From the plot in Fig. 1·2c, we see that for $-\theta_o \leq \theta \leq \theta_o$ the truss is unstable, where $\cos\theta_o = (\cos\alpha)^{1/3}$.

Unsurprisingly, continuous and more complex structures than the examples presented in this section can present nonlinear equations with more degrees of freedom (see Section 1.2), and approximations are often needed. Variational methods are common, as are various numerical techniques, i.e. the Rayleigh-Ritz method [11]. Linearizing (i.e. discarding

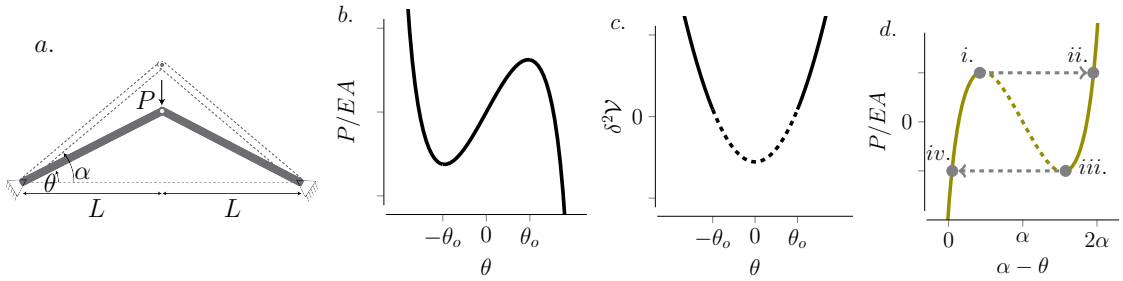

Figure 1·2: *a*. Schematic of a von Mises truss loaded at its center. The initial state is indicated by the dashed gray outline. *b*. Normalized equilibrium curve from (1.7). *c*. The second variation of the total energy from (1.8). The equilibrium path b. is unstable when $\delta^2\mathcal{V}$ is negative (dashed portion of curve, with $\cos\theta_o = (\cos\alpha)^{1/3}$). *d*. Normalized force versus rotation. When *P* increases from 0 to the limit point *i*., the truss snaps to the nearest stable point on the equilibrium path, *ii*. Stability is lost again upon unloading to *iii*., when the structure snaps to *iv*.

higher-order terms) is also a useful tool, but this raises an important distinction between bifurcations (Fig. 1·1b) and limit point instabilities. From Fig. 1·2b, we observe that only one equilibrium path exists for systems that undergo limit point instabilities. When stability is lost (Fig. 1·2d,*i*&*iii*), the nearest equilibrium point that can sustain the same load is far away (Fig. 1·2d,ii.&iv.). Thus, the force increases up to a critical point, then the structure snaps abruptly to the next state. For buckling, we saw that when stability is lost, the closest, stable equilibrium state is infinitesimally close the state just before the instability. Because of this difference, bifurcations permit a linear stability analysis, but limit point instabilities do not.

1.2 Shell & plate theories

In thin structures, relatively small provocation can lead to large deformations and instabilities. To simplify the highly nonlinear problems that result, reduced order models have been developed, approximating three-dimensional elastic shells and plates as two-dimensional. This dimensional reduction relies on several key assumptions: That motion follows the

mid-plane, that straight lines normal to the midplane remain straight and normal to the midplane, and that the thickness h remains constant. The latter two are known as the Kirchhoff-Love assumptions.

Under these assumptions, reduced-order shell theories take on a common form: the elastic strain energy is additively split into a stretching term, $\mathcal{U}_s$, which accounts for extension or compression of the midsurface and scales with h, and a bending term, $\mathcal{U}_b$, which accounts for changes in curvature, and depends on h^3. In the chapters that follow, we will often refer to Koiter's widely accepted shell theory, which we will now introduce.

1.2.1 Koiter shell theory

Assuming elastic, homogenous, and isotropic materials (i.e. the material model is Kirchhoff-St. Venant), the strain energy in a shell is [106]:

$$\mathcal{U}_K = \underbrace{\frac{Y}{2}\int \left[(1-\nu)\gamma^{\alpha\beta}\gamma_{\alpha\beta}+\nu(\gamma^{\alpha}_{\alpha})^2\right]d\omega}_{\text{stretching}} + \underbrace{\frac{B}{2}\int \left[(1-\nu)\rho^{\alpha\beta}\rho_{\alpha\beta}+\nu(\rho^{\alpha}_{\alpha})^2\right]d\omega}_{\text{bending}}. \tag{1.9}$$

Here, Y is the stretching rigidity and B is the bending rigidity. For homogenous shells, these are given by $Y = \frac{Eh}{1-\nu^2}$ and $B = \frac{Eh^3}{12(1-\nu^2)}$, respectively, with Young's modulus E and Poisson's ratio ν. The midsurface strain tensor is $\gamma_{\alpha\beta} = \frac{1}{2}(a_{\alpha\beta} - \mathring{a}_{\alpha\beta})$, and the curvature strains are quantified by the tensor $\rho_{\alpha\beta} = b_{\alpha\beta} - \mathring{b}_{\alpha\beta}$. The over circle refers to the initial configuration, whereas no subscript denotes the current (deformed) state. This formulation relies on concepts from differential geometry [138, 135], which are discussed in Appendix A. Briefly, **a** is the *first fundamental form* or 2D *metric tensor*, which quantifies changes in length, whereas **b** is the *second fundamental form* or *curvature tensor*, which accounts for curvature changes. The indices $\alpha, \beta \in \{1,2\}$. Lowered and raised indices, repsectively, refer to the covariant and contravariant quantities, and Einstein's summation convention is employed, i.e. we sum over repeated indices. Since the shell is approximated as two-dimensional, each term in (1.9) contains the square of two principal scalar invariants, albeit

perhaps in a somewhat veiled form. Koiter's model is suitable for large displacements and rotation (i.e. *geometrically* nonlinear problems) but small strains (*elastically* linear).

To make these equations more tractable, additional assumptions are often used. For example, in many instances, it is reasonable to neglect the stretching energy, since isometries are so heavily preferred for thin structures. For example, this concept applies to the residual swelling bilayers [146] we use in Chapter 2, or the d-cone [3], which is relevant to Chapter 3. Better yet, symmetries can enable further dimensional reduction, e.g. to the 1D *elastica*, or an Euler column [24, 5]. In Chapters 2 & 3, we rely on Koiter's equations in a scaling sense, meaning that we make significant approximations in order to discern the key mechanisms driving deformation. Another simplification of Eq. (5.13) leads to the commonly used Föppl-von Kármán plate theory, discussed below.

1.2.2 The Föppl-von Kármán approximation for plates

For thin plates, the in-plane strain component of the elastic energy, $\gamma_{\alpha\beta}$, can be simplified by neglecting higher-order terms correspdoing to in-plane stretching (while retaining those that capture transverse deflection). With this small-stretching assumption, a variational approach (see e.g. Refs. [109, 5]) leads to the coupled, nonlinear partial differential equations known as the Föppl-von Kármán (FvK) equations, which minimize the elastic energy when satisfied:

$$B\nabla^4 w - h\sigma_{\alpha\beta} w_{,\alpha\beta} = 0 \tag{1.10a}$$

$$\sigma_{\alpha\beta,\beta} = 0, \tag{1.10b}$$

where ∇^4 is the biharmonic operator, w is the out-of-plane deflection, $\sigma_{\alpha\beta}$ is the Cauchy stress tensor, and the comma denotes partial differentiation, i.e. $f_{,1}$ is the partial derivative of the function f with respect to the coordinate x_1.

If the in-plane components of an external distributed force are assumed to be zero, the stress tensor can be replaced by a single scalar function using the Airy potential χ, defined

such that

$$\sigma_{\alpha\alpha} = \chi_{,\beta\beta}\,, \quad \sigma_{\alpha\beta} = -\chi_{,\alpha\beta}\,, \quad \sigma_{\beta\beta} = \chi_{,\alpha\alpha}\,, \tag{1.11}$$

which gives an alternate form of the FvK equations (Eq. (1.10)):

$$B\nabla^4 w - h[w,\chi] = 0 \tag{1.12a}$$

$$\nabla^4 \chi + \frac{E}{2}[w,w] = 0, \tag{1.12b}$$

where the differential operator $[...]$ is defined as $[u,v] \equiv u_{,\alpha\alpha}\, v_{,\beta\beta} + v_{,\alpha\alpha}\, u_{,\beta\beta} - 2u_{,\alpha\beta}\, v_{,\alpha\beta}$. Eqs. (1.12) are nonlinear partial differential equations for two unknown functions, the deflection $w(x_1,x_2)$ and the Airy potential $\chi(x_1,x_2)$. This form highlights the Gaussian curvature, $K = [w,w]/2$ in the second equation. In the first equation, the non-linear term couples the curvature with in-plane stress.

An extension of the FvK equations to allow for initial curvatue are the Donnell-Mushtari-Vlasov (DMV) equations, which are useful for shallow shells [160]. For simpler, linear plate deformations, Kirchoff-Love plate theory, which extends Euler-Bernoulli beam theory, can suffice [120]. In this thesis, we primarily consider deformations that are too large to be handled by the FvK of DMV equations. In Chapter 5, we discuss Non-Euclidean Plate (NEP) theory [46], which is an alternative theoretical framework suitable for arbitrarily large deformations. NEP theory is an extension of Koiter shell theory, wherein the strains are calculated with respect to a fictitious target configuration instead of the initial configuration.

Chapter 2

Buckling of geometrically confined shells

In this chapter, we study the periodic buckling patterns that emerge when elastic shells are subjected to geometric confinement. *Residual swelling* provides access to range of shapes (saddles, rolled sheets, cylinders, and spherical sections) which vary in their extrinsic and intrinsic curvatures. Our experimental and numerical data show that when these moderately thick structures are radially confined, a single geometric parameter – the ratio of the total shell radius to the amount of unconstrained material – predicts the number of lobes formed. We present a model that interprets this scaling as the competition between radial and circumferential bending. Next, we show that reducing the transverse confinement of saddles causes the lobe number to decrease with a similar scaling analysis. Hence, one geometric parameter captures the wave number through a wide range of radial and transverse confinement, connecting the shell shape to the shape of the boundary that confines it. We expect these results to be relevant for an expanse of shell shapes, and thus apply to the design of shape–shifting materials and the swelling and growth of soft structures.

2.1 Introduction

Shells are notorious for their nonlinear response to mechanical loading, and subtle changes to how they are held, or constrained, can have profound affects on how they deform. Confinement of soft shells can induce dramatic deformations as illustrated in Fig. 2·1, where radial confinement is increased from left to right. These mechanics are relevant to soft biological tissues, as their morphology often depends on a combination of mechanical

forces imparted along their boundaries, and non–mechanical forces that drive growth or swelling. Confinement of soft tissues can result in the wrinkling and scar formation of surgical wounds [20], and these changes in shape or morphology are not purely cosmetic. For example, during the embryogenesis of the ciliary body of an avian eye, differential growth induces wrinkles that radiate outward from the retina [7], a stiff region that resists deformation. Capillary blood vessels form in the valleys of these wrinkles, while molecules that promote neural cell adhesion fail to express in the regions where these epithelial tissues wrinkle [8, 9]. These effects are entirely mechanical, as evidenced by experiments that induced wrinkles in the chick eyes by swelling them in ethanol [7, 9]. Similar studies on the differential swelling and growth of artificial tumors [35, 36] and biofilms[12, 37] described the role of confinement and the mechanics of these circumferential wrinkles in much greater detail. Radial confinement occurring within airways and arteries [60], as seen in buckling and folding of mucous membranes, can cause the collapse or closure of the oesophagus [201], blood vessels [115], and gastrointestinal tract [122].

Beyond these biological systems, the ability to prescribe and control the shape of objects has ushered in an age of *designer materials* [154]. By dictating the volumetric strain in specific regions of soft elastomers, researchers have been able to morph 2D sheets into 3D shells [102, 81, 101], with features spanning multiple length scales [34, 140]. Differential swelling, sometimes accomplished by using the residual polymer chains left in portions of cured elastomers, has been used to fabricate helical ribbons [195], rolled sheets [146], saddles [145], pinched spheres [148], and wavy strips and discs [131, 43, 10]. Even for free, unconstrained plates and shells the shape selection process is non–trivial. The shapes that result from differential swelling can be determined by examining how swelling alters the metric tensor of the middle surface of the plate, an approach described by the so–called theory of unconstrained non–Euclidean plates [46]. When swelling only imparts a local curvature change along the middle surface, as is the case for the residual swelling of bi-

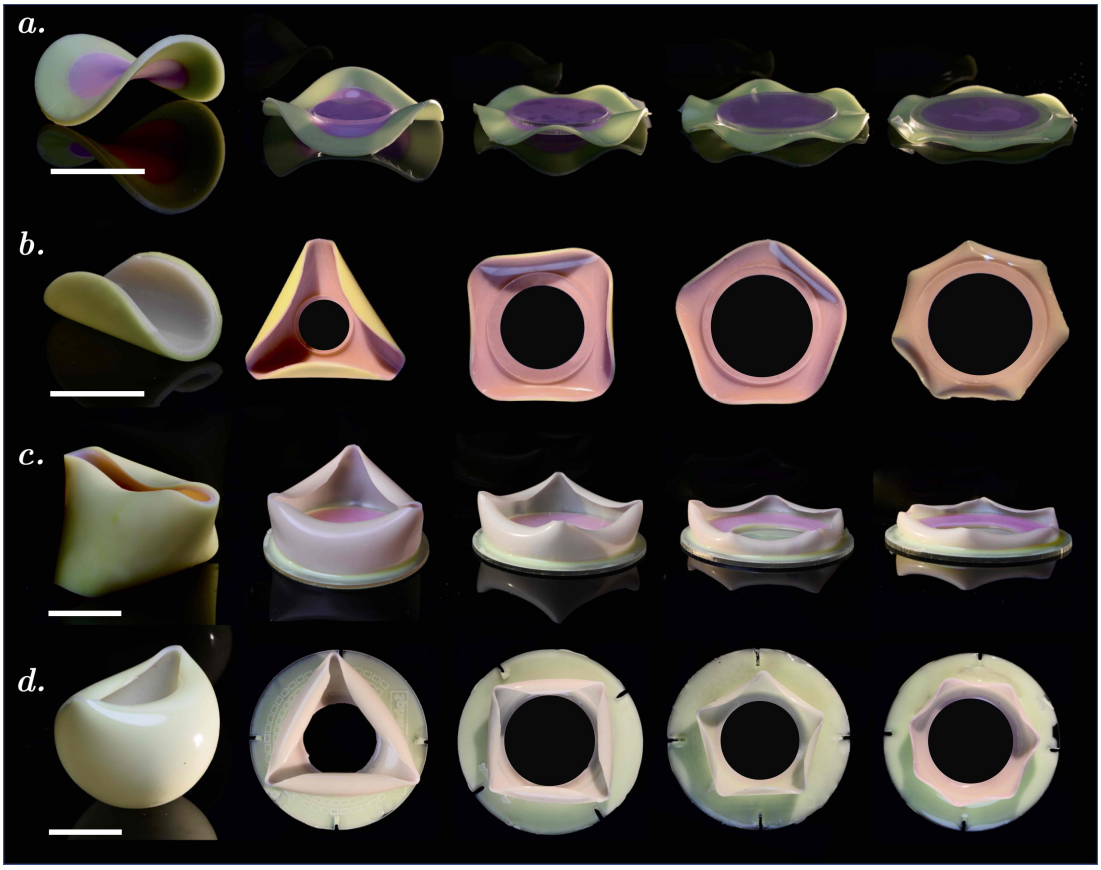

Figure 2·1: As the extent of confinement increases from left to right, the *a*. saddle, *b*. rolled sheet, *c*. cylinder and *d*. spherical segment exhibit more lobes. In *a*. and *b*., shells are clamped between acrylic plates of increasing diameter. The cylinder and sphere cut to varied *c*. heights and *d*. latitudes, and fixed with an acrylic ring at the base. Shells are made of polyvinylsiloxane (PVS). Scale bars represent 30 mm.

layer plates and shells, the non–mechanical swelling process can be cast as a mechanical stimulus which alters the natural curvature of the shell [148], and the stability of these structures can be evaluated using techniques common to applied mechanics. The inverse problem – knowing a desired shape and searching for the correct initial conditions necessary to achieve it – is a problem that has received far less attention, but will likely be more desirable. Work by Dias *et al.* demonstrated how to find the metric for a variety of axisymmetric shapes [39], while more recent work has shown how to find the metric for a

wide range of shapes, including a human face, when a curvature can be prescribed at any point [185].

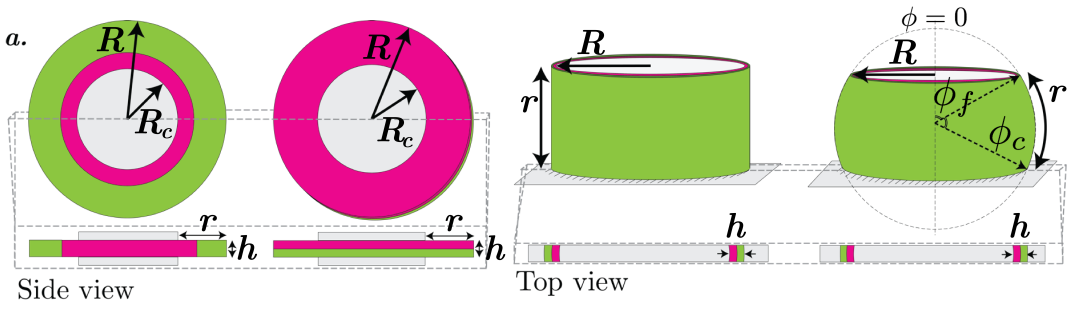

b.

	(i.) Saddle	(ii.) Rolled sheet	(iii.) Cylinder	(iv.) Spherical segment
$\mathring{\mathcal{K}}$	0	0	0	+
$\mathcal{K}_{avg}$	−	0	0	+
$\mathring{\mathcal{H}}$	0	0	+	+
$\mathcal{H}_{avg}$	0	+	+	+

Figure 2·2: *a*. Schematics showing pre-residual swelling configurations and relevant geometric parameters for the *i*. saddle, *ii*. rolled sheet, *iii*. cylinder, and *iv*. spherical segment. Pink areas will "shrink" while green ones will "grow" upon residual swelling, and grey represents areas constrained by acrylic plates. *b*. Table displays initial (accented "o") and post-swelling (subscripted "*avg*") Gaussian $\mathcal{K}$ and mean $\mathcal{H}$ curvatures for each shape.

In the effort to understand and control shape change in soft and thin structures, the interplay between intrinsic geometry and geometric constraints is still not well understood. Confining a simple 1D object, *i.e.* an *elastica*, within a rectangular box is a nontrivial problem, in part due to the unknown and evolving location of the point of contact between the elastica and the walls [42, 83, 155, 156, 149]. Similar problems emerge in the packing of thin sheets, for instance pushing a plate through a ring causes it to form a *developable* cone, or *d*–cone [3, 22, 27, 21, 26, 24], and in the confinement of a thin plate between two hemispheres [86] or onto a droplet of water [144]. Confinement of intrinsically curved shells has received less attention, with an exception being the behavior of shells under indentation [187], including a hybrid experimental-numerical study of the response of pos-

itively curved shells to indenters of varied geometries [134]. In this work, we present a primarily experimental study on how geometric confinement facilitates pattern formation in structures with intrinsic curvature. We consider shells with various mean and Gaussian curvatures under a range of radial confinement, and we examine the combined role of radial and transverse confinement on negatively curved shells, or saddles. We focus our study on four categories of shapes, shown in Fig. 2·1 and schematically in Fig. 2·2a: saddles, rolled sheets, cylinders, and spherical segments. Each is initially axisymmetric and exhibits periodic postbuckling patterns when subjected to geometric constraints. These geometries were chosen to access a range of average Gaussian and mean curvatures in their reference ($\mathring{\mathcal{K}}_{avg}$, $\mathring{\mathcal{H}}_{avg}$) and deformed ($\mathcal{K}_{avg}$, $\mathcal{H}_{avg}$) configurations.

The range of structures studied is outlined in Fig. 2·2b. Of the four shapes we study, two start out as flat plates – one of these changes its average mean curvature, and the other changes its average Gaussian curvature after fabrication. Our study omits spherical caps, which have been well-characterized, *e.g.* in Ref. [134]. These shells are relatively thick as compared to recent work on thin film confinement [144, 189, 143], and we will show that the characteristic pattern of deformation can be described by a single geometric parameter that appears to be independent of shell thickness in this regime.

2.2 Radial Confinement

Each of the unconstrained, residually stressed shapes are shown in the leftmost column of Fig. 2·1. We begin by constraining the rolled sheets and saddles in the radial direction by clamping the shells between two rigid acrylic sheets of radius R_c. In Fig. 2·1a&b, we increase R_c from left to right while keeping the shell radius R and thickness h constant, and we see that the number of lobes N, or wavenumber, increases. Three-dimensional simulations were implemented in COMSOL Multiphysics to validate these experiments for the three bilayer geometries (rolled sheets, cylinders, and spheres). Residual swelling is

represented by an inelastic distortion field, and Dirichlet boundary conditions around a ring of radius R_c act as the external constraint (see Sects. 5.7.1 & 5.2.1 for details on fabrication and simulations).

The wavenumber appears to be insensitive to changes in thickness in the range of h/R we considered (Fig. 2·3a), $h/R \in [0.008, 0.13]$ – thicker shells behave more like 3D bodies, while thinner shells made from these materials deform significantly under gravity. Instead, it appears that the wavenumber is inversely proportional to the length of material that is unconstrained, *i.e.* $r \equiv R - R_c$.

The bending energy of the shell, which we assume to be decoupled from the stretching energy, is known to scale as $\mathcal{U}_b \sim \frac{B}{2}\int \rho^2 d\omega$. The quantity $\rho = (\kappa - \kappa_o)$ represents the curvature strains – the difference between the deformed curvature κ and the curvature in the reference (unconstrained) state κ_o – and $d\omega$ is the area element.

The bending energy penalizes high curvatures, so in the circumferential direction, long wavelengths are preferable. We assume that the θ-direction wrinkle curvature will scale with the amplitude and wavelength as $\kappa^{(\theta)} \sim A/\lambda^2$, so $\rho^{(\theta)} \sim A/\lambda^2 - A_o/\lambda_o^2$. When the two initial lobes, each of amplitude A_o, are split into N lobes, the amplitude becomes $A = 2A_o/N$ – the total length does not change. Thus, $A_o \sim NA$. Similarly, $\lambda = 2\pi R/N \implies N \sim R/\lambda$, and $\lambda_o \sim R$, so that $\rho^{(\theta)} \sim A/\lambda^2 - A/(\lambda R)$. Again by inextensibility, $\lambda \sim A$, so we can also say $\rho^{(\theta)} \sim 1/\lambda - 1/R$. Together, this gives

$$\mathcal{U}_b^{(\theta)} \sim \frac{B}{2}\left(\frac{1}{\lambda} - \frac{1}{R}\right)^2 d\omega. \tag{2.1}$$

The question in regard to these constrained shells is: what opposes the circumferential bending energy to produce shorter wavelengths? Typically in (unconstrained) shell problems, competition between bending and stretching drives deformation. However, stress distributions of similarly confined structures obtained experimentally [131] and numerically [119] suggest that stretching in the radial direction is concentrated in a small region

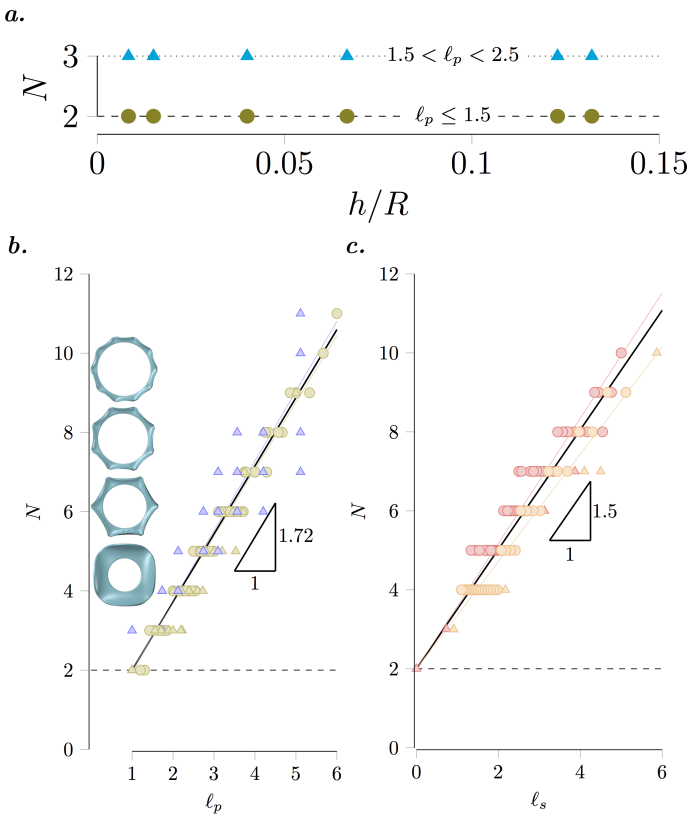

Figure 2·3: *a*. In the thickness range we study, the wavenumber is insensitive to changes in thickness, h. Instead, the amount of unconstrained material, quantified by ℓ, sets the wavenumber: for ℓ_p in a fixed range, but h/R varied, N (shown for rolled sheets) is unaffected. *b.*&*c*. The number of lobes N may be reduced to one geometric parameter, $\ell = R/r$, which quantifies the relative amount of constraint. The evolution of N is a linear function of ℓ. Triangles are experimental data points and circles are from simulations. Solid lines of best fit, and their slopes, are shown in each plot. Free of constraints, each shape has two lobes (dotted line). Solid horizontal axes are drawn according to the minimum value for ℓ. *b*. For saddles (purple) and rolled sheets (green), $\ell_p = R/(R-R_c)$, and $min(\ell_p) = 1$. Inset: Results from simulations for rolled sheets for (bottom to top) $\ell_p = \{2.2, 3.2, 4.5, 5.8\}$. *c*. For cylindrical shells (red) with height r, $\ell_s = R/r$. For spherical segments (orange), $\ell_s = \sin\phi_f/(\phi_c - \phi_f)$. The minimum of ℓ_s is 0.

near the inner boundary. Further, since in this thickness regime the shell thickness does not appear to play a dominant role in setting the wavelength, or wavenumber (Fig. 2·3a), of these constrained shells, we expect that any energy comparison should be independent of

thickness to leading order. Thus, we hypothesize that bending in the radial direction is the other relevant contribution to the energy: [1] along the length r, the radial bending energy *prefers* short wavelengths (smaller amplitudes).

In the radial direction, the curvature $\kappa^{(r)} \sim A/r^2$, so we can say $\rho^{(r)} \sim \kappa^{(r)} - \kappa_o^{(r)} \sim A/r^2 - Ao/R^2$. With the same arguments as before applied to the numerator, the bending energy in the radial direction is given by

$$\mathcal{U}_b^{(r)} \sim \frac{B}{2}\left(\frac{\lambda}{r^2} - \frac{1}{R}\right)^2 \mathrm{d}\omega. \tag{2.2}$$

Balancing the two energies in (3.3) and (3.5) gives $\lambda \sim r$. With $\lambda = 2\pi R/N \sim R/N$, and defining $\ell \equiv R/r$, we arrive at a scaling of the wavenumber as a function of the unconstrained, or free length of the shell:

$$N \sim \ell. \tag{2.3}$$

In Fig. 2·3b, we plot experimentally and numerically obtained wavenumbers N as a function ℓ_p, which is ℓ for the shells that initially started as flat plates. When the constraint $R_c \to 0$ the dimensionless length $\ell_p \to 1$, and experiments on unconstrained shells confirm that $N \to 2$ (Fig. 2·1), suggesting that for rolled sheets and saddles equation (2.3) should be modified to $N \sim \ell_p + 1$. This scaling is plotted as a solid line on Fig. 2·3b, with a slope of 1.72 found via linear regression. We would expect the slope to be of $O(1)$ if the scaling is valid, and these results suggest that our approximations were reasonable.

We now turn our attention to shells with initially nonzero mean and Gaussian curvatures. Physically, the scaling from equation (2.3) suggests that the wavenumber will increase linearly as the free, unconstrained length of the shell decreases. For the cylinders and spherical segments constrained at their base, the free length that decreases from left

[1] Inherently, these assumptions are contradictory – bending in both directions throughout the free area implies stretching, which we have chosen to neglect. We anticipate that a more thorough analysis is needed to relieve this contradiction. Here, we assume these stretching effects are small compared to bending. We are grateful to James Hanna who provided helpful insight to clarify this scaling.

to right on Fig. 2·1c&d is the arclength r of material from the clamped base to the shell opening, and similar to the rolled sheets and saddles, as this free length is decreased the wavenumber increases. Therefore, we anticipate that equation 2.3 will also capture the wavenumber of these constrained shells, provided the appropriate limits on N and ℓ_s are met, where ℓ_s is ℓ for shells that have are initially curved. Here, the unconstrained shell corresponds to $r \to \infty$, or $\ell_s \to 0$, which is analogous to the two lobe deformation (*i.e.* $N \to 2$) observed with a "pinch in a pipe" [124]. This suggests that for cylinders and spherical segments, we expect that equation 2.3 should be modified to $N \sim \ell_s + 2$. In Fig. 2·3c, we plot experimentally and numerically obtained wavenumbers N as a function ℓ_s for cylinders and spherical segments. The scaling $N \sim \ell_s + 2$ is plotted on Fig. 2·3c, with a slope of 1.50 found via linear regression. These results seem to be in good agreement with this reduced order model, suggesting that the wavenumber of a wide range of constrained shells can be characterized with a dimensionless parameter corresponding to the free length of the shell.

2.3 Transverse confinement

We will now relax the radial confinement to investigate shell behavior under varying amounts of transverse confinement. We focus primarily on an experimental analysis of saddles, because to our knowledge there are only limited examples of the transverse confinement of saddles in the literature, and the experiments on saddles are the most practically feasible out of the structures discussed in section 2.2. We constrain the shells in the transverse direction with quasi-static, displacement-controlled tests in which a saddle is compressed between pairs of acrylic plates of radius R_c. Initially, the distance d between the top and bottom plates equals the saddle's thickness, *i.e.* $\delta = d - h = 0$ (Fig.2·4a&b,i.), which represents the limit discussed in Section 2.2.

As we separate the distance between the two plates by an amount δ, there is a non-

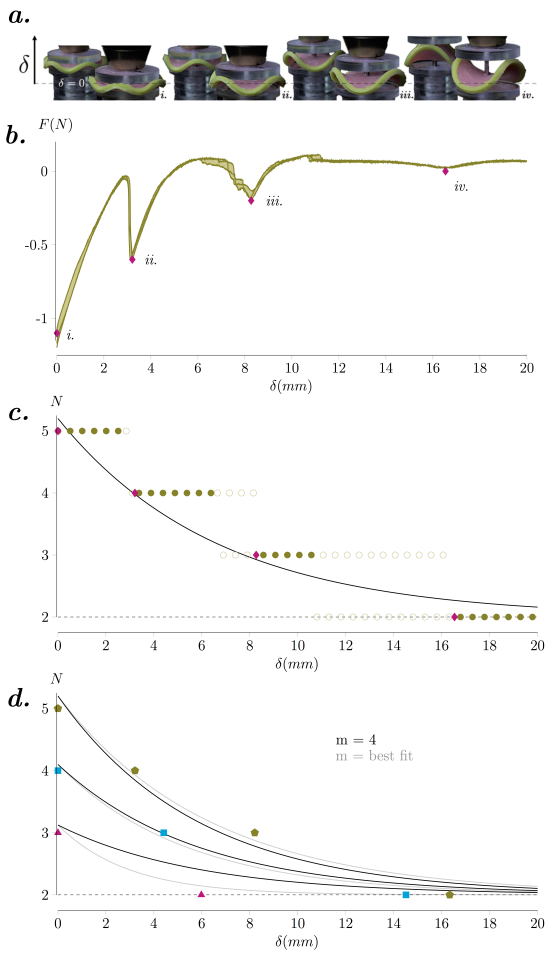

Figure 2·4: *a*. As δ increases from left to right, the number of lobes (N) decreases. The recessed images are mirrored views showing the back side of saddles. *b*. Force-displacement curves of three displacement-controlled tests on a single shell. Pink diamonds correspond to lobe transition points with Roman numerals indicating the transition from five (i.), to four (ii.), to three (iii.) to two (iv.) lobes. *c*. Wavenumber N vs. δ for the same sample. Solid points correspond to symmetric lobes, and open circles correspond to transitions between lobes. We expect the solid theoretical curve to capture the points marked by pink diamonds. This curve is equation (2.5) with $m = 3.5$. *d*. The same equation captures experimental lobe switches (points, as in *c*) with different geometric parameters. Black curves fix $m = 4$, and grey curves correspond to best fit m values: from top, $m = 3.68$, $m = 4.38$, $m = 8.00$.

monotonic decrease in the applied compressive load, and the number of lobes decreases, as shown in Fig. 2·4a, (a more detailed experimental protocol is discussed in Sect. 2.5.2).

The decrease in the compressive load is nearly linear for $\delta/A << 1$, and then reaches a minimum when one point of contact between the acrylic plate and the saddle is lost, thus beginning the mode shape transition from $N = N_{\max}$ to $N-1$ lobes. The load immediately increases, and once the saddle has reaches $N-1$ (asymmetric) lobes (Fig.2·4a&b,ii.) the load once again decreases. When a new symmetric shape is reached at $N-1$ lobes, the slope of the force-displacement curve decreases but remains positive, and the process repeats until $\delta \simeq A$, $F \simeq 0$, and there are $N = 2$ lobes (Fig.2·4a&b,iv.). The slope of the force-displacement curves through these transitions appears to gradually decrease, pointing to a diminishing effective stiffness as δ increases. Fig. 2·4b shows these trends in a force-displacement curve for a representative sample that achieves a maximum of 5 lobes at $\delta = 0$.

We now aim to provide some mechanistic insight as to the lobe transitions from $N_{\max}$ to $N = 2$ for saddles as the transverse constraint is reduced. Here, we know the two limits: (1.) as $\delta \to \infty$ we expect that $N \to 2$, and (2.) as $\delta \to 0$ we expect that $N \to N_{\max}$ as given by equation 2.3. The first limit can be simplified, because the sheet will be unconstrained once δ is larger than the amplitude of the shell's lobes, *i.e.* $N \to 2$ when $\delta \geq A$. In these experiments, while in principle ℓ_p is fixed, in effect the free length of the shell may be approximated as being a function of δ, *i.e.* $r_\delta(\delta)$, with $r_\delta(0) = r$ from section 2.2. As an *ansatz* for r_δ that meets these two limits, we chose a logistic function in the form

$$r_\delta(\delta) = \frac{R}{1 + \frac{R_c}{r} e^{-m\frac{\delta}{A}}}, \tag{2.4}$$

where m is an unknown constant that describes how quickly the unconstrained length will transition between r and R. Substituting this *ansatz* into equations $\mathcal{U}_b$ and $\mathcal{U}_k$ for r, we can solve for $N(\delta)$. Following some algebra, we find

$$N(\delta) \sim \ell_p + 1 - \frac{R_c}{r}\left(1 - e^{-m\frac{\delta}{A}}\right). \tag{2.5}$$

which reduces to equation 2.3 for plates when $\delta = 0$. In Fig. 2·4c, we plot the experimentally observed wavenumber as a function of δ. The transition process is highly nonlinear, and so we note the transition between two wavenumbers with open symbols, while highlighting the transition points from the local minima in the force-displacement curve as filled diamonds. Equation 2.5 is plotted as a solid black curve, with $m = 3.5$ chosen as a best fit parameter to the transition points. Although m is effectively a fitting parameter, we anticipate that it will depend on the bending rigidity of the saddle. We have not taken into account how the magnitude of the saddle's Gaussian curvature, which will be related to the amplitude of the lobes, nor the shell thickness affect the transition points, however we expect that m will be a function of these parameters. Further testing, in particular numerics, will help explain the contribution of $\mathcal{K}$ and h to the transition between mode numbers. Still, we note that for the samples we tests, using $m = 4$ captures the transition points for shells with $N_{\max} = 5$, $N_{\max} = 4$, and $N_{\max} = 3$ (Fig. 2·4d). Choosing the best fit values of m for each sample ($m = 3.7$, $m = 4.4$, and $m = 8.0$) changes the critical δ for observing lobe transitions, but qualitatively provides similar values. In general, the form of (2.5) clarifies the relative contributions of transverse (δ) and radial (R_c) confinement. At low δ values, radial effects dominate. As the wave number depends on δ exponentially, however, the effects of reduced transverse confinement quickly take over with increasing δ.

2.4 Conclusions

In this work, we explored geometry's fundamental role in the periodic buckling patterns that emerge in confined shells. We studied shells covering a range of Gaussian and mean curvatures, accessible via residual swelling. We first saw that one simple geometric parameter, ℓ, which relates the overall shell radius to the amount of unconfined material, predicts the number of wrinkles (N) a radially confined shell will adopt. Then for negatively curved saddles, we reduced the radial constraint by varying transverse confinement and measured

the transition points between wavenumbers.

We observed that decreasing the amount of confinement, whether in-the-plane or vertically, makes bending in the circumferential direction costly – lower buckling modes are energetically preferable in a low-confinement regime. This interpretation allowed us to generalize ℓ to include our range of transverse confinement. Thus, the model given by relation (2.5) captures a wide range of bidirectional confinement.

There is much to be done in terms of more rigorously understanding why thickness and stretching appear to be unimportant, and to put our scaling assumptions on firmer ground. A nice analog to our transverse confinement of saddles is the transverse confinement of an elastica [155, 156]. In these works, solutions for the confined elastica [83, 42] are extended to thin plates constrained progressively in the vertical direction. Our problem has subtle differences, notably that our shells are naturally curved, and our confining plates are smaller than the shell size. However, the transitions between buckling modes in our experiments are reminiscent of these studies, including qualitative features like planar contact, free-standing folds, and rolling [149]. These parallels suggest a way to pursue a more formal connection between the two problems. The shells studied in this work are residually stressed, and the magnitude of residual stress did not enter our mechanical model. It was recently shown that the magnitude of residual stress in shells will alter the critical point at which an instability occurs, *i.e.* the load required to buckle the structures, but that the instability remains qualitatively similar [94]. Also, as others [134] have observed, contact plays an important role in transverse confinement. Further numerical analysis of these constrained shells would be beneficial, in particular, such an analyses could also offer a more geometric freedom, with regards to both shells and their confining boundaries, beyond what is readily accessible experimentally. In general, we anticipate these results will aid in the design of shape–shifting structures, and we believe there are many open questions regarding the role of confinement when designing structures that change shape on

command.

2.5 Supplemental Information

2.5.1 Structure Fabrication

To fabricate the shapes shown in Fig. 2·1, we use a technique known as residual swelling [145, 146]. We use two polyvinylsiloxane (PVS) elastomers, which we will refer to as *green* (Zhermack Elite Double 32, E=0.96 MPa) and *pink* (Zhermack Elite Double 8, E=0.23 MPa). The materials are cast in as fluids and allowed to thermally crosslink, or cure, at room temperature for 20 minutes. After curing, the pink elastomer has residual polymer chains within the material, and these residual free chains flow into the green elastomer when the two materials are in contact with each other. The local loss of mass causes the pink material to decrease in volume, or shrink, while the green material correspondingly swells, thus inducing a *differential* swelling in the structure which preserves its total mass. Differential swelling in shells can lead to residually stressed structures that emerge because the shell must deform to accommodate a geometric incompatibility [102]. When the differential swelling occurs through the shell's thickness, it deforms in a nearly isometric manner in the bulk of the shell, away from shell's edges [148], and when the differential swelling occurs in-the-plane of the shell the deformation is dominated by stretching [145]. These opposing deformations explain why the initially flat shapes can be morphed into either rolled sheets or saddles. As residual swelling is a diffusive process, the time to deform scales with the square of the dimension across which swelling occurs. This characteristic dimension for swelling is either the thickness $h \approx 1mm$, or in the case of saddles, where residual swelling occurs in-the-plane, the radius, $R = 30mm$ [145].

To make homogeneous rolled sheets, we use a spin coater (Laurel Technologies, WS-650-23) to deposit a pink layer of PVS atop a laser-cut (Epilog Laser Helix, 75W) circular acrylic plate, $R \in [25mm, 35mm]$. After it cures, we add a green layer in the same man-

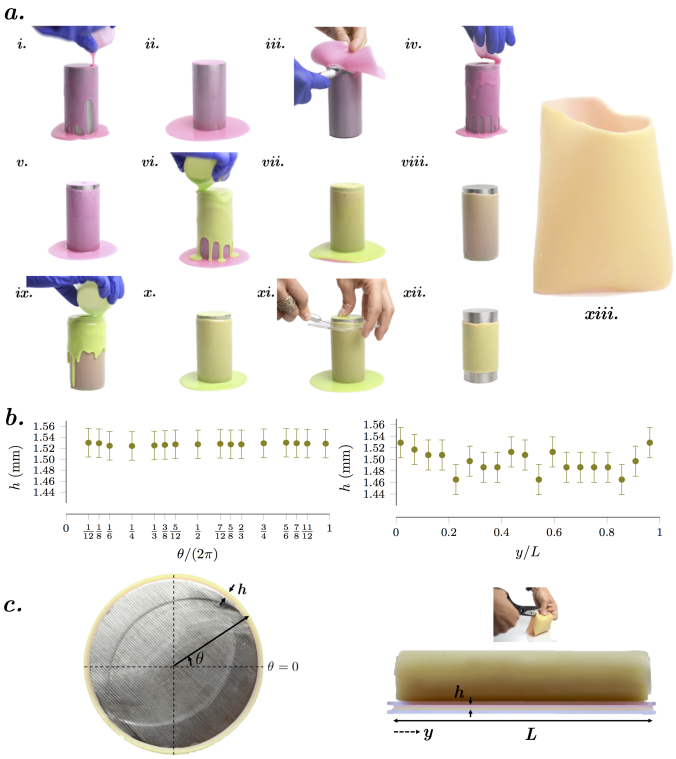

Figure 2·5: *a*. Fabrication process for a bilayer cylinder: (i.-ii.) The first pink layer of PVS is poured to uniformly coat the steel cylinder. (iii.) After 20 minutes, the first layer has cured. The cylinder is flipped upside-down, and the excess material is removed. (iv.-v.) A second layer of pink PVS is poured in order to achieve a uniform thickness in the vertical direction. (vi.-vii.) After another 20 minutes, both pink layers have cured. A green layer is added in the same manner. (viii.) After 20 minutes, the excess material is removed and the cylinder is flipped upside-down again. (ix.-x.) The final green layer is added. (xi.-xii.) After the final layer has cured (20 minutes), the bilayer cylinder is cut from the mold using a straightedge. (xiii.) The bilayer cylinder once peeled from the mold. Residual swelling causes the cylinder to buckle into a "pinched pipe". *b*. Thickness versus (right) axial and (left) azimuthal ($y = 0$) position, corresponding to parameters shown in the images in *c*. Thickness is relatively uniform in both directions, albeit more so in the radial direction. Measurements were taken using ImageJ. *c*. Top view (left) and cut view (right) show parameters relevant to the above plots. Right: to obtain thickness measurements in the axial direction, the cylinder is cut, then glued between glass plates to prevent rolling.

ner. The residual swelling first bends the sheet into a shallow spherical cap, and then ultimately buckles it into a rolled sheet – a cylinder–like shape that is open along its directrix. The rolled sheet is nearly isometric away from its edges (*i.e.* $K_{avg} = 0$) and its non–zero mean curvature is linearly proportional to the natural curvature imposed by residual swelling [146, 147, 148]. In the range of thicknesses we study, the unconstrained mean curvature $\mathcal{H}$ seems to have no effect on the wavenumber. Qualitatively, we observe that higher $\mathcal{H}$ does, however, increase the amplitude of wrinkles in constrained shells.

Saddles are made by laser-cutting a negative circular mold ($R = 30mm$) from clear cast acrylic sheets of thickness h: 0.794mm±0.119mm (Inventables), 1.589mm (tolerance -0.584mm to $+0.254$mm), 2.381mm (-0.034mm to $+0.025$mm), or 3.175mm (-0.635mm to $+0.381$ mm) (McMaster-Carr). This circular mold is glued atop a base acrylic plate, and a smaller circle, radius $R_c \in \{12.5mm, 28.25mm\}$, is centered and fixed to the base plate. We then pour green PVS to form a ring, filling the mold up to the acrylic sheet thickness. After the ring cures, the smaller circle is removed and the remainder is filled with pink PVS. After residual swelling, a saddle shape forms: $H_{avg} \approx 0$ and $\mathring{K}_{avg} < 0$ – the value of the latter depends on the ratio of pink to green polymer[146]. In-plane swelling is quite a bit slower than through-thickness swelling, since the characteristic length scale changes from the thickness to the radius [145]. The dynamics can be increased by extracting the free polymer chains in a solvent bath, *e.g. ethyl acetate*.

Cylinders and spherical segments are poured as bilayers over corresponding 3D molds. Spherical segments are formed by coating a metal ball-bearing with viscous PVS so that each layer has approximately uniform thickness [112, 148]. These spherical shells have positive average mean and Gaussian curvatures both before and after the swelling process. Cylinders are fabricated similarly [125] (see Fig.2·5), and like spheres, the initial mean curvature $\mathring{\mathcal{H}} > 0$, though $\mathring{\mathcal{K}} = 0$. After deformation, a "pinched pipe" forms [124], with $\mathcal{H}_{avg} > 0$ and $\mathcal{K}_{avg} \approx 0$.

For the experiments described in Section 2.2, rolled sheets and saddles are clamped in the center between two laser-cut acrylic plates of equal size, $R_c \in \{12.7mm, 30.5mm\}$. Cylinders and spherical segments, on the other hand, are constrained by acrylic plates glued to the base with a very thin layer of green VPS. Cylinders are then cut to varied heights, and spheres are cut at different latitudes: the angle ϕ_f is subtended by the arclength from the origin (the north pole) to the top cut (the free surface). The base, where the shell is constrained, is defined by the angle ϕ_c. Schematics of the pre-swelling configurations, including constraints, are given in Fig. 2·2. Thickness is measured at $h = \{0.25, 0.45, 0.75, 1.5, 4\}$mm ±0.15mm for Section 2.2, and $h \in$ [2.381mm ±0.1mm, 3.175mm ±0.1mm] for the saddles discussed in Section 2.3.

The wavenumber in rolled sheets, cylinders, and spheres is indifferent to whether the constraint is applied before or after residual swelling occurs, and the experimental data in Fig.2.2b&c represents a mix of both scenarios.

For saddles, where the swelling gradient lies in-the-plane, the confining plates are added after the swelling process. Our aim in this paper was to examine how, given a saddle, constraints affect its shape. Therefore, residual swelling is a tool to make these saddles. Applying the constraint beforehand leads to a different question: how does confinement affect saddle formation in residual swelling?

If the radius of the pink PVS region $R_p < R_c$, the clamp forces the pink region to stretch to conform to R_c. The inner perimeter of the green region is fixed, but the outer perimeter decreases as free chains are lost from the green polymer. Then, instead of buckling into a negatively curved saddle, the shape develops positive Gaussian curvature. This is analogous to Ref. [145], in which structures comprised of geometrically mismatched disks and annuli buckle into saddles if the perimeters require that the annulus stretches, and domes if the annulus must compress.

2.5.2 Mechanical force testing

The saddles used in Section 2.3 were fabricated with a centered 2.25mm radius hole through which we guide a 2mm radius rod as transverse confinement is varied. We determined this hole to be necessary for maintaining the saddle's position but negligible for our purposes – it has no effect on lobe number. Care was taken to align shells as close to centered as possible, as shells are sensitive to initial conditions.

We investigate transverse confinement with a setup designed for the INSTRON 5943. We attach a drill-type grip (Instron 0.375in Keyless Drill-Type Chuck Assembly) to the load cell to secure an aluminum rod (2mm radius), which is screwed to an internally threaded acrylic plate of radius R_c. A second partially threaded rod is attached to the underside of this top plate, pointing downward. The rod is guided through the saddle's center hole and then through a hole also of radius 2.25mm in the center of the acrylic base plate, which itself has radius R_c. The base plate is affixed to a thick tube of outer radius $< R_c$, inner radius 3.5mm and height 44.45mm. This tube is comprised of stacked acrylic rings each of thickness 6.35mm, glued together and closed at the base. The base of the tube is screwed to a tapped optical table.

Displacement-controlled tension tests are performed at a rate of 4 mm/min and force is measured with a 500N load cell (resolution 0.0025N). Videos were taken with a Nikon D610 DSLR Camera and were used for post-processing in conjunction with Instron data.

2.5.3 Numerics

For the three bilayer geometries where residual swelling occurs through-the-thickness, we sought to validate the experiments from Section 2.2 with simulations developed in COMSOL Multiphysics. We created a 3D model within the context of elasticity with large distortions using a Neo-Hookean incompressible material model [123]. The residual swelling stimulus is represented by a spherical distortion field $\mathbf{F}_o = \alpha(\eta^3)\mathbf{I}$ where η^3 is the gen-

eral coordinate normal to the midsurface (i.e. across the thickness). Shells are composed of two layers: in the swelling (green) layer, $\alpha(\eta^3) = \lambda_o$, and in the other (pink) layer, $\alpha(\eta^3) = 2 - \lambda_o$, where λ_o represents an inelastic stretching factor (see Fig.2·6). This ensures that the conformal stretching factor $\Lambda_o \simeq 1$, as was found experimentally for residual swelling bilayers [147]. The constraints were modeled with Dirichlet boundary conditions imposed around a ring of radius R_c in each case, reflecting the experimental setup. Solving for the deformed shape while varying geometric parameters, we confirmed our experiments from section 2.2 for rolled sheets, cylinders, and spheres.

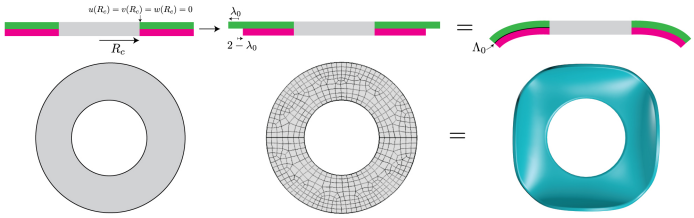

Figure 2·6: Top: Schematics depicting the distortion field and boundary conditions applied in COMSOL to the bilayer geometry, and the resulting deformation. Bottom: Top-down images from simulations showing the geometry, mesh, and deformation.

2.5.4 Buckling dynamics

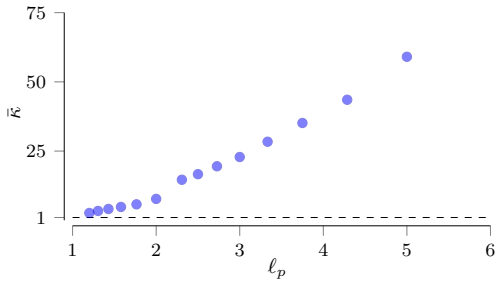

Figure 2·7: The critical buckling curvature for rolled sheets increases with the extent of constraint, quantified by ℓ_p. $\bar{\kappa}$ is the ratio of the critical buckling curvature to that of the unconstrained case, from (2.6).

We know from Ref. [147] that for the unconstrained rolled sheet ($\ell_p = 1$), the critical buckling curvature (normalized by the thickness) is

$$\kappa_b h = \sqrt{10+7\sqrt{2}}\left(\frac{h}{R}\right)^2. \tag{2.6}$$

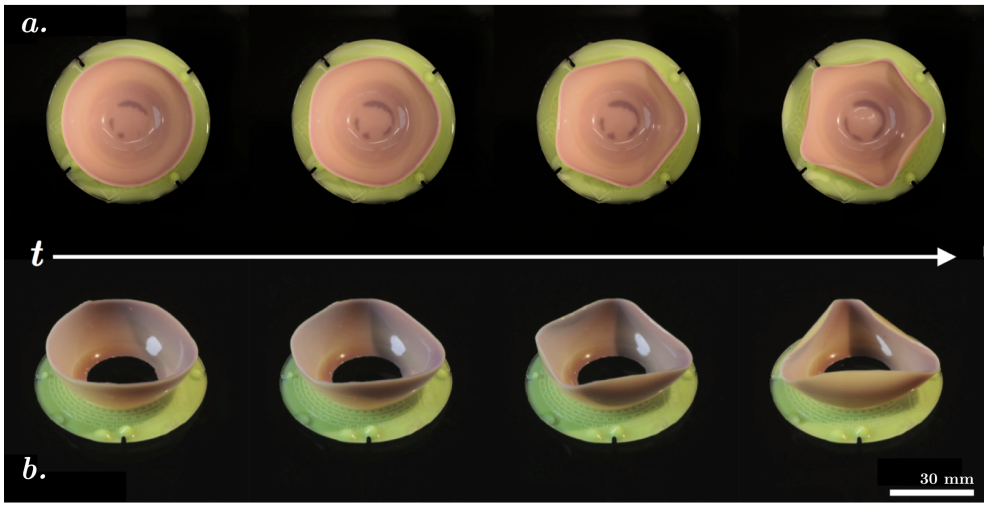

Figure 2·8: Timelapse images of constrained swelling spherical segments. Time between photos is about 40 minutes. *a*. As curvature develops, a spherical segment ($\ell \approx 2$) develops five increasingly curved lobes. *b*. A different sample ($\ell \approx 1$) is unstable through the residual swelling process: at lower curvatures (earlier in the residual swelling process), four lobes emerge. As curvature continues to increase, the spherical segment settles on three lobes as its energy-minimizing configuration.

We examine the effect of constraint on this value – our numerics allow us to extract the critical curvature required for buckling for various values of ℓ_p. This is shown in Fig. 2·7 by $\bar{\kappa}$, which represents the ratio of the buckling curvature of the constrained structure over an unconstrained but otherwise geometrically identical sheet (according to (2.6)). We observe that the buckling curvature increases with ℓ_p or, in other words, that more constrained structures require more curvature to buckle. Curvature continues to develop past the critical buckling point, and we generally observe that lobes become increasingly pronounced, as in Fig. 2·8a. However, when ℓ corresponds to an intermediate N value, the lobe-selection process can be unstable (Fig. 2·8b.) A similar bistability between two mode numbers is seen in some shells after residual swelling is complete.

Chapter 3

Circumferential Buckling of the Annular *D-cone*

The last chapter showed us that shells are highly sensitive to external confinement, and highlighted the close connection between mechanics and geometry. Now, we examine the effect of geometric confinement on intrinsically flat structures. When a thin sheet is packed into a ring, it sacrifices a small central region to stretching, preserving its developability elsewhere. Known as the developable cone or *d-cone*, this structure appears across scales and materials. When external confinement forces the center region to remain flat, the free annulus circumferentially buckles. The dynamics are rich: early wrinkles coalesce, sequentially snapping to form truncated d-cones. With precison experiments and molecular dynamics (MD) simulations, we examine the shape-selection of this *annular d-cone*. A scaling argument based on the elastic energy reveals how the size of a buckled section depends on the geometric parameters. We also show that critical force at which the first cone forms relates closely to Euler buckling of a compressed beam.

3.1 Introduction

Slender structures are exceptionally sensitive to stimuli and external forces, at times adopting wildly nonlinear configurations to minimize stretching. Often, as for a biofilm adhered to a substrate [48], the inflamed inner layer of an asthmatic airway [201], a stamped metal sheet as it is embossed [177, 86], or a lotus leaf held by its stem [197], the cause for such deformation is external confinement. In general, the first line of defense for thin, confined elastic structures is stress-focusing, wherein a plate or shell concedes a small region to high

stress so that the bulk deformation is approximately isometric, or stretch-free [194]. The canonical example of stress-focusing is the developable cone or *d-cone* [3]. The structure may be observed in a simple table-top experiment (see Fig. 3·1a,*i*): Rest a sheet of paper atop a drinking glass, then push the sheet into the open ring by indenting its center with the tip of a pencil, urging it to form a cone. To accomodate the extra material, a section buckles, losing contact with the ring and forming a convex conic section itself. By stitching together these two conics, the sheet retains unbent radial directors almost everywhere. The exception is a small, sacrificial region at the tip of the intentor, where the sheet curves and stretches severely.

Crumpled paper is peppered with d-cones [14, 194], which also spontaneously form, for example, as a Kleenex emerges from its box and when insect wings fold and unfold [65]. Thanks to this ubiquity, the d-cone has inspired an impressive body of primarily theoretical work, both from mechanics [24, 22, 3] and purely geometric [47, 163, 164] perspectives. The prevailing theoretical work is that of Cerda and Mahadevan [24]. Assuming a purely isometric deformation away from the tip of the cone, only the bending energy needs to be considered. The authors show that the shape of the sheet that minimizes the curvature strain satisfies the equation for the classic planar *elastica*. That is, by assuming unbent director lines, the three-dimensional deformations can be captured with a one-dimensional equilibrium equation. Numerical simulations have shown generally good agreement with the theory, while also revealing unexpected features, such as a small amount of radial curvature where the sheet meets the ring [117, 194, 132]. Experimental contributions are limited in quantity and geometric range [27]. Despite general agreement with theory, they also report distinguishing features that arise in real plates with finite thickness. For example, Chaïeb and Melo observed that the dislocation has a smaller angular size than predicted, and is offset from the center of the sheet [28]. It has also been reported recently that cone formation can occur as a sudden snapping event, rather than the expected smooth transition [64].

Our results support these findings. These disrepancies highlight the need for additional, thorough experimental investigations of confined sheets, which the present work seeks to address.

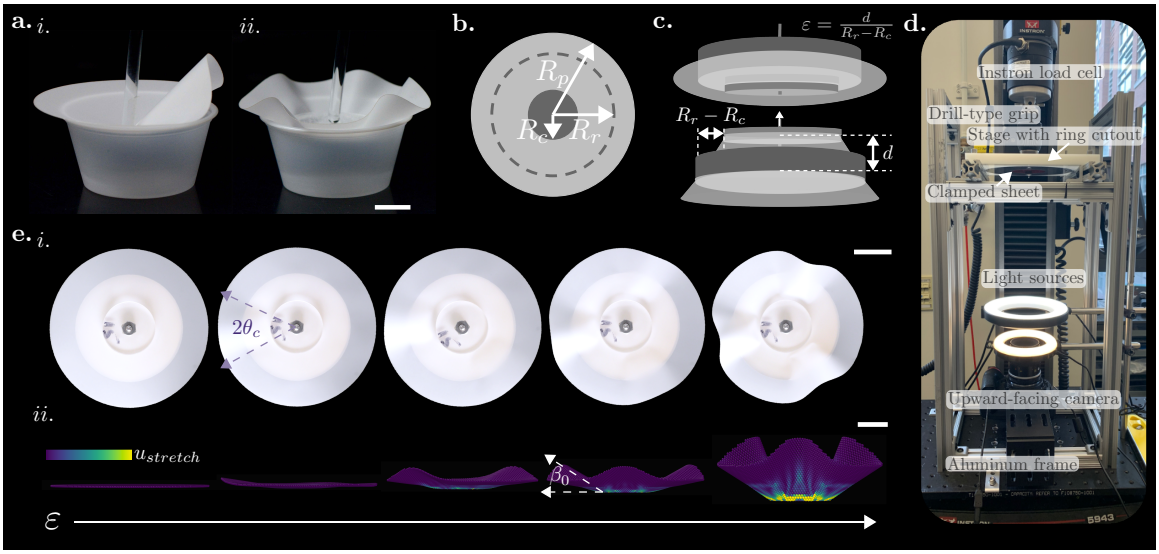

Figure 3·1: a. Table-top realizations of *i.* the d-cone [3] and *ii.* the annular d-cone, in which the addition of acrylic clamps forces the center region to remain flat. b. Schematic of relevant geometric parameters. R_c is the radius of the clamp, R_r the radius of the ring, and R_p that of the plate. c. Schematic of experiments. The clamped plate is quasi-statically pulled upward through the ring. The distance pulled is d, and the dimensionless packing parameter $\varepsilon = d/(R_r - R_c)$. d. Experimental setup. e. *i.* Images from a typical experiment with $R_p = 47.5$ mm, $R_r = 30$ mm, and $R_c = 15$ mm, and *ii.* from a simulation. Color shows the stretching energy density $u_{stretch}$, which ranges from 0 (purple) to $6 \cdot 10^{-8}$ J·m^{-3} (yellow). The contact angle θ_c is indicated in *i*, and the opening angle β_0 is shown in *ii*. All scale bars represent 15mm.

In the present work, we study a scenario in which additional confinement dictates that the central region must remain flat, preventing formation of the preferred vertex. We refer to this system as the *annular d-cone*: a thin, circular sheet which is clamped in its central region and packed into a ring. In its highly confined state, the annular d-cone consists of truncated conical buckles which are distributed around the circumference (see Fig. 3·1a,*ii*). At a glance, this periodic buckling pattern is reminiscient of wrinkles generated by com-

pressive hoop stress in swelling annular gels [131], suspended nanocrystalline films [93], or a draped tablecloth [25] or disk [15] under gravity. Yet, in this work we show that the annular d-cone is distinct from traditional wrinkling problems–subtly in its geometry, and strikingly in its dynamics.

We probe the geometry and mechanics of the annular d-cone primarily with experiments. Molecular dynamics (MD) simulations, which handle contact well compared to other simulation methods such as finite element (FE), support our experiments. Our experimental and numerical methods are described in Sect. 3.2. In Sect. 3.3, we describe the rich dynamics of shape-selection. We then present a scaling for the elastic energy in our system in Sect. 3.4, which reveals how the geometric parameters set the angular size of a dislocation. Next, in Sect. 3.5 we show *via* a scaling argument that the critical force at which the first section buckles closely relates to Euler buckling of a compressed cantilever beam. In Sect. 3.6, we offer concluding remarks.

3.2 Materials and methods

In experiments and MD simulations, we systematically varied three geometric parameters (see Fig.3·1b): R_p, the radius of the plate (i.e. the circular sheet), R_r, the radius of the ring through which we force the sheet, and R_c, the radius of the clamped region. The distance the center of the clamped sheet is pulled through the ring is given by d, where $d = 0$ when the plate just contacts the ring (see Fig.3·1c). Following e.g. Ref. [24], we define a dimensionless packing parameter $\varepsilon = d/(R_r - R_c)$. Details about the experiments and simulations follow.

3.2.1 Experiments

We performed several sets of experiments to analyze different aspects of the annular d-cone. In the main experiments, we laser-cut (Epilog Laser Helix, 75 W) circular plates of radius

$R_p \in [28, 60]$ mm from flattened polyethylene terephthalate (PET) sheets (Dupont Teijin Film, McMaster-Carr) with Young's modulus $E = 3.5$ GPa, Poisson's ratio $\nu = 0.38$, and thickness $h = 0.127$ mm. Pairs of circular clamps with radius $R_c \in [1, 35.35]$ mm were cut from acrylic (thickness 6.35 mm). All plates and clamps were cut with a 3.8 mm diameter hole at the center so that a 3.6 mm diameter partially threaded aluminum rod could be fed through the plate, which was sandwiched between two clamps. A hex nut secured the rod-clamp-plate assembly, which was then attached to the load cell of the Instron 5943 *via* a drill-type grip (Instron 0.375 in Keyless Drill-Type Chuck Assembly). A custom-built frame made from T-slotted aluminum rails (McMaster-Carr) was mounted to the base of the Instron (see Fig. 3·1d). A CNC-milled polyvinyl chloride (PVC) plate (thickness 9.525 mm) with a stepped circular cutout (diameter 55 mm) and three evenly-spaced through-holes was fixed to the top of the frame. Interchangeable PVC rings were screwed into the opening, closing the inner diameter some amount to result in a ring radius $R_r \in [12.6, 52.4]$ mm. A small number of additional tabletop experiments were performed to measure the maximum number of conical dislocations, N_{max}, for larger clamp-ring-plate combinations up to $R_c = 77.5$ mm, $R_r = 75$ mm, and $R_p = 84$ mm. Overall, $R_c/R_p \in [0.017, 0.917]$, $R_c/R_r \in [0.026, 0.972]$, and $R_r/R_p \in [0.21, 0.95]$.

The plates are very sensitive to initial conditions, so care was taken before each experiment to ensure that the ring and clamped plate ($R_p > R_r$) were level and centered with respect to one another, and that the clamped plate was just in contact with the underside of the ring. Then, quasi-static displacement-controlled tensile tests were administered using the software Bluehill 3. The clamped plate was pulled upward through the ring (see Fig. 3·1c) at a rate of $0.1 - 0.5$ mm/min. An upward-facing camera (Nikon D610 DSLR) was mounted parallel to the clamped sheet and the ring, recording deformation as the imposed upward displacement, d, increased.

Videos were used for post-processing alongside Instron force-displacement data, and

we could glean global characteristics like N_{max}. However, this view was limiting for a number of reasons, so we also performed complementary experiments. For several samples, we took 3D scans (Einscan Pro) of the sheet while the Instron was paused at regular intervals of d. This allowed us to make out-of-plane measurements, e.g. of the maximum opening angle of the cone β_0. Additionally, the projected view left large uncertainty about the contact angle θ_c, i.e. the half-angle between the two endpoints of a buckled region that contact the ring. For another subset of experiments, the Instron was stopped and points where the sheet contacts the ring were marked manually, then θ_c was measured once the sheet was released from the Instron. Further, the small-amplitude wrinkles we observe could not reliably be seen in the projected view. To image the wrinkles, we replaced the opaque PET sheets with reflective colored photo filter film ($h = 0.1$ mm, Pro Gel, B&H Photo), and stacked two circular LED ring lights (4 inch diameter, B-Qtech, Amazon and 6 inch diameter, MACTREM, Amazon) concentrically, separated by about 6 inches.

3.2.2 Molecular dynamics simulations

To obtain information that is inaccessible in experiments, e.g. the strain energy distribution, we also performed MD simulations using the Large-scale Atomic/Molecular Massively Parallel Simulator (LAMMPS). Compared to e.g. finite element (FE) simulations, MD handles contact well, which is essential for our system. To simulate a plate, we use a triangular lattice of particles, with the potential

$$U_{2d} = \frac{\sqrt{3}}{4} Eh \sum_{ij} (q_{ij} - q_0)^2 + \frac{Eh^3}{8\sqrt{3}} \sum_{ijk} (1 + \cos\theta_{ijk}). \tag{3.1}$$

Here, q_0 is the lattice spacing, which is ten times the thickness. The first term takes all nearest-neighbor particles and adds a harmonic stretching potential, and the second term takes all sets of three adjacent collinear particles and adds a bending potential. In the limit of small strains compared to unity, and large radii of curvature compared to the lattice

spacing, this model is equivalent to an elastic sheet of thickness h, Young's modulus E, bending rigidity $B = Eh^3/[12(1-\nu^2)]$, and Poisson's ratio $\nu = 1/3$. We simulate the ring using a granular pair potential with no friction, and we clamp particles by manually enforcing their displacements. No gravity is present in simulations. The thickness and modulus were set to match the main experiments. The geometric parameters were varied so that $R_c/R_p \in [0.04, 0.87]$, $R_c/R_r \in [0.06, 0.95]$, and $R_r/R_p \in [0.4, 0.93]$.

3.3 Dynamics of packing

When one begins to push a circular sheet some normalized distance $\varepsilon \ll 1$ of radius R_p into a ring whose size $R_r < R_p$, the "extra" length creates a compressive circumferential stress. To accommodate this excess, the un-clamped ($R_c \approx 0$) sheet transitions from an axisymmetric state to a d-cone at very small ε by buckling in a section whose angular size $2\theta_c$ is set by energy minimization [24]. Upon continued packing, more arclength will feed the sole [1] buckled section. The dynamics we see in our experiments and simulations are richer: transient wrinkles preceed sequential, pronounced snapping into a multi-cone structure. In this section, we report our qualitative observations of how these shape-shifting structures emerge.

In experiments and simulations, deformation is axisymmetric inside the ring, i.e. from $r = R_c$ to $r = R_r$, where r is the radial coordinate from the center. However, from R_r to R_p, axisymmetry breaks at small values of ε (i.e. $\varepsilon \lessapprox 0.05$) as the outer region wrinkles. Wrinkles are evenly distributed circumferentially, and we find that the number of wrinkles n is generally greater than the number of cones N_{max} in the final state (see Fig. 3·4). We observe in experiments that if $R_p/R_r \gtrapprox 1.3$ and $R_c/R_r \gtrapprox 0.5$, wrinkles are pronounced, propagating to the edge of the sheet with an amplitude large enough to be observed from a side view with the naked eye (Fig. 3·2b). However, simulations and experiments using

[1] The energy to form two dislocations is only slightly greater than that for a single fold, so in relatively rare cases, perturbation can lead to two-fold structures even with $R_c \approx 0$ [24].

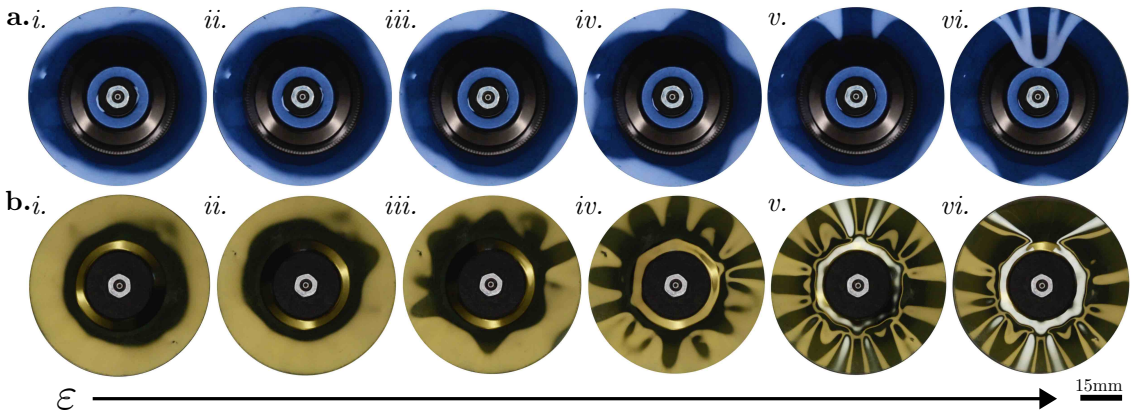

Figure 3·2: At small ε, circumferentially distributed wrinkles develop in the portion of the sheet which is outside of the ring. Deformation is axisymmetric inside the ring. a. For $R_p = 30$mm, $R_r = 15$mm, and $R_c = 6.35$mm, wrinkles have a small amplitude. In *iv.*, $n = 5$ wrinkles have formed, and two coalesce to form a cone in *v.*-*vi.* when $\varepsilon \approx 0.03$. b. More pronounced wrinkles emerge ($n = 6$ in *iv.*&*v.*) for $R_p = 30$mm, $R_r = 12$mm, and $R_c = 8.82$mm. Two wrinkles snap into a cone in *vi.* when $\varepsilon \approx 0.08$.

reflective sheets (Fig. 3·2a) reveal that wrinkling occurs across the geometries we studied, even in the d-cone limit.

This behavior is surprising in the context of the d-cone: the small-deflection state is not developable for $r > R_r$, and evidently a discontinuity exists at the ring such that the sheet is only in compression for $r < R_r$. We believe the scenario to be comparable to the curtain-like wrinkling in Ref. [186]. Supporting this conjecture is the fact that if $R_p \gg R_r$ and $R_c \lessapprox R_r$, we observe hierarchical wrinkles, wherein the wavelength is small near the ring and larger at the edge of the plate. Curtain-linke wrinkling is analogous to the wrinkling of a film is compressed atop an elastic foundation. The linear restoring force is proportional to the tension, which is higher at the compressed edge than the free edge. We expect that a similar gradient appears in our setting, such that the annular geometry acts as an elastic foundation against the bending stiffness, thus setting the wrinkle wavelength [23].

As packing increases, wrinkles grow in amplitude before two suddenly coalesce to form a single truncated cone (Fig 3·2,*vi*) of angular size $2\theta_c$. Its angular height β_0 is greater than

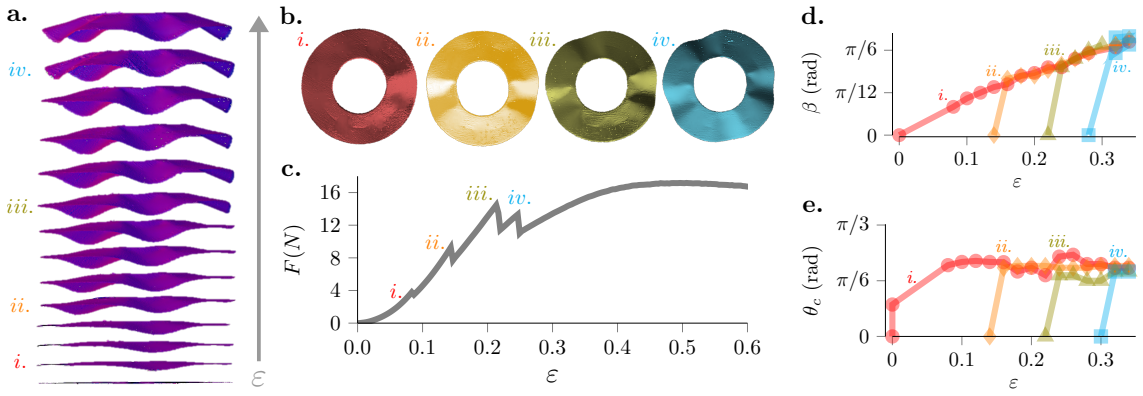

Figure 3·3: a. & b. Selected 3D scans from quasistatic experiment for $R_p = 35$ mm, $R_r = 25$ mm, and $R_c = 15$ mm. Roman numerals correspond to *i.* when the first cone has formed, *ii.* the second, and so on. c. The reaction force sharply drops when each new cone forms. d. The opening angle β_0 *vs.* ε for each cone, measured from 3D scans, and e. The contact angle θ_c for each cone. In d&e, only the last data point before each cone forms is included, for visibility. Note that a,b,d&e are from the same experiment, but c is from a separate sample with the same geometry.

that of the wrinkles. A sharp drop in the force-displacement curve (see Fig. 3·3c) and often an audible pop marks this instability. We observe that more pronounced wrinkles can delay this wrinkle-to-cone transition.

After the first cone has formed, its amplitude increases as packing progresses (Fig. 3·3d) with little, if any, change to θ_c (Figs. 3·3e & 3·6b). Then, one-by-one, more conical dislocations snap to meet the others, sharply dropping the force some amount and immediately matching the angular height β_0 of the existing cones. In most cases, additional cones also form with the same aperture angle θ_c as in Fig. 3·3, however for some geometries we observe “frustrated" structures where a smaller cone forms at high ε. Cones are not necessarily distributed symmetrically at intermediate ε, but in general the final structure will be symmetric. In the case that a smaller cone enters as a late addition, it also breaks this symmetry.

Cone formation saturates eventually, and for any further increase of ε, there will be

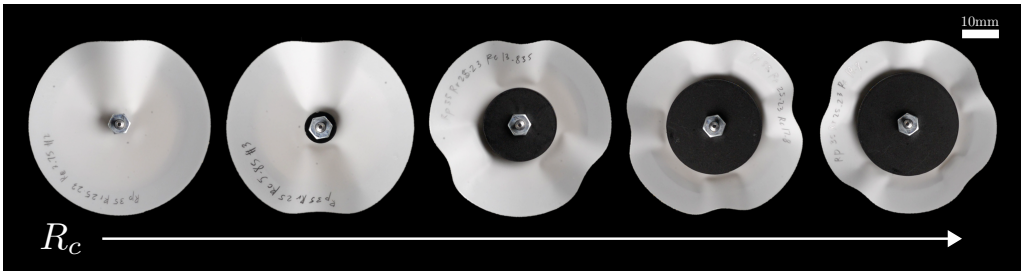

Figure 3·4: Images from experiments at large ε, after the number of cones has reached $N_{\max}$. R_p and R_r are fixed at 35 mm and 25.23 mm, respectively, and $R_c \in \{3.8, 5.9, 13.8, 17.8, 19.7\}$ mm, increasing from left to right. As the free length R_c increases, so does $N_{\max}$, from 1 to 5 in these images. In the leftmost image, the clamp is smaller than the hex nut and thus is not visible.

$N = N_{max}$ cones of equal and increasing angular height β_0. Whereas the small-deflection wrinkles are smoothly distributed along the circumference (i.e. the wavelength of a wrinkle at radial coordinate r, where $R_r < r \leq R_p$, is $2\pi r/n$), this is not necessarily the case for cones. Especially for small $R_p - R_c$, small dislocations can be separated by relatively large regions that retain contact with the ring (see Fig. 3·7b.)

The sequential and symmetric nature of the deformations we observe suggests that the essential behavior of the system is contained in the formation of the first cone. In particular, the first cone sets the angle θ_c that any additional cones will adopt (Fig. 3·3e). With this in mind, in the sections that follow, we seek to understand the mechanics at play during the first buckling event.

3.4 Contact angle

The contact angle is perhaps the most robust feature of the d-cone. In theory, the size of the buckled section that minimizes the bending energy is independent of materials and geometry (for $Rc \to 0$) [24]. Theoretical solutions in the literature predict $\theta_c \approx 1.21$ rad [24, 22] or $\theta_c \approx 1.05$ rad [27]. In several experiments with a fixed ratio $R_r/R_p = 0.95$, θ_c was measured as 0.96 ± 0.04 rad [28, 22]. In our setting, θ_c clearly depends on geometry. To

understand how so, we consider the elastic energy in the system immediately following the onset of the first buckling event.

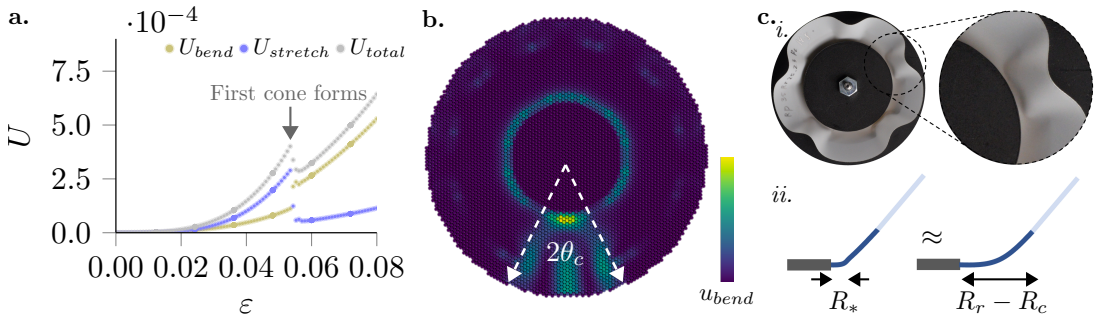

Figure 3·5: a. Comparison of energy contributions from a simulation ($R_c = 20.3$ mm, $R_r = 42.3$ mm, $R_p = 63.5$ mm). The stretching energy (blue) is the largest contribution before cone formation, but bending (green) dominates once the first cone forms. b. Contour plot of the bending energy density at cone formation, showing that the highest energy is located predominately in the dislocated region. The main contributions are distributed circumferential bending, and concentrated radial bending (yellow) near the clamp. Color bar range is from 0 (purple) to $1.5e-10$ Jm^{-3} (yellow). c. *i.* Concentrated radial bending shown in an experiment. *ii.* Schematic of radial bending approximation. Concentrated bending in a region of length R_* is approximated as distributed bending over the length $R_r - R_c$.

In simulations, we confirm that after the first cone forms, the dominant contribution to the strain energy is from bending (see Fig. 3·5a). (Note that this is not the case before buckling; the stretching energy is higher initially.) A main contribution to the bending energy is bending in the circumferential direction, which is distributed over the entire annulus in the region $0 \leq \theta \leq 2\theta_c$ (see Fig. 3·5b). We approximate the θ-direction curvature in the dislocated region as the cone amplitude over the square of the bent length, i.e.:

$$\kappa^{(\theta)} \approx \frac{r \sin \beta_0}{(\theta_c r)^2}. \tag{3.2}$$

Assuming β_0 is not too large, which is valid for $\varepsilon \ll 1$, then $\sin \beta_0 \approx \beta_0$, and further $\beta_0 \approx \varepsilon$.

Then the circumferential-direction bending energy in the dislocated region scales as:

$$\mathcal{U}_b^{(\theta)} \sim \frac{B}{2}\int_0^{\theta_c}\int_{R_c}^{R_p}\left(\frac{\varepsilon}{\theta_c^2 r}\right)^2 r\,\mathrm{d}r\,\mathrm{d}\theta = \frac{B}{2}\log\left(\frac{R_p}{R_c}\right)\varepsilon^2\theta_c^{-3}. \tag{3.3}$$

Eq. (3.3) shows that since the bending energy penalizes high curvatures, large θ_c is preferred from the perspective of the θ-direction bending energy. However, the conical dislocation also carries sharp bending in the radial direction, in a small region located near the clamp (see Fig. 3·5b&c,i). A smaller opening angle reduces this contribution to the elastic energy.

The concentrated radial-direction bending is confined to a small region $R_c < r \leq R_*$. The size of R_* (the stretching core) is unknown, and is not agreed upon in the context of the d-cone [194, 132]. Thus, we approximate this concentrated deformation as distributed bending over the length $r = R_c$ to R_r (see Fig. 3·5c,ii). Each radial director in the dislocated region bends to an amplitude set by the elastica-like curve in the θ-direction, and thus depends on θ. We approximate the θ-dependence as linear for small ε, and note that the amplitude also scales with the dislocated arclength at the ring, which itself scales with R_r. Then the curvature in the radial direction is approximately:

$$\kappa^{(r)} \approx \frac{(\theta_c - \theta)R_r}{(R_r - R_c)^2}. \tag{3.4}$$

Thus, the radial-direction contribution to the bending energy scales as:

$$\mathcal{U}_b^{(r)} \sim \frac{B}{2}\int_0^{\theta_c}\int_{R_c}^{R_r}\left(\frac{(\theta_c-\theta)R_r}{(R_r-R_c)^2}\right)^2 r\,\mathrm{d}r\,\mathrm{d}\theta = \frac{B}{2}\frac{R_r^2(R_r^2-R_c^2)}{(R_r-R_c)^4}\theta_c^3. \tag{3.5}$$

We note that bending in the radial direction near the clamp for all θ_c also contributes to the energy, but is unaffected by θ_c. Thus, we expect that θ_c is set by the competition between the circumferential and radial bending contributions in the conical dislocation region. Accordingly, we minimize the sum of Eqs. (3.3) & (3.5) with respect to θ_c (i.e.

$\partial \mathcal{U}_b^{(\theta)}/\partial\theta_c + \partial \mathcal{U}_b^{(r)}/\partial\theta_c = 0$) to find:

$$\theta_c \sim \varepsilon^{1/3}\left[\log\left(\frac{R_p}{R_c}\right)\frac{(R_r-R_c)^4}{R_r^2(R_r^2-R_c^2)}\right]^{1/6}, \quad \varepsilon \ll 1. \tag{3.6}$$

Eq. (3.6) is valid for small ε, and captures our limited data in this regime well. This is shown in Fig. 3·6a, where we plot this scaling *vs.* the measured values of $\theta_c/\theta_c^{dcone}$, with $\theta_c^{dcone} = 1.05$ rad.

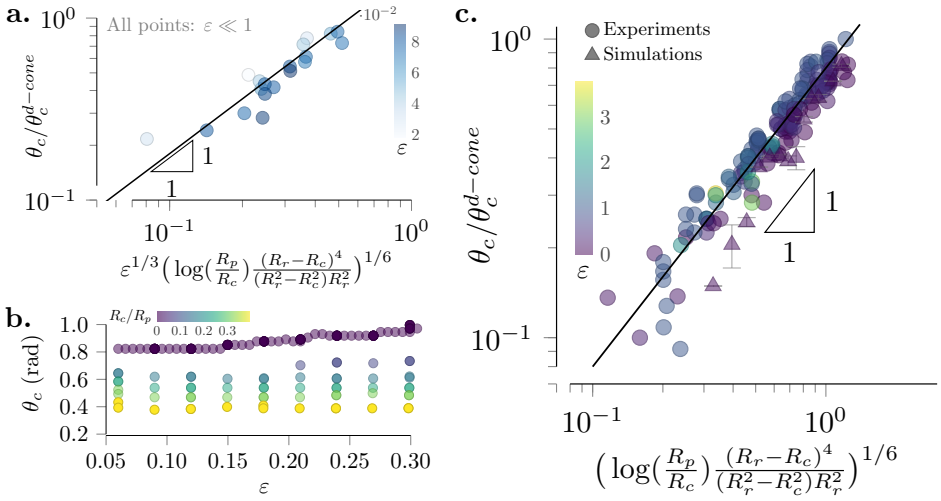

Figure 3·6: a. For limited experimental data when $\varepsilon \ll 1$, the ε-dependent scaling for θ_c given by Eq. (3.6) captures our data well. b. Plot of θ_c *vs.* ε once the first cone has formed, for fixed $R_p = 63.5$ mm and $R_r = 42.3$ mm, and increasing R_c (color bar, purple to yellow). Away from the single cone limit ($R_c \to 0$), θ_c becomes independent of ε as additional cones take up the excess length. This motivates Eq. (3.7), which is plotted in c. c. Eq. (3.6) is only valid for $\varepsilon \ll 1$, but the same scaling with $\varepsilon \to 1$ (Eq. (3.7)) applies more generally. In a&c, we take θ_c^{d-cone} to be 1.05 rad [22, 163].

Besides in the single cone limit ($R_c \to 0$) however, θ_c becomes more or less constant beyond small ε, as excess length feeds new cones as they form (see Figs. 3·6b & 3·3e.) Thus, we expect that:

$$\theta_c \sim \left[\log\left(\frac{R_p}{R_c}\right)\frac{(R_r-R_c)^4}{R_r^2(R_r^2-R_c^2)}\right]^{1/6} \tag{3.7}$$

in general. We plot this ε-independent form of Eq. (3.6) in Fig. 3·6c, where we see that it

reflects our measurements of θ_c over a broader range of ε.

The contact angle predicted by Eq. (3.7) depends purely on geometric properties, and describes the energy minimizing shape in the vicinity of one cone. Thus, it is expected that each of the additional cones that form will also follow Eq. (3.7). As we have seen, this is the case in general. A logical progression is that as packing continues, the sheet will simply pack in as many cones as it can fit, as dictated by geometry. That is, we hypothesize that $N_{max} = \pi/\theta_c$. In Fig. 3·7a, we plot $N_{max} = \pi/\theta_c + 1$ using the scaling for θ_c from Eq. (3.7). We add 1 because the scaling otherwise predicts $N = 0$ in the d-cone limit (since $R_c \to 0 \implies \log(Rp/Rc)^{-1/6} = 0$).

The parameter N_{max} is accessible in all experiments we performed, so the data in Fig. 3·7a covers a wide geometric range and includes two sheet thicknesses. We expect some degree of scatter, simply due to the quantizing effect of a discrete parameter. Overall, we indeed see the hypothesized linear trend. However, it overpredicts N_{max}. One source for this is the relatively large space between small cones when $R_p - R_c$ is small (i.e. a "bottle cap-like" distribution of cones; See Fig. 3·7b). In other, more rare cases, symmetry is broken by smaller cones that form at high ε. Thus, behavior at large ε requires a more nuanced investigation, which we do not pursue herein.

3.5 Critical force

In our displacement-controlled experiments and simulations, we measure the total reaction force in the system. While previous studies [28, 24] of the d-cone report smooth force-displacement curves[2], we observe that cone formation occurs as a sudden instability event. We identify the critical force F_c at which this instability occurs from the earliest drop in the force-displacement curve (Figs. 3·3c & 3·8a).

We observe that F_c increases for small $R_r - R_c$ (see Fig. 3·8a), which we note corre-

[2]Recently, others have reported [64] a snapping event observed experimentally for d-cone formation.

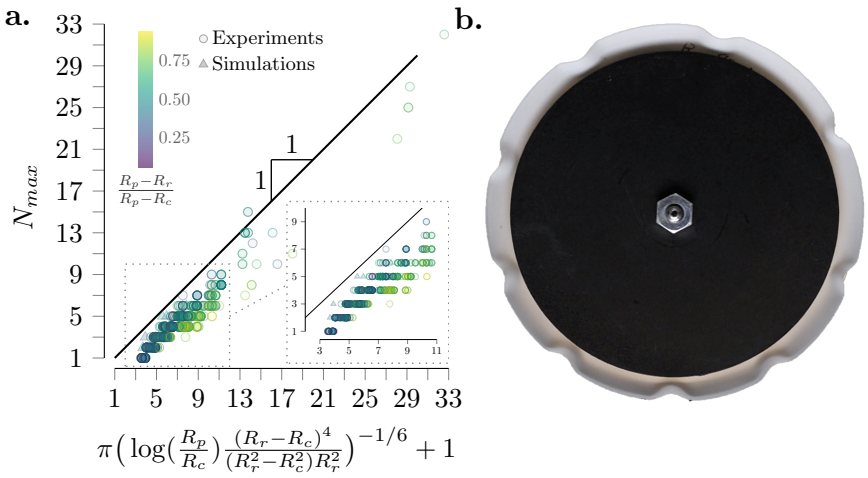

Figure 3·7: a. If the annular d-cone simply packs in the maximum number of cones of angular size θ_c, we expect $N_{max} = \pi/\theta_c + 1$, where θ_c depends on the geometry according to Eq. (3.7) (black line). This captures the general trend of our > 650 data points, but the overprediction suggests that the packing is more nuanced. Inset: zoomed-in view. b. The bottle cap-like distribution of cones seen here, especially for small $R_p - R_c$, is a source of the spread in a.

sponds to the size of the region in compression. Empirically, we determine $F_c \sim (R_r - R_c)^{-2}$. This dependence can be explained *via* an analogy to Euler column buckling. Considering a radial slice of the sheet as a cantilevered beam, which feels a compressive force f from the ring (see Fig. 3·8b), then the critical buckling force of the column is:

$$f_c = \frac{\pi^2 EI}{4(R_r - R_c)^2}. \tag{3.8}$$

Here, $I = \ell_f h^3$ is the second moment of area, where ℓ_f is a characteristic length. Since the measured force, F, is distributed over the entire sheet, $\ell_f = R_p$. The total critical force $F_c = \int_0^{2\pi} f_c \, d\theta$, so we expect that F_c, in dimensionless form, scales as:

$$\frac{F_c(1-\nu^2)}{Eh^2} \sim \frac{R_p h}{(Rr - Rc)^2}. \tag{3.9}$$

As shown in Fig. 3·8c, Eq. (3.9) agrees well with our data. This agreement elucidates the

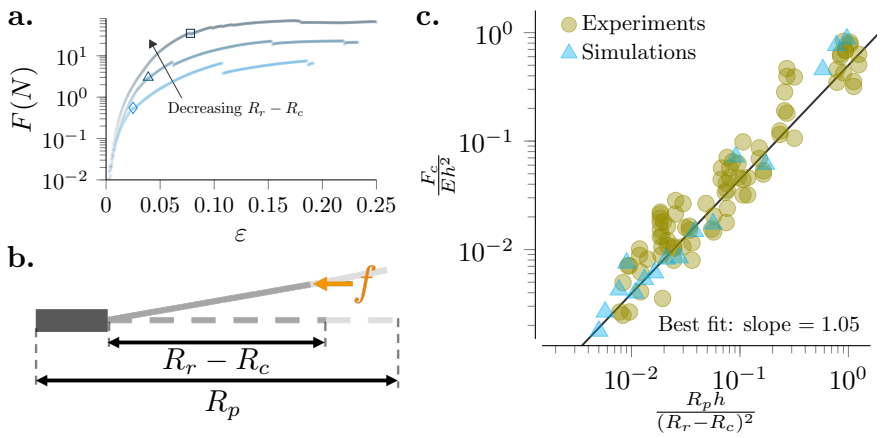

Figure 3·8: a. Force *vs.* ε curves for fixed $R_p = 45$ mm, $R_r = 25$ mm, and increasing $R_c \in 10, 17, 23$mm, i.e. decreasing $R_r - R_c$, from light to dark. The open symbols mark when the first cone forms, i.e. F_c. b. Schematic of compressed Euler column, i.e. the darker gray section (length $R_r - R_c$). The dashed line shows the reference state,. The ring exerts a compressive force f. c. The scaling for the critical force F_c at which the first cone forms agrees well with Eq. (3.9). The black line is a least-squares fit to the data, which has a slope of 1.05.

nature of the axisymmetric, compressive force inside the ring, and shows how the critical force depends on the geometric parameters.

3.6 Conclusion

In summary, we performed experiments and MD simulations to investigate the mechanics of the annular d-cone, i.e. a thin, flexible plate clamped in its central region and forced through a ring. These experiments and numerics revealed complex dynamics. Wrinkles emerge at small ε, which distribute evenly in the circumferential direction, but do not span the entire sheet in the radial direction. Rather, the part of the sheet that lies outside of the ring wrinkles, while the material compressed inside the ring remains axisymmetric. This non-axisymmetric, non-developable deformation is surprising in the context of the d-cone literature [24, 28]. Through a sudden, audible instability, two wrinkles merge to form a truncated developable cone. As packing continues, more cones sequentially snap to meet

the first, immediately matching its shape. Besides near the single d-cone limit ($R_c \to 0$), the contact angle θ_c of the first dislocation in the annular d-cone is constant beyond small ε, and only its amplitude increases. The number of cones eventually reaches a maximum, and significant bending and plastic deformation ensue.

It was evident from our experiments that the forces and deformations associated with packing the annular d-cone are highly sensitive to changing geometry. Since in general, the size of the first dislocation is the same as that of all subsequent cones, we focused on the geometry and mechanics of the initial cone formation. By considering the elastic energy in the dislocated region immediately following the onset of instability, which consists of distributed circumferential and concentrated radial bending, we determined a scaling for the the angular size of the dislocation. This scailng is valid for small ε and depends on the geometric parameters, and $\varepsilon^{1/3}$. However, because θ_c is more or less constant beyond low ε for the annular d-cone, we showed that the scaling is valid for all of our data without the ε dependence. We also showed that the critical force corresponding to this loss of stability depends on geometry in a manner relatable to Euler buckling of a compressed column.

We found that the maximum number of cones is roughly proportional to θ_c^{-1} over a wide range of data. However, some of our observations (e.g. nonuniform “bottle cap"-like spacing, and frustrated, asymmetrical structures) contradict the simple hypothesis that cones maximally distribute around the circumference. Further study of the mechanics at intermediate and high ε is needed to address this, as well as other phenomena we did not focus on herein, e.g. when new cones form. Additionally, we have widely varied the geometric confinement parameters, but not the sheet properties (i.e. the thickness, modulus, and Poisson’s ratio). To verify the validity of our scalings for the critical force and the contact angle, the effect of these parameters should studied in simulations or experiments. Future work will include a closer study of the small ε wrinkling. The intricate, shifting dynamics we have observed, as well as the non-intuitive features like non-developability and

discontinuous radial deformation, highlight the extreme sensitivity of thin sheets to changing boundary conditions. We hope that these experiments and numerics inspire further investigations of confined sheets.

Chapter 4

Delayed buckling of spherical shells due to viscoelastic knockdown of the critical load

In the last two chapters, we studied instabilities induced by external confinement. These were fundamental investigations of phenomena that are not well understood. In the remaineder of this thesis, we begin to think about how instabilities could be used for the design of devices that reversibly buckle or snap. In this chapter, we study delayed buckling of elastomer shells. With an understanding of the mechanics underlying the phenomenon, we can offer clear design guidelines.

We performed dynamic pressure buckling experiments on defect-seeded spherical shells made of a common silicone elastomer. Unlike in quasi-static experiments, shells buckled at ostensibly subcritical pressures (i.e. below the experimentally-determined load at which buckling occurs elastically), often following a significant time delay. While emphasizing the close connections to elastic shell buckling, we rely on viscoelasticity – which is often overlooked in silicone elastomers, as the rate dependence is dormant in most settings – to explain our observations.

In particular, we demonstrate that the lower critical load may be determined from the material properties, which is rationalized by a simple analogy to elastic spherical shell buckling. We then introduce a model centered on empirical quantities to show that viscoelastic creep deformation lowers the critical load in the same predictable, quantifiable way that a growing defect would in an elastic shell. This allows us to capture how both the critical deflection and the delay time depend on the applied pressure, material properties, and defect

geometry. These quantities are straightforward to measure in experiments. Thus, our work not only provides intuition for viscoelastic behavior from an elastic shell buckling perspective, but also offers an accessible pathway to introduce tunable, time-controlled actuation to existing mechanical actuators, e.g. pneumatic grippers.

4.1 Introduction

Shell structures are lightweight and flexible. Largely owing to their curvature, they offer considerable strength with little material. As a result, shells are abundant in nature (e.g. eggshells and blood vessels) and design (e.g. fuel tanks and soda cans). However, slenderness also brings susceptibility to abrupt and often catastrophic deformations. Clearly, understanding how a thin, curved structure will lose stability – and in particular at what load value this will occur – is crucial.

We restrict our attention to spherical shells in the present work. The first-known quantitative prediction for the critical load P_c in a perfect, spherical, elastic shell subjected to uniform pressure was produced by Zoelly in 1915 *via* linear eigenvalue analysis, and is given as:

$$P_c = \frac{2E}{\sqrt{3(1-\nu^2)}}\eta^{-2} \tag{4.1}$$

for a shell with Young's modulus E, Poisson's ratio ν, and radius (R) to thickness (h) ratio $\eta \equiv R/h$.

Although this result is still widely accepted today, it severely overpredicts the buckling load observed in experiments. Recognizing this disrepancy, which is due to the extreme sensitivity to imperfections inherent to thin shells, scientists at the space agency NASA and collaborators introduced the *knockdown factor* (k_d) in 1930. The quantity is defined as the ratio of the observed critical load P_c^e, to that predicted by the theory, i.e. $k_d \equiv P_c^e/P_c$. Based on surveyed experimental results [112, 190], engineers at NASA settled for the extremely

conservative design code of $k_d \approx 0.2$ for spherical shell structures [133].

Over the decades that followed, extensive work was dedicated to correcting the persistent overprediction of the critical pressure. This involved studies of the post-buckling behavior [98, 182], and the imperfection sensitivity [104, 105, 87, 18, 107, 103] of thin spherical shells. Yet, marked success arrived only recently, after Lee et al. developed a new fabrication technique for polymeric spherical caps [111]. The authors used this method to create dominant dimple-like defects (larger than those naturally occurring in the shell) with systematic size variations [112]. These experiments, validated with finite element modeling (FEM) and numerical analysis, quantitatively showed for the first time how the imperfection depth lowers the critical load.

Other contributions followed, including studies on spheres with similar dimple defects and sinusoidal equatorial undulations [88], large-amplitude dimples [95], through-thickness defects [199] (a notable predecessor is Ref. [142]), dent defects [55], and probing force imperfections [56], which collectively clarify the effect of the type of defect on the knockdown factor for spherical shells. More broadly, this long-awaited breakthrough provoked a new surge of progress in spherical shell theory (see e.g. Refs. [88, 90, 6, 89]). These developments afford engineers the opportunity to design sturdy structures with more specific – and permissive [190] – lower bounds on the load carrying capacity. This was the initial goal. In more recent years, though, a community of researchers has adopted, in a sense, the opposite goal: to design structures that buckle and snap on command [78, 154] for functions like colloidal self-assembly [158], encapsulation [170], inflatable snapping actuation [99, 62], and artificial muscle actuation [200].

The new understanding of defect sensitivity in a different light demonstrates the tunability of spherical shell buckling, and thus serves this “buckliphilic" [153] community equally. In particular, the geometry and placement of a dominant defect prescribe, respectively, the buckling strength and the spot where an instability localizes. Recent extensions

of this concept couple geometric defects with differentially swelling [113] or magneto-responsive [198] materials to modify the knockdown factor over time. Relatedly, a more general study showed how a homogenous natural curvature – which can be a proxy for nonmechanical stimuli like thermal expansion, changes in pH, or differential growth – acts to raise or lower the knockdown factor in spherical shells [80].

Besides control over when instability occurs – which depends on geometry, loading, and mechanics – mechanical actuators generally rely on reversibility. Repeatable actuation calls for robust, elastic materials, and silicone rubbers like polydimethylsiloxane (PDMS) and vinyl polysiloxane (VPS) have answered this call in mechanics research [154]. In addition to their elastic behavior, these elastomers are readily accessible and allow for fast, easy fabrication [111].

Recently, Djellouli, et al. combined these ingredients to produce a mechanical swimmer [41]. Quasi-static pressure cycles drove the device, a defect-seeded spherical shell made of the elastomer Dragon Skin^{TM} 30, to propel forward through a viscous fluid by buckling and unbuckling controllably. The authors propose that maintaining dimensionless quantities constant would allow for miniturization, with implications for drug delivery. A natural extension of this work, and the motivation for the present study, is to seek control over the speed of swimming by adjusting the frequency and/or amplitude of pressure cycles. Largely because shell and fluid motion are highly coupled in swimming, and because of possible resonance with postbucking oscillations [130], we expect this phase space to be complex. Thus, we set out to first isolate the shell buckling response, independent of fluid motion, to dynamic loading at pressures in the vicinity of the critical load.

We fabricated imperfect spherical shells like those in Ref. [41], and fixed them in place surrounded by air. A small nozzle allows for internal pressure control, through which we step-load the shells – that is, we abruptly apply, and then maintain, a pressure load. Explicitly, we reduce the pressure inside the shell cavity, creating a negative inside-outside

differential pressure. For simplicity, we will refer to this pressure difference in terms of its magnitude. These straightforward experiments produced surprisingly rich results. Even for loads below the experimentally measured elastic critical pressure (which we loosely call “subcritical" herein), we consistently observe buckling. Further, this buckling at subcritical loads occurs abruptly, often after an extended period of very slow deformation perhaps mistakeable for stability. We observe singular thresholds and a delay time which increases monotonically as pressure decreases – this contrasts the findings of a recent numerical study on dynamic step loading of spherical shells which are much thinner than our own [171].

As discussed, geometric imperfections can lead to buckling at lower-than-expected loads. In this case, though, the shell defects are already accounted for. Devoid of any plausible geometric explanation for this strange buckling behavior, our results require a closer examination of the materials. Although silicone elastomers are selected precisely because they behave elastically in most settings, they are in fact prone to time-dependent molecular rearrangement, and hence are viscoelastic [118, 202, 184]. Thus, they behave differently depending on how fast they are loaded, and exhibit both stress-relaxation (softening when subjected to a constant strain) and creep (deformation over time under constant stress).

In the present work, we rely on this viscoelasticity to account for our observations, while emphasizing the close connections to elastic spherical shell buckling. The structure is as follows: First, we introduce key aspects of our experiments in Sect. 4.2. Specifically, we report the viscoelastic material properties, describe the geometry of our imperfect spherical shells, and briefly introduce our experimental setup. In Sect. 4.3, we present an overview of our findings. We address the critical pressure conundrum in Sect. 4.4 by defining two pressure thresholds: the elastic critical pressure, and the lower viscoelastic critical pressure, which can be related through the limiting material properties. These thresholds separate three regimes: immediate buckling, delayed buckling, and no buckling (stable). In Sect.

4.5, we introduce an analogy wherein viscoelastic creep deformation lowers the critical load in the same way that a growing dimple-like defect would in an elastic shell. This provides insight about the pre-buckling deformation (Sect. 4.5.1), and reveals how the delay time preceding buckling depends on the imposed pressure, shell geometry and material properties (Sect. 4.5.2). Finally, we offer concluding remarks in Sect. 4.6.

4.2 Materials, geometry and methods

We have performed dynamic, step-loaded pressure buckling experiments on soft, viscoelastic spherical shells. Here, we briefly summarize the material properties, shell fabrication and geometry, and dynamic loading methods.

4.2.1 Material characterization

The shells used in our experiments are made of the elastomer Dragon Skin^{TM} 30 (manufactured by Smooth-On; Poisson's ratio $\nu = 0.5$ [41]). We assume that our viscoelastic material can be described by the Standard Linear Solid (SLS) model, the simplest linear model that captures both stress-relaxation (the decreasing stress response over time for a structure subjected to a constant strain) and creep (deformation under a prolonged constant stress) [203]. The SLS model describes limited creep behavior, i.e. creep deformation does not progress indefinitely, nor does the modulus eventually go to zero.

According to the SLS model, the modulus relaxes over time according to:

$$E(t) \equiv \frac{\sigma(t)}{\varepsilon} = E_\infty + E_1 e^{-t/\tau_\sigma} \tag{4.2}$$

where $\sigma(t)$ is the time-varying stress, ε the constant strain, and τ_σ the relaxation time. The parameter $E_1 \equiv E_0 - E_\infty$ quantifies the total stiffness lost as the elastic modulus E_0 decreases to the long-term (equilibrium) modulus E_∞, where $E_0 \geq E_\infty$. The function (4.2) is known as the relaxation modulus. It is related by Laplace transform to the creep compliance

function, which describes the temporally increasing strain $\varepsilon(t)$ of the SLS element under imposed constant stress σ [108]:

$$J(t) \equiv \frac{\varepsilon(t)}{\sigma} = J_0 + J_1\left(1 - e^{-t/\tau_\varepsilon}\right) \tag{4.3}$$

where $J_0 = E_0^{-1}$, $J_1 \equiv J_\infty - J_0$ with $J_\infty = E_\infty^{-1} \geq J_0$, and τ_ε is the retardation time.

We performed uniaxial tension and stress-relaxation tests using the tensile testing machine Instron 5943 to identify the parameters in Eq. (4.2) (details are provided in Appendix 4.7.1.) We found the relaxation time to be $\tau_\sigma = 0.78 \pm 0.49$ s. As for the moduli, we determined $E_0 = 0.59 \pm 0.04$ MPa and $E_\infty = 0.54 \pm 0.08$ MPa. Reported errors throughout the text correspond to one standard deviation unless otherwise noted[1]. The resulting ratio of the mean long-term modulus to the mean instantaneous one is $\bar{E} \equiv E_\infty/E_0 = 0.91$, which is central to the analysis beginning in Sect. 4.4.

Since our materials have a relatively low relaxation strength, defined as $\Delta = E_1/E_\infty$ [108], Eq. (4.2) and the inverse of Eq. (4.3) differ negligibly, i.e. $J^{-1}(t) \approx E(t)$ (see Appendix 4.7.1, Fig. 4·7). While creep is the relevant process in our experiments, our primary aim is to draw connections to elastic shell theory, which relies on the modulus E. Thus, we will use this convenient fact to interchange the representation of these two mechanisms in our analysis.

4.2.2 Shell geometry

Spherical shells were fabricated following the bi-molding method from Ref. [41], which is detailed in Appendix 5.7.1. The shells, made of two hemispheres seamed with a thin layer of diluted polymer, all have an outer radius of $R_o = R + h/2 = 25$ mm. The thickness $h \in [1$ mm, 5 mm$]$, such that $\eta \in \{24.5, 12.0, 6.6, 4.5\}$.

To control the location and direction of buckling, each shell is seeded with an im-

[1]For quantities with few measurements, the approximate standard deviation is reported as one-fourth of the error range.

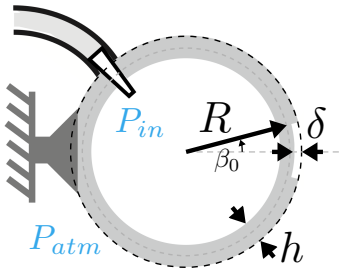

Figure 4·1: Schematic of the clamped shell with an inlet for pressure control. The flexible tube connects at its other end to a vacuum tank so that when the line is open, $P_{\text{in}} < P_{\text{atm}}$ (or $P \equiv |P_{\text{in}} - P_{\text{atm}}| > 0$). The relevant parameters are labeled: the nominal thickness h and midline radius R, imperfection depth δ, and half-angular width of the imperfection β_0.

perfection, where the thickness is reduced by an amount $\delta \in [0.40, 0.81]$ mm, such that $\bar{\delta} \equiv \delta/h \in [0.08, 0.76]$ in a circular region spanning a half-angle of $\beta_0 \approx \pi/24$ radians. The shell parameters are shown schematically in Fig. 4·1, and the effect of this defect is discussed further in Appendix 4.7.3.

Following e.g. Ref. [112], we also introduce the parameter λ, defined as

$$\lambda = \left(12(1-\nu^2)\right)^{1/4} \eta^{1/2} \beta_0, \tag{4.4}$$

which describes the defect geometry in the context of spherical caps [97, 178]. For our shells in order of increasing thickness, $\lambda \in \{1.038, 0.716, 0.612, 0.492\}$.

4.2.3 Step loading

A flexible tube was connected on one end to the inside of the shell, and on the other to a vacuum tank. An electrovalve interrupting this channel allowed us to abruptly remove air from the inner volume of the shell, creating a pressure difference of magnitude $P \in [0.3$ kPa, 46.5 kPa] (see Fig. 4·1), which we monitor with a pressure sensor. The pressure load is maintained for either the time it takes the shell to buckle, or $t_{hold} \in [5s, 360s]$. For details on the experimental setup, see Appendix 4.7.4.

4.3 Three regimes

For each of our shells, the immediate response to any non-negligible pressure load was qualitatively the same: The shell compresses as soon as the pressure is felt, and deformation quickly localizes at the unclamped pole (in the vicinity of the imperfection), forming a dimple-like depression with a deflection depth w (see Fig. 4·2 a.) Beyond this early behavior, which occurs in approximately the first 0.05 seconds, three regimes were evident from our experiments.

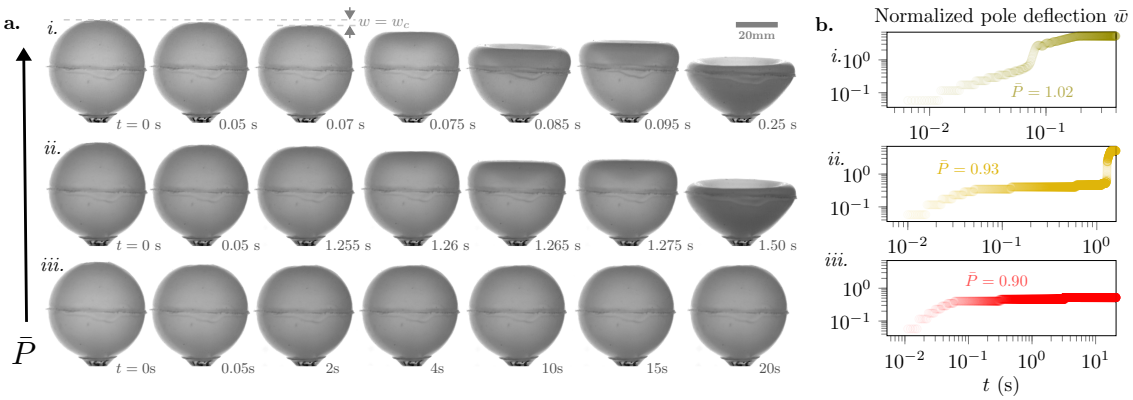

Figure 4·2: (a.) Selected high-speed camera images and (b.) corresponding plots of the pole deflection normalized by the shell thickness, i.e. $\bar{w} = w/h$, show the typical response of a shell ($\eta = 6.6$) to step loading at relatively *i.* high (supercritical), *ii.* moderate (subcritical), and *iii.* low pressures. The pole deflection w is measured from the initial state, marked in a,*i.* by the upper dashed gray line. At or above the elastic buckling pressure (e.g. $\bar{P} \equiv P/P_c^e = 1.02$), the shell quickly buckles ($t_c \approx 0.07$ s). The corresponding critical pole deflection w_c is indicated in a,*i.* Even at subcritical pressures, e.g. $\bar{P} = 0.93$, the shell eventually buckles ($t_c \approx 1.26$ s). This collapse follows a deceleration in the pole deformation at $t \approx 0.05$ s, and a subsequent period of slow, constant-rate deformation. For pressures below a second threshold, e.g. $\bar{P} = 0.90$, the shell does not buckle.

If the imposed pressure is high, the initial fast rate of pole deformation is maintained, and the shell quickly buckles – that is, the pole inverts, driving global collapse (Fig. 4·2, *i*). In postbuckling, which we do not study in detail here, the pole region is completely

inverted and oscillations occur before stability is reached again when $w \approx 2R$. We refer to this regime, wherein the shell behaves elastically throughout deformation, as the *immediate buckling regime*. The lowest pressure at which we observe this buckling behavior defines the experimental elastic critical load P_c^e. Due to the seeded defects and the non-negligible thickness of our shells, the experimentally-determined value P_c^e differs from the theoretical critical pressure P_c (Eq. (4.1)) for thin, perfect elastic shells. For details, see Appendix 4.7.3.

At slightly lower pressures, the deformation rate slows considerably following the fast response to loading, at a transition time ($t \approx 0.05$ s). The dimple slowly deepens (i.e. w increases; See Fig. 4·2, *ii*), before an abrupt acceleration after some time $t_c \in [0.09$ s, 17.09 s] signifies buckling. We define this intermediate regime as the *delayed buckling regime*. At still-lower pressures, slow pole motion eventually stops, and the shell settles into indefinite stability for as long as the load is maintained. We call this third regime the *stable regime* (Fig. 4·2, *iii*).

The value of the pressure which separates the delayed buckling and stable regimes, and hence marks the boundary of whether collapse will occur, is clearly of interest. This lower pressure threshold was more or less constant for all of our shells when normalized by the elastic load. In other words, the reduced critical pressure is independent of geometry. With this nudge toward the materials, we proceed to rationalize these findings.

4.4 Pressure thresholds via modulus ratio

Since we know our materials are viscoelastic, we can presume that the slow pole deformation under constant pressure is an exhibition of creep. This would situate our observations in the terrain of *creep buckling*. Creep buckling was introduced in the literature in 1951 [157]. The bulk of the work in this field was developed in the thirty or so years that followed, and was aimed at understanding creep collapse that occured on timescales of hours

or even days in metallic, mono-resin materials, and reinforced concrete. However, general theories emerged, which are illuminating when applied to our elastomer shells. In particular, Hayman [70, 71] and others [75, 127] proposed that a viscoelastic structure that buckles due to creep may be treated as an equivalent elastic structure with a lower critical load. The main result is that the lower threshold – which we will henceforth refer to as the viscoelastic critical pressure P_c^v – is directly related to the long-term modulus. For spherical shells, the lower critical pressure P_c^v may be found by simply replacing Young's elastic modulus E with E_∞ in calculating the elastic critical load (Eq. (4.1)). Denoting normalization by the experimentally measured elastic critical pressure P_c^e with an overbar, i.e. $\bar{P} \equiv P/P_c^e$ and $\bar{P}_c^v \equiv P_c^v/P_c^e$, that is:

$$\bar{P}_c^v = \bar{E}. \tag{4.5}$$

In Fig. 4·3, we show that (4.5) agrees with our experimental data very well, solidifying the notion that viscoelasticity is indeed the cause for the subcritical buckling we observe. The dashed line marks the theoretical lower limit where creep bucking may be observed, $\bar{P}_c^v = \bar{E}$, which for our materials (see Sect. 4.2.1 & Appendix 4.7.1) is 0.91.

Explicitly, Eq. (4.5) ignores the actual mechanism that leads to instability, creep deformation, in favor of a straightforward way to determine the minimum buckling pressure for creep-limited materials, which is perhaps the most crucial information for any design goal. Given the elastic (viscoelastic) critical pressure and the experimentally-determined instantaneous and long-term moduli, the ratio in Eq. (4.5) readily predicts the viscoelastic (elastic) critical pressure.

This view is effective and completely general with respect to geometry and material properties. However, it provides no information about deformation or the time delay that preceeds buckling. Besides that these features are of fundamental interest, understanding this delay mechanism will offer a route to including controllable delays in elastomer device

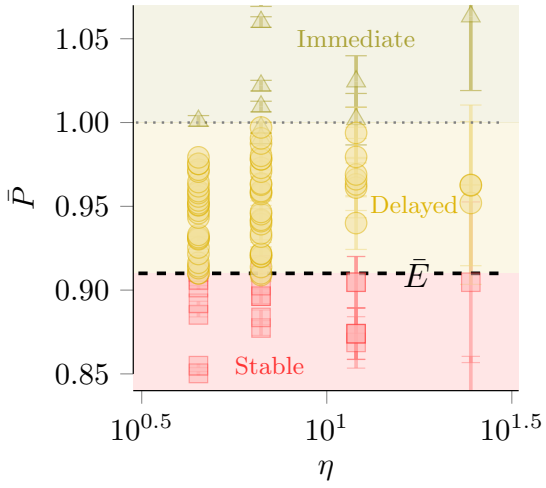

Figure 4·3: Phase plot depicting the three regimes, separated by two pressure thresholds. The elastic critical pressure (thin dotted line, $\bar{P} = 1$) was experimentally determined as the minimum pressure at which a slowdown of dynamics does not preceed buckling. We expect "immediate" (elastic) buckling for an imposed pressure $\bar{P} \geq 1$, which corresponds to the green region. The theoretical viscoelastic critical pressure $\bar{P}_c^v = \bar{E}$ (thick dashed line) is determined from (4.5) using the material parameters measured independently in stress-relaxation tests (see Sect. 4.2.1). Between $\bar{P} = 1$ and $\bar{P}_c^v$ (yellow region), viscoelastic creep can explain delayed instability at subcritical pressures. Below $\bar{P} = \bar{E}$ (red region), limited creep for our material is insufficient to cause buckling, so we expect indefinite stability. Green triangles, yellow circles, and blue squares represent, respectively, experiments which buckled elastically, buckled after a time delay, and did not buckle. Error bars represent one standard deviation.

design. We address these open questions in the following section.

4.5 Creep deformation as an evolving defect

As we have seen, the efficient, modulus-based approach in Sect. 4.4 connects the limiting critical pressure of a viscoelastic shell to that of the equivalent elastic shell. It leaves questions, however, about the time it takes a subcritically-loaded shell to buckle, and the underlying pre-buckling deformation. Traditional analytical approaches to capture the critical time and/or deflection for creep buckling involve incorporating calculated quantities

for stress and strain into the constitutive model (in our case Eq. 4.3). Instability may be identified by solving the eigenvalue problem of the governing differential equations, or by the quasi-static "critical strain approach" [54] wherein the critical strain must be known or assumed *a priori*, and the corresponding time is directly solved for [128]. These methods require precise representations of the stresses and strains throughout deformation, and have met moderate success in capturing experimental behavior for simple structures like columns [73, 74], trusses and arches [85], plates and even cylinders [54]. (See Ref. [128] for a review of the relatively recent work on creep buckling of shell structures, or Ref. [75] for an earlier review on creep buckling of plates and shells.)

A clear problem with these approaches is that it is generally assumed that a shell undergoing creep will lose stability at the same strain as its elastic counterpart [53, 76]. However, it has been noted that this assumption often leads to underprediction of the critical displacement and time [136]. Indeed, although the immediate and delayed buckling regimes appear qualitatively very similar in terms of deformation in our experiments (see Fig. 4·2, *i. & ii.*), we observe that shells which creep for longer sustain more deformation before buckling.

Complex geometries like imperfect spherical shells and their nonlinear deformations introduce significant analytical difficulties of their own. Creep buckling in spherical caps and complete spherical shells has primarily been studied with numerical analyses [84, 169, 96, 129, 196], which do not produce closed-form solutions for when instability occurs. Few experiments exist for comparison to these results, and attempts to replicate limited experimental creep buckling behavior for spherical shells have largely been unsuccessful [169, 110].

A more enlightening approach relies on the observation that the pre-buckling deformation approximately amplifies the initial defect (see Fig. 4·4a). This suggests that we may be able to draw an analogy between creep deformation and a growing imperfection in an elastic shell. This concept was proposed by Hayman in 1981, but the author conjectured that

while his "locus of critical points" approach offered intuition, it lacked predictive power for all but simple, statically determinate structures [71]. To our knowledge, the approach has not been implemented besides in the original work, when it was validated against a small number of experiments on concrete three-pin arches.

One key challenge was that the effect of the defect must be quantifiable. Indeed, as discussed in Sect. 5.1, the imperfection sensitivity of shell structures has only recently become experimentally tractable. In what follows, we rely on the work of Lee and collaborators [112], and center our analysis upon quantities that are readily determined through experiments, to derive a practical and predictive model for creep buckling in our shells.

Knowing that an imperfection “knocks down" the critical load in an elastic structure, in this view quasi-static creep deformation has the same effect. In other words, creep deformation behaves like an evolving imperfection by progressively knocking down the critical load. It follows that creep collapse occurs when the critical load associated with the “imperfect" creep-deformed structure falls to the value of the applied load. Conversely, the imperfection size associated with a given applied load should correspond to the critical deformation at which creep buckling occurs. It is important to note that this was buried but implied in the approach of Sect. 4.4; the two arguments are complementary.

To make this analogy quantitative, we turn to the recent literature on geometric imperfections in elastic spherical shells. The true defects in our shells are characterized by a local reduction in thickness as in Ref. [199] (see Appendix 4.7.3). The pole deflection generated during creep, however, is qualitatively more similar to a dimple-like imperfection where the thickness does not change, but the curvature of the shell midline does. Because the midline curvature of our shells is unaffected by the thickness reduction except at the discontinuity at either edge of the defect profile, we consider our shells initially “perfect" in the dimple sense. For the present analysis, we rely on the findings of Lee et al. [112], which are in agreement with Refs. [87, 88, 95].

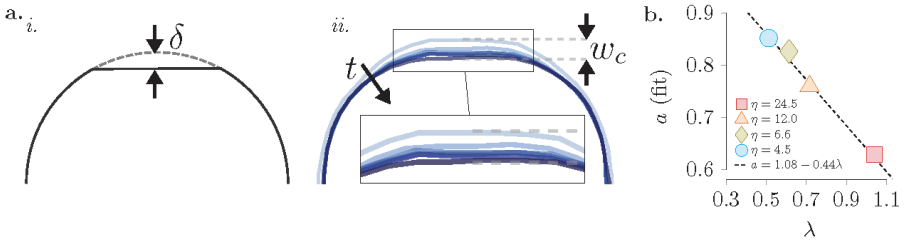

Figure 4·4: Pre-buckling pole deformation ($w \leq w_c$) is qualitatively similar to a geometric defect of increasing depth δ. (a.) *i.* Schematic of dimple-like defect in an elastic spherical shell, after e.g. Ref. [112]. *ii.* Edge contours from high-speed images at $t = 0, 0.07, 0.14, 0.21, 0.28$ s and $t_c = 0.35$ s (darkening blue corresponds to increasing time) for $\eta = 4.5$ and $\bar{P} \approx 0.97$. After initial compression, deformation localizes to the pole and progresses. (b.) Our fitting parameter $a \approx f(\lambda) = 1.08 - 0.44\lambda$.

The key finding of their work, for our purposes, is that the knockdown factor for a given shell $k_d = P_c^e/P_c$ is a function of $\bar{\delta} = \delta/h$ which initially decreases for increasing $\bar{\delta}$, then reaches a plateau. The authors present an empirically-determined function describing the lower bounding envelope over the range of λ they study, which takes the form $k_d = a + b/(c + \bar{\delta})$. We find that this functional form describes their individual curves sufficiently well.

Primarily because λ for our thick shells is below the range studied in Ref. [112], we cannot directly extract the results relevant to our work. Instead, we expect that these general trends will hold. We assume that we can simply replace the imperfection depth δ with the pole deflection w. Because we only consider the additional knockdown due to creep deformation, and not that due to the inital defect, we take the reference pressure as the experimental critical pressure P_c^e that corresponds to the initially imperfect shell. Then we define a general viscoelastic knockdown function

$$k_d^v(w) = \bar{P}_c(\bar{w}) = a + \frac{b}{c + \bar{w}}, \tag{4.6}$$

where $\bar{w} = w/h$, and a, b, and c are yet unknown.

Since w increases according to the creep strain rate, an alternative form of Eq. (4.6) specifies the time dependence. Approximating the magnitude of the circumferential strain to first order as $\varepsilon \approx w/R$, we can say $\bar{w} \approx \eta\varepsilon(t)$. From Eq. (4.3) this means $\bar{w} \approx \eta\sigma J(t)$, which is approximately $\eta\sigma/E(t)$ since the creep compliance function $J(t)$ and the inverse of the relaxation modulus $1/E(t)$ are nearly indistinguishable for our material. At early times the shell behaves elastically, so we assume Hooke's Law applies, *i.e.* $\sigma \approx E_0\varepsilon(t_t)$ at a transition time t_t between the elastic and creep stages of deformation. Further, we assume $\varepsilon(t_t) \approx \varepsilon_c^e$, where $\varepsilon_c^e \approx w_c^e/R$ is the critical strain corresponding to $\bar{P} = 1$, when the shell buckles immediately following elastic deformation. Then by Eq. (4.2), the normalized pole deflection increases with time following the relation

$$\bar{w}(t) \approx \frac{E_0\,\bar{w}_c^e}{E_\infty + E_1 e^{-t/\tau_\sigma}}. \tag{4.7}$$

Note that due to our simplified representations of stresses and strains in Eq. (4.7), all relations that follow are approximations, despite that we present them as equalities for simplicity. Substituting Eq. (4.7) in Eq. (4.6), gives a time-dependent version of the generalized viscoelastic knockdown function:

$$k_d^v(t) = \bar{P}_c(t) = a + \frac{b}{c + \frac{E_0\,\bar{w}_c^e}{E_\infty + E_1 e^{-t/\tau_\sigma}}}. \tag{4.8}$$

It remains to determine the three unknown quantities, which should explain how sensitive the critical pressure is to deformation (Eq. (4.6)) and how quickly the critical pressure decreases (Eq. (4.8)) for each shell. To do so, we constrain the functions, enforcing what we know about the limiting behavior. The critical deflection required for buckling at the elastic limit where $\bar{P} = 1$ is an experimentally-determined value, w_c^e, which differs for each shell based on geometry. Since for buckling to occur, $P_c(w) = P$, from Eq. (4.6) this condition is stated as:

$$1 = a + \frac{b}{c + \bar{w}_c^e}. \tag{4.9}$$

We also know from Eq. (4.5) that buckling will not occur below $k_d = \bar{P}_c^v = \bar{E}$. Taking the limit of the right hand side of Eq. (4.8) as t approaches infinity gives a second constraint:

$$\bar{E} = a + \frac{b}{c + \frac{\bar{w}_c^e}{\bar{E}}}. \tag{4.10}$$

Solving Eqs. (4.9) & (4.10) simultaneously gives

$$b = \frac{(a-1)(a-\bar{E})\bar{w}_c^e}{\bar{E}} \tag{4.11}$$

and

$$c = \frac{-a\bar{w}_c^e}{\bar{E}}, \tag{4.12}$$

which we insert into Eq. (4.6) to arrive at:

$$\bar{P}_c(w) = a + \frac{(1-a)(\bar{E}-a)\bar{w}_c^e}{\bar{E}\bar{w} - a\bar{w}_c^e} \tag{4.13}$$

which describes the critical pressure for a given degree of pole deflection. If $\bar{w}$ is large enough that $\bar{P}_c$ is lowered to the imposed dimensionless pressure $\bar{P}$, in theory buckling will occur.

Similarly, inserting the expressions for b and c in Eq. (4.8) gives

$$\bar{P}_c(t) = a + (a-1)(a-\bar{E})\left(\frac{E_0\bar{E}}{E_\infty + E_1 e^{-\frac{t}{\tau_\sigma}}} - a\right)^{-1} \tag{4.14}$$

which specifies the time-dependence, according to the SLS model, of the knockdown to the critical pressure that occurs as the pole deflection progresses. Again, if t is such that $\bar{P}_c = \bar{P}$, we expect collapse to occur.

Note that from Eq. (4.14), it is clear that any explicit dependence on geometry is contained in a. When a is left as a fitting parameter for the curves defined by Eq. (4.16) (see Fig. 4·6a), we find that it is a decreasing function of the geometric defect parame-

ter λ, which is in general agreement[2] with Ref. [112]. In particular, we determine $a \approx 1.08 - 0.44\lambda$ (Fig. 4·4b) for our shells. We refer to this linear function henceforth as $f(\lambda)$, and substitute it accordingly for a to emphasize the deduced connection between our fitting parameter and the defect geometry.

The deflection (Eq. (4.13)) and time (Eq. (4.14)) forms of the viscoelastic knockdown relations lead to expectations for how the critical displacement and critical time should depend on the material properties, geometry and the imposed pressure. We assess both in the following subsections.

4.5.1 Critical deflection

Evaluating Eq. (4.13) at $P = P_c(\bar{w}_c)$, replacing a with $f(\lambda)$, and solving for $\bar{w}_c/\bar{w}_c^e$ gives the following expression for the dimensionless critical deflection:

$$\frac{w_c}{w_c^e} = \frac{f(\lambda)(1+\bar{E}-\bar{P})-\bar{E}}{\bar{E}(f(\lambda)-\bar{P})} \tag{4.15}$$

which is valid when creep occurs ($\bar{P}_c^v = \bar{E} < \bar{P} < 1$, where the first equality refers to Eq. (4.5)) and tells us the pole deflection we should expect at (or, that is required for) buckling. Eq. (4.15) is plotted against our data in Fig. 4·5, showing good agreement until $\bar{P} \approx \bar{P}_c^v$. Near this asymptote, marked by the loosely dotted line, the critical deflection observed in experiments exceeds the predicted value. We discuss this deviation further in Sect. 4.5.2.

The results in Fig. 4·5 are consistent with the trend observed in the creep buckling literature, where it is suggested that a shell undergoing creep prior to buckling sustains more deformation before collapse than its counterpart that buckles elastically. The explanation is that as the imposed pressure decreases, more deformation is required to sufficiently "knock down" the critical pressure for buckling to occur.

Creep does not occur before buckling when $\bar{P} \geq 1$ (the green region in Fig. 4·5), where

[2]We fit a function of the form $k_d = a + b/(c+\bar{\delta})$ to the numerical data over $\lambda \in [1,5]$ in Fig. 6b of Ref. [112], and found $a \approx 0.5 - 0.14\lambda$.

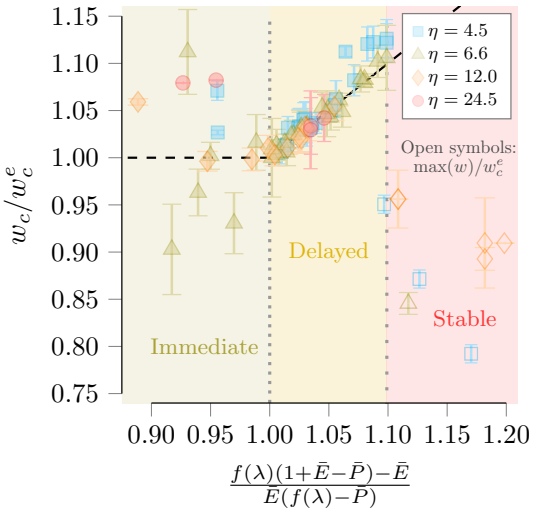

Figure 4·5: The critical pole deflection w_c depends on P, the material properties, and the geometry through $a = f(\lambda)$ and P_c^e: when creep occurs (delayed buckling, yellow region, to the left of the dotted line at 1 on the horizontal axis which marks $\bar{P} = 1$), the shell must deform more than $w_c^e = w_c(P_c^e)$ to "knock down" the critical pressure until it coincides with the imposed pressure P, and stability is lost. This is represented by the diagonal line (Eq. (4.15)), which matches our data well until the lower pressure limit for buckling is approached. This asymptote is marked by the loosely dotted line with abscissa $1/\bar{E}$, which corresponds to $\bar{P} = \bar{E} = P_c^v/P_c^e$ (Eq. (4.5)). Open symbols in the red (stable) region represent the maximum (equilibrium) w/w_c^e for experiments that did not buckle. As expected, these points fall below the theoretical line, which projects the deflection necessary for buckling. Our model does not extend to the immediate buckling regime (green region). Error bars are approximately one standard deviation.

the shell behaves elastically. In this region, where Eq. (4.15) does not apply, we do not observe a clear trend in the critical deflection. Further, for experimental points that do not buckle, the deformation was insufficient to reduce the critical pressure to the value of the relatively low applied load. Accordingly, the maximum pole deflection (open symbols in Fig. 4·5) falls below theoretical curves when $\bar{P} < \bar{P}_c^v$ (red region in Fig. 4·5). Taking the limit as t approaches infinity in either Eq. (4.3) or Eq. (4.2) gives $\varepsilon_{\max} = \sigma/E_\infty$, so $w_{\max} \approx R\sigma/E_\infty$. Meanwhile, Hooke's law provides an estimate for the critical deflection if $\bar{P} = 1$ is imposed: $w_c^e = R\sigma_e/E_0$. Then in theory, if $\bar{P} < \bar{P}_c^v$, $w_{\max}/w_c^e \approx \sigma/(\bar{E}\sigma_e) \sim \bar{P}/\bar{E}$.

We do not attempt to verify this scaling with our sparse data in this region, besides noting that as $\bar{P}$ approaches $\bar{P}_c^v$, we would expect $w_{\max}/w_c^e$ to approach 1 (from below). Our data appears to support this conjecture.

4.5.2 Critical time

We have seen that the pole deflection is analogous to a dimple-like defect. Incorporating the viscoelastic material model, in turn, tells us how the critical pressure is expected to decrease over time. This offers a means to explain the critical buckling time, which increases monotonically for decreasing pressure. To do so, we evaluate Eq. (4.14) at $\bar{P} = \bar{P}_c(t_c)$ and solve for the dimensionless critical time t_c/τ_σ:

$$\frac{t_c}{\tau_\sigma} = \ln\left(\frac{(\bar{E}-1)(f(\lambda)(\bar{E}-\bar{P}+1)-\bar{E})}{\bar{E}(f(\lambda)-1)(\bar{E}-\bar{P})}\right). \tag{4.16}$$

Eq. (4.16) is plotted against our data in Fig. 4·6. Like for the critical deflection (Fig. 4·5), the knockdown theory captures the critical time well in the intermediate range. At or above the elastic limit $\bar{P} = 1$, Eq. (4.16) predicts nonphysical critical times of $t_c \leq 0$. This is because the SLS model assumes that both loading and initial elastic deformation happens instantaneously, so creep begins at $t = 0$ s. Of course, in reality elastic instability occurs on a timescale associated with the elastic wavespeed. Accordingly, the inertial timescale t_* begins to dominate the viscoelastic one as $\bar{P}$ approaches 1. Following e.g. Refs. [141, 58, 171], we expect that the elastic timescale $t_* \sim (2R)^2/(ch)$, where $c = \sqrt{E_0/\rho} = 23.37$ m/s is the speed of sound within the material and $\rho = 1080$ kg/m^3 is the material density according to the manufacturer. For our shells in order of increasing thickness, this gives $t_* \sim \{0.1027, 0.0493, 0.0264, 0.0173\}$ s. We have indicated the elastic snap-through time for an arch $t_{snap} = 2\sqrt{3}t_*$ [141], with horizontal dashed lines in Fig. 4·6a.

When the imposed pressure nears the lower limit $\bar{P}_c^v$, the asymptotic behavior is cap-

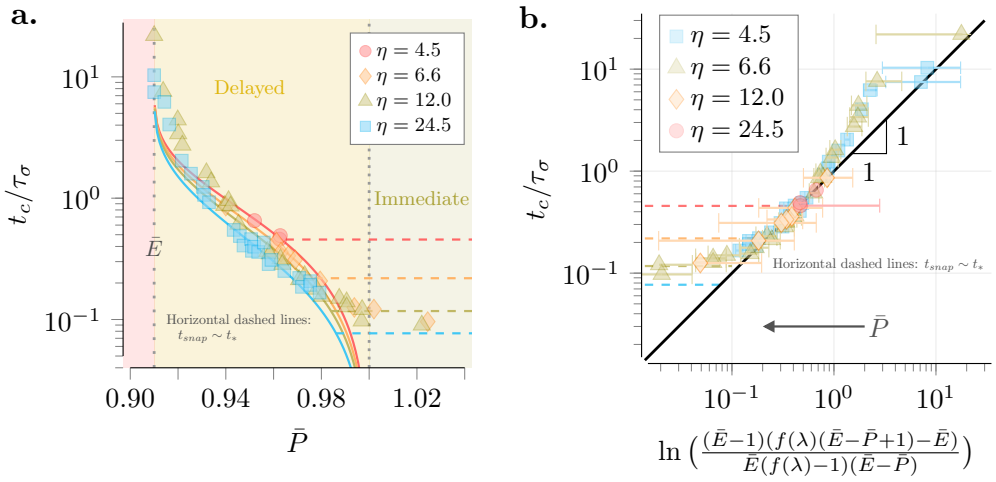

Figure 4·6: As the dimensionless applied pressure increases from $\bar{P}_c^v = 0.91$ to the elastic critical pressure $\bar{P} = 1$, the buckling time decreases monotonically according to Eq. (4.16), which specifies how long it takes for the pole to deform enough to decrease the critical pressure to the applied one. (a.) Experimental data (markers) and color-corresponding curves from Eq. (4.16), which were fit to obtain $f(\lambda) = 0.62, 0.76, 0.81, 0.85$, which is plotted in Fig. 4·4b. for $\eta = 4.5, 6.6, 12.0, 24.5$, respectively. The densely dotted vertical line marks $\bar{P} = 1$. Near this limit, the inertial (elastic) timescale, indicated by horizontal dashed lines, sets t_c for each shell. The loosely dotted vertical line marks the asymptotic pressure set by $\bar{E} = 0.91 = \bar{P}_c^v$ by Eq. (4.5). (b.) Eq. (4.16) collapses the same experimental data plotted in (a.), and captures the critical time for intermediate pressure values. When $\bar{P}$ decreases to about 0.94, the theory underpredicts the critical time. Error bars correspond to one standard deviaton in $\bar{P}$. Horizontal dashed lines in a. & b. indicate the elastic snap-through time t_{snap}, which sets the minimum t_c.

tured qualitatively (see Fig. 4·6a). However, the theory underestimates the critical time in this region. This divergence occurs around $\bar{P} \approx 0.94$, which corresponds to when the predicted buckling time surpasses τ_σ. Thus, deformation has slowed considerably prior to buckling for these experiments and the inertia that was present at early times is no longer available. We have identified elastic buckling in our experiments as when the deformation rate exceeds that at very early times (when the shell also behaves elastically). However, it is possible that buckling initiated sooner in reality, but that the shell needs further perturba-

tion – that is, to deform more, which requires more time – before we detect collapse. This is reminiscient of critical slowing down phenomena, wherein dynamics slow considerably near instability [58, 57]. Other possible explanations for the deviation from our model are the simplified representations of stresses and strains, or the inability of the SLS model to capture the material behavior exactly. Nonetheless, we conclude that despite the notable simplicity of our assumptions, the knockdown theory explains our observations quite well, and does so while emphasizing the close connections between elastic and viscoelastic shell buckling.

4.6 Conclusion

In summary, we subjected thick, spherical, defect-seeded viscoelastic shells to step pressure loading. We observed three regimes: When the pressure load was at or above the experimentally determined elastic critical load, we observed predictible elastic behavior, i.e. prompt buckling. At intermediate loads – below the elastic critical pressure – the shell buckled, albeit after a time delay during which deformation slowly progressed. At still-lower pressures, the shell deformed but collapse never occured. Our aim in this work was to rationalize our findings in a way that maintains close ties to elastic shell buckling, and is readily useable for experiment or design goals. To this end, we demonstrated that the load thresholds, critical deflection, and critical time may all be captured by a framework that treats creep deformation like an evolving defect in an elastic shell.

In particular, the ratio of the long-term modulus to the short-term (elastic) one is the same as as the ratio of the two critical pressures. This result is rooted in elastic shell theory, but practically, the material properties alone can explain the two pressure thresholds. This finding was suggested in various theoretical works on creep buckling [70, 71, 75] and is independent of geometry, and hence is completely general.

We used this fact and existing work [112] on defects in spherical shells to discern an

expression for how deformation due to creep acts to "knock down" the critical pressure. In this view, the shell loses stability when creep deformation, which localizes at pole and amplifies the initial imperfection, progresses enough to reduce the critical pressure to the value of the imposed one. This allowed us to capture the dependence of the critical deflection on the imposed pressure (normalized by the experimentally-determined elastic critical pressure), the modulus ratio, and the defect geometry (Eq. (4.15)). This offers an explanation rooted in elastic shell behavior for a decidedly viscoelastic phenomenon: in the delayed buckling regime, higher deflection is required for instability as the pressure decreases.

Because deformation occurs on a timescale sufficiently well-described by our chosen viscoelastic material model (SLS), a time-dependent form of the viscoelastic knockdown function immediately follows. From this we devise an expression for how the pre-buckling delay time depends on the same quantities: the modulus ratio, the dimensionless pressure, and the defect geometry (Eq. (4.16)). The buckling time increases monotonically but nonlinearly as the pressure decreases, which is generally captured by our model. While the modulus ratio $\bar{E}$ was fixed in our experiments, we expect that our model is valid for any material with relatively low relaxation strength (i.e. the relaxation modulus and creep compliance functions do not differ significantly). Further, we note that the success of our model does not depend on the approximation $J^{-1}(t) \approx E(t)$ that we have employed. Rather, if one were to obtain the creep compliance function in experiments, using this directly in place of the relaxation modulus would likely improve the accuracy of predictions.

While viscoelastic shells behave elastically during buckling, viscous effects re-enter in later stages of postbuckling, as discussed in Ref. [33]. Unbuckling was studied in detail in Ref. [41], as the non-reciprocal nature of the buckling-unbuckling cycle is the source of motility. We did not examine unbuckling in the present work. However, we could reasonably expect that another viscoelastic delay phenomenon, termed “pseudo-bistability" [17] (first introduced in Ref. [161] as “temporary bistability"), could be seen in our shells.

Pseudo-bistability refers to the delayed “snap-back" instability that occurs in the unloaded state, following a loading-unloading sequence that induces both stress-relaxation and creep [57]. Early works modeled viscoelasticity *via* an evolving stiffness, acheiving qualitative agreement with experiments [161, 17]. A recently-proposed metric framework introduces viscoelasticity as a temporally evolving (fictitious) reference length instead, and among its merits is the ability to predict delayed snap-back instability [184, 183]. Delayed snap-back instability occurs in the unloaded state, and in our setting would require maintaining the pressure load for a sufficiently long time while the shell is fully buckled before unloading. As such, creep instability and pseudo-bistable snap-back can in theory be induced in the same thick structure, with one or the other surpressed at will.

Our findings highlight the importance of the load rate, and the sensitivity of the shell to pressure variations in the vicinity of the elastic critical load (when approached from below). These are important considerations for structural designs using silicone rubber where either stability or elastic behavior is desired. For instance, knowledge of the critical load thresholds is clearly important when designing an efficient spherical swimmer, or indeed any viscoelastic structure that should undergo oscillatory instability. If the goal is fast motility, it would likely be desirable to minimize the time delay before buckling by avoiding the delayed buckling (intermediate pressure) regime altogether.

In other settings, viscoelastic behavior can enhance the functionality of reversibly actuatable structures. This has been demonstrated recently in designs that rely on pseudo-bistable snap-back, *e.g.* 3D-printed viscoelastic metastructures whose time-dependent properties are tunable based on temperature [29], with even more flexibility afforded by using multiple viscoelastic materials [30]. Another study examines the interplay between viscous dissipation and geometric hysteresis, as a function of the strain rate, for the design of optimal energy dissipating metamaterials [44]. Introducing tunable delays *via* creep buckling has not yet been explored, but the potential is vast: A switch or capsule could be loaded

subcritically, so that the shell has time to move to a desired location before buckling occurs. Over time as deformation reduces the critical load and thus the energy barrier [91], a much smaller probing force or other perturbation could trigger buckling. This could be useful for pneumatic gripping. A mechanical signal of fixed input frequency (and varying amplitude) could produce a varied output frequency, which has implications for mechanical computing. Because our analysis relies only on quantities that are straightforward to determine in experiments, our findings are especially amenable to accessing such tunability. As we have shown, these possibilities are achievable with the nearly-elastic materials that are already common and cherished in mechanics research.

In 1956, Gerard wrote about creep buckling that “there are almost more theories than reliable test points which can be used to check the theories" [53]. While a limited number of experimental contributions have come about since, to our knowledge our experiments on full spheres are novel to the existing creep buckling literature. Further, we have demonstrated that some concepts central to general creep buckling theories, which previously were mostly tested on metallic, mono-resin materials, and reinforced concrete [128], are indeed applicable to soft, rubbery materials. We expect that the concepts we have studied can be extended to other geometries, other loading methods, and similar polymers.

4.7 Supplemental Information

4.7.1 SLS parameters

To determine the material properties of Dragon Skin 30^{TM}, we fabricated 7 dogbone specimens (ASTM D412 Type C). The molds, cut using the Epilog Helix laser machine, were designed to give each sample a protruding defect – two thin horizontal lines 500 microns thick and separated by 500 microns – at the middle of the gauge section. These lines were tracked with a zoom lens attached to a Nikon D610, allowing for accurate strain measurements taken later in ImageJ. Samples were then tested after 16, 18, 24, 44, 65, and 94

hours at room temperature post-fabrication, as well as 1 hour after 25 minutes of curing at an elevated temperature of 65°C. The manufacturer lists the cure time as 16 hours.

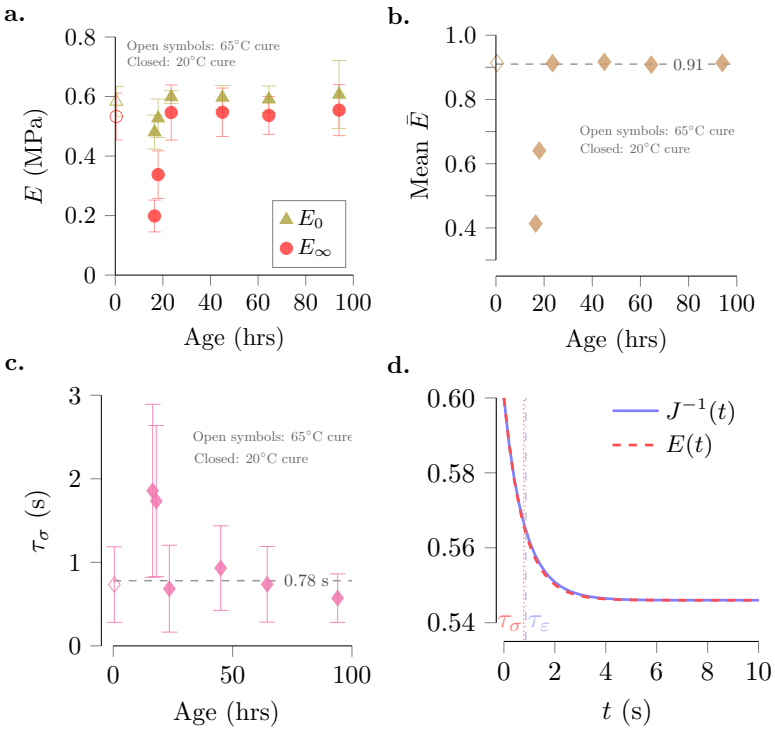

Figure 4·7: Averaged values for (a.) the elastic and long-term moduli of Dragon Skin 30^{TM} and (b.) the ratio of their mean values, as determined from tensile stress-relaxation tests. The x-axes indicate the time elapsed since fabrication; The cure time is listed by the manufacturer as 16 hours post-fabrication. (c.) Plot of the relaxation time from stress-relaxation tests. The dashed lines in (b.) & (c.) show the averaged values used in our analysis, $\bar{E} = E_\infty/E_0 = 0.91$ and $\tau_\sigma = 0.78$ s, which were determined from the samples whose ages were relevant to our experiments (24-48 hours cured at room temperature, and 0.4 hours cured at elevated temperature). (d.) SLS relaxation modulus ($E(t)$) and inverse creep compliance ($J^{-1}(t)$) functions constructed from our averaged quantitites. Because the material is nearly elastic, the $E(t) \approx J^{-1}(t)\,\forall\, t > 0$. All error bars represent one standard deviation.

The long-term (equilibrium) modulus was determined from tensile stress-relaxation tests using the tensile testing machine Instron 5943. Displacements, which resulted in strains $\varepsilon_0 \in [2\%, 20\%]$, were imposed at rates of 150-500 mm/min, then maintained for 120

seconds while the force, which decreases over a timescale $t \sim \tau_\sigma$ before plateauing, was measured. The plateau force was used to calculate σ_∞ where we took $E_\infty \equiv \sigma_\infty/\varepsilon_0$. The values for E_∞ plotted in Fig. 4·7a are calculated as the average of 12 total measurements from 4 tests at varied strain levels and strain rates.

This relatively fast loading resulted in measurement uncertainty at early times, so we did not fit a curve to the entire range of stress-relaxation data, nor did we extract the elastic modulus from stress-relaxation tests. Instead, tensile tests on the same samples were conducted at rates of 10 and 20 mm/min up to $\varepsilon_{\max} \in [8\%, 26\%]$. This resulted in linear stress-strain curves, and the slopes were used to calculate E_0. Each data point in Fig. 4·7a represents the average of 6 measurements from 2 tests for each sample.

Between 16 and 24 hours post-fabrication at room temperature (approximately 20° C), we observe an increase in the long-term modulus from 0.20 ± 0.05 MPa to 0.55 ± 0.09 MPa. By 24 hours, the long-term modulus reaches a plateau. The elastic modulus follows a similar trend: the material stiffens from $E_0 = 0.48 \pm 0.06$ MPa at 16 hours post-fabrication to 0.60 ± 0.02 MPa at 24 hours, by which time the elastic modulus has plateaued. The plateau value we measure is in agreement with the 100% modulus value listed by the manufacturer, Smooth-On, of 0.59 MPa. More or less the same plateau values result from curing the sample in the oven at 65° C for 25 minutes ($E_\infty = 0.53 \pm 0.08$ MPa, $E_0 = 0.58 \pm 0.05$ MPa).

The ratio $\bar{E} = E_\infty/E_0$ is central to our analysis, and is plotted in Fig. 4·7b. For the shell-buckling experiments discussed in the body of this paper, the relevant times are 24 and 44 hours, and the 25 minute oven-cured sample (see Appendix 5.7.1). Averaging this data gives the value we use throughout our analysis (and the dashed line in Fig. 4·7b), $\bar{E} = 0.91$. Instead including all of the samples whose moduli appear to have saturated (i.e. all except the 16 and 18 hour samples) does not change this averaged value (it only slightly increases the standard deviation, to 0.3 MPa.)

With the functional form of the relaxation modulus in mind, we identified the relaxation time τ_σ as the time when the modulus has reduced to $E_\infty + E_1 e^{-1}$. The averaged values are shown in Fig. 4·7c. The overall average was $\tau_\sigma = 0.78 \pm 0.49$ s. This corresponds to a retardation time $\tau_\varepsilon \approx 0.86$ s [108]. The relatively large error range on the characteristic timescale results from initial uncertainty in stress-relaxation curves.

In Sects. 4.4 & 4.5, we blur the lines between the creep compliance and the relaxation modulus: While the active process is creep, we use not the creep compliance, but the relaxation modulus – which describes stress-relaxation – in our analysis. This is for two reasons: First, our primary aim is to describe creep buckling in the language of elastic buckling – which refers to Young's Modulus E – rather than to provide an exact description of creep in this material. Second, we found that stress-relaxation (displacement-controlled) tests provided much more reliable data than creep (force-controlled) tests using Instron 5943.

The relaxation modulus (Eq. (4.2) in the main text) is related by Laplace transform to the creep compliance (Eq. (4.3)). Thus, the limiting values $E_0 = \sigma(t=0)/\varepsilon$ and $J_0 = \varepsilon(t=0)/\sigma$; $E_\infty = \sigma(t=\infty)/\varepsilon$ and $J_\infty = \varepsilon(t=\infty)/\sigma$ are exact inverses.

The relaxation time τ_σ is less than the retardation time τ_ε. The two are related through the relaxation strength, defined as $\Delta = E_1/E_\infty$, according to $\tau_\varepsilon = \tau_\sigma(1+\Delta)$, and thus $E(t) \neq J^{-1}(t) \forall t$ [108]. However, the difference between the two functions is very small, as shown in Fig. 4·7d. Due to this negligible difference, we conclude that our approximation in Sect. 4.5 is also reasonable.

4.7.2 Shell fabrication

The process for fabricating polymeric spherical shells, which was developed in [41], is as follows: Custom aluminum molds consist of female and male components along with alignment sleeves. The female mold is a cylinder of equal radius and height (30 mm) with a hemispherical cavity, which sets the outer radius of the shells to $R_o = 25$ mm. The

Figure 4·8: Shell fabrication process. *i.* Mixed and degassed DragonSkin 30 is poured into two hemispherical aluminum cavities of $R_o = 25$ mm. Only one is shown in *i.-iv.*, and several layers of tape have been cut into a circle and adhered to the center of one of the hollow spheres. *ii.* After degassing again, the filled cavity is fitted with an alignment sleeve. *iii.* A half-sphere of $R_i < R_o$ is inserted. *iv.* After curing for 25 minutes in the oven, a spherical hemisphere has formed. *v.* Heptane-diluted polymer is deposited with a syringe to glue two cured hemispheres. *vi.-vii.* The edges of the two hemispheres are joined and aligned by the alignment sleeve. *viii.* After curing at room temperature for at least 16 hours, a sealed sphere is removed from the mold.

male component consists of a shouldered half-sphere whose size determines the inner shell radius, $R_i = \{24, 23, 21.5, 20\}$ mm. The shoulder (chamfered to 5°) is 10 mm tall, and its maximum diameter matches that of the female mold as well as the inside of the guiding sleeve. The latter is a 40 mm tall cylindrical tube, internally chamfered up to a depth of 10mm to accommodate the male mold.

To control the location of the onset of buckling, shells are seeded with a circular imperfection. This is achieved by affixing 1-4 layers of adhesive tape cut to $R_\delta \approx 6$ mm (resulting in imperfection depth of $\delta = \{0.76, 0.81, 0.84, 0.40\}$ mm, in order for the thinnest to thickest shell) to the center of one of the two female molds used to make each shell.

To make shells, the polymer is prepared according to package instructions, degassed in a vacuum, and poured into the female molds. After degassing again, each polymer-filled cavity is fitted inside an alignment sleeve, and the male mold is inserted. The assembly is

tightly clamped between the two plates of a simple mechanical press and cured at 65° C for 25 minutes.

After curing, the alignment sleeve and the male component are removed, revealing two hemispherical shells resting in the female molds. To join the two halves, a glue is prepared. The viscosity of the liquid polymer is reduced via dilution with heptane at a 2:1 ratio. This allows for the application of a sufficiently thin layer of glue, deposited with a syringe around the equator of each hemisphere. Again a sleeve is used to align the two halves, whose contact is ensured by the mechanical press, and the shell is left to cure at room temperature for 16 hours.

A drill press is used to create a 1 mm diameter hole, into which a small nozzle connected to a tube allows for internal pressure control. Lastly, a suction cup ($2-3$ cm diameter) is glued to the shell surface opposite the buckling spot with cyanoacrylate (Loctite). During experiments, the shell is fixed in place via a screw attached to the back of the suction cup.

4.7.3 Knockdown of elastic critical pressure due to through-thickness defects

Unsurprisingly, the classical prediction for the buckling pressure of a perfect elastic spherical shell (Eq. (4.1)) does not capture the behavior of our imperfect shells. Recently, predictions for the knockdown factor as a function of the size of an axisymmetric imperfection have been presented for dimple-like [112, 95] and through-thickness [199] defects.

The reduced-thickness defects in our experiments (see Fig. 4·1) are like those in the work of Yan et al. [199]. The authors present data from experiments and FEM simulations on the knockdown factor for varied depth, angular width, and transition width of the imperfection. We use this data[3] to calculate the "knocked-down" theoretical elastic critical pressure for each of our shells. This theoretical value is plotted against our experimental data in Fig. 4·9. We have taken P_c^e to be the minimum pressure at which a plot of volu-

[3]Knockdown values were extracted from Figure 11b of Ref. [199], and found to be $k_d = \{0.2719 \pm 0.007, 0.7423 \pm 0.000, 0.8664 \pm 0.008, 0.93 + 0.070\}$ for $\eta = \{24.5, 12.0, 6.4, 4.5\}$, respectively.

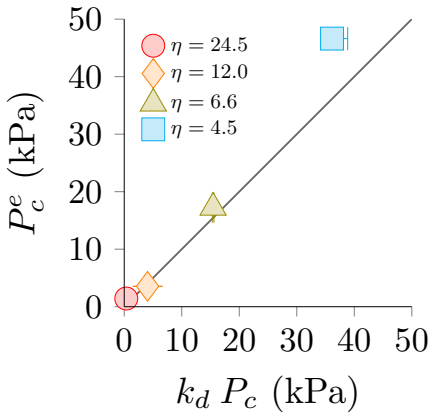

Figure 4·9: Comparison of the theoretical elastic buckling pressure P_c^e for thin, shells with through-thickness imperfections with our experimental value. The experimental value is taken as the minimum pressure at which no slowdown of deformation occurs before buckling. The theoretical value $k_d P_c$ is calculated using k_d extracted from Fig. 11b in Ref.[199], and P_c from Eq (4.1). Error bars correspond to approximately one standard deviation, and are smaller than the markers in most cases.

metric or pole deformation versus time shows no slope change until buckling (the rate of deformation is much slower when creep occurs.)

Up to relatively thick shells, the theoretical knockdown predicts our experimentally measured critical pressure relatively well ($\eta = 24.5, 12.0, 6.6$) – perhaps surprsingly so, given that the data in Ref. [199] was collected in quasi-static experiments on shells of fixed $\eta = 100$. However, as η decreases even further from the thin shell limit, the thick shell withstands higher pressures than predicted. This inapplicability of thin shell knockdown theories is significant for the thickest shell we tested ($\eta = 4.5$). For consistency, then, in all arguments throughout the main text we rely on an experimentally determined value for the elastic buckling pressure. Thus, we take the experimental value for P_c^e to be the minimum pressure difference where elastic buckling occurs.

4.7.4 Methods for dynamic pressure loading experiments

Before each experiment, a vacuum pump (Becker U 4.40) is used to reduce the pressure inside a 50 liter tank. A flexible tube (3 mm inner diameter, 12 cm length) connects the tank to a differential pressure sensor (Freescale Semiconductor MPX5100DP, sensitivity 45mV/kPa). Pressure readings were recorded using a microcontroller (Arduino UNO) every 0.02 s with a resolution of 0.1 kPa.

As this pressure resolution is slightly coarse for the thinner shells, which buckle at pressures on the order of 1 kPa, we account for rounding (and small pressure fluctuations) by reporting the mean and standard deviation of the pressure values reported at intermediate[4] times (after initial elastic deformation and before buckling, should it occur).

Via a T-junction, a second tube (6 cm long) connects the tank to the inside of the shell, by way of an electrovalve (Matrix Pneumatics Solenoid Valve, MX891.901C224). The response time of the valve is < 1 ms. Based on a back-of-the-envelope calculation of the amount of gas that needs to travel from the shell to the tank for pressure equilibrium and the corresponding mass flow rate, we expect that shell-vacuum tank system equilibriates within approximately 4 ms for pressures imposed on the thickest shell (where higher pressure gradients drive faster air flow), to about 40 ms for the thinnest.

Arduino IDE software enables synchronization of the sudden opening of the valve with the digital recording of the pressure difference (at a rate of 500 Hz), as well as with the triggering of the high-speed camera (Phantom Miro 310). Depending on the empirically determined delay time before buckling, images were captured at a rate of 2000-9000 frames per second. Image processing of TIFF stacks was completed using ImageJ and custom Python scripts.

[4]For shells subjected to large P which buckle elastically, we simply report the (non-fluctuating) imposed pressure, recorded before the shell begins to deform, with a default maximum error of ± 0.05 kPa.

4.7.5 Time-dependent equilibrium paths

In Sect. 4.4, we rationalize buckling at apparently subcritical pressures by introducing a lower pressure threshold, which is associated with the long-term modulus E_∞. Here we elaborate on the underlying theoretical framework, which we have adopted from Hayman and others [70, 71, 75], as it applies to our spherical shells.

Following, e.g. Ref. [70], the viscoelastic pressure threshold can be understood through the existence of a long-term equilibrium path in addition to the elastic one, which is available only at early times. The shape of such a path is like that of the equivalent elastic shell, but is governed[5] by the long-term modulus E_∞ rather than the instantaneous modulus E_0. These two deformation paths are shown schematically in Fig. 4·10b&c.

The loading response at different pressures, which is qualitatively depicted in Fig. 4·10, can be understood as follows: When an instantaneous pressure load is delivered to a shell, in short times it follows the instantaneous path (dashed green line in Fig. 4·10a-c). If P is at or above the elastic critical pressure P_c^e (marked by the solid, horizontal green line in Fig. 4·10a-c), the black arrowed path in Fig. 4·10a is followed, and immediate (elastic) buckling occurs (green “x" in Fig. 4·10a).

On the other hand, if an instantaneous sustained load P is below P_c^e, the initial elastic response is followed by time-dependent creep (horizontal arrows in Fig. 4·10b&c): the shell continues to deform at a constant pressure. For $P < P_c^v$ (Fig. 4·10c), the (quasi-unstable) creep path (horizontal arrows in Fig. Fig. 4·10c) will eventually meet the stable long-term path (Fig. 4·10a, thick blue line). At a fixed pressure, the shell composed of a limited-creep material will rest in this configuration indefinitely.

Delayed buckling occurs between these two thresholds (see Fig. 4·10b): If the imposed

[5]For elastic shells, P is linearly related to the volume change ΔV up to buckling, with a proportionality constant of $P_c/\Delta V_c$. The critical volume according to elastic shell theory is $\Delta V_c = \frac{4\pi(1-\nu)}{\sqrt{3(1-\nu^2)}} R^2 h$, so $\frac{P_c}{\Delta V_c} = \frac{2E}{4\pi(1-\nu)} \frac{h}{R^4}$ [152]. Thus, the ratio of the slope of the instantaneous (elastic) equilibrium pressure-volume path to that of the long-term path is $(\frac{2E_0}{4\pi(1-\nu)} \frac{h}{R^4}) / (\frac{2E_\infty}{4\pi(1-\nu)} \frac{h}{R^4}) = \frac{E_0}{E_\infty} = 1/\bar{E}$.

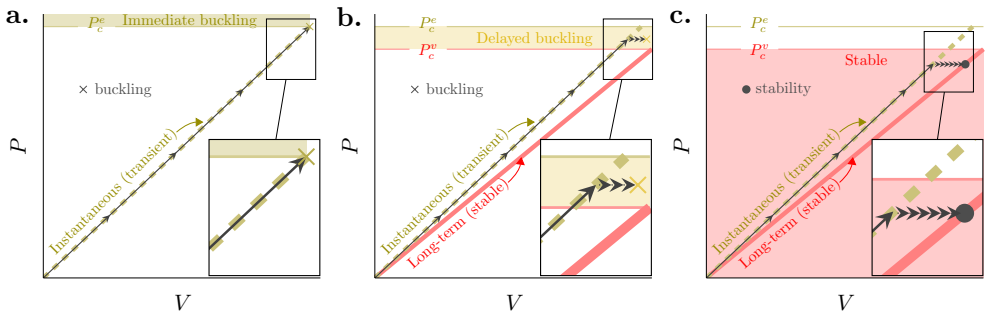

Figure 4·10: Theoretical plots of pressure versus volume change up to buckling for a spherical elastic shell with $E = E_0$ (dashed green line) or $E = E_\infty$ (solid, thick blue line in (b.)&(c.)), where we use our measured value of $\bar{E} = 0.91$. The black arrowed lines represent the response to step pressure loading, following Refs. [70, 71]. The instantaneous (dashed green) path is available at short times. (a.) If the imposed pressure $P \geq P_c^e$, this path leads directly to buckling. (b.) If $P < P_c^e$, the shell does not reach buckling before the elastic path ceases to exist. A "creep line" is followed (horizontal arrows), where the shell slowly deforms. If $P \geq P_c^v$, no stable path is available at later times and the shell eventually buckles. (c.) If $P < P_c^v$, the creep path (arrows) intersects the stable long-term path (solid red). The limited-creep shell rests in this deformed but unbuckled state indefinitely.

pressure difference $P \in [P_c^v, P_c^e)$, the long-term equilibrium path is unavailable. As such, deformation follows the creep line (horizontal arrows in Fig. 4·10b) to instability (yellow "x" in Fig. 4·10b), where creep collapse occurs after some time. This delay time varies significantly within this pressure range. As noted, in the main text, this theory provides a useful, straightforward way to determine the pressure threshold, but provides no information about deformation, and thus the critical time is not directly accessible. The defect analogy solves this problem.

Chapter 5

Efficient snap-through of spherical caps by applying a localized curvature stimulus

In the last chapter, our model offered a route to induce controllable buckling delays in elastomer shells. Next, we study the closely connected roles of mechanics and geometry in the snap-through instability of stimulus-responsive spherical caps. We focus on guiding the design of efficient snapping devices.

In bistable actuators and other engineered devices, a homogeneous stimulus (*e.g.* mechanical, chemical, thermal, or magnetic) is often applied to an entire shell to initiate a snap-through instability. In this work, we demonstrate that restricting the active area to the shell boundary allows for a large reduction in its size, thereby decreasing the energy input required actuate the shell. To do so, we combine theory with 1D finite element simulations of spherical caps with a non-homogeneous distribution of stimuli–responsive material. We rely on the effective *curvature stimulus*, *i.e.* the natural curvature induced by the non-mechanical stimulus, which ensures that our results entirely stimulus-agnostic. To validate our numerics and demonstrate this generality, we also perform two sets of experiments, wherein we use *residual swelling* of bilayer silicone elastomers – a process that mimics differential growth – as well as a magneto-elastomer to induce curvatures that cause snap-through. Our results elucidate the underlying mechanics, offering an intuitive route to optimal design for efficient snap-through.

5.1 Introduction

The spherical green alga *Volvox globator* swims thanks to thousands of synchronously flapping flagella. This motility is surprisingly hard-earned: after cell division, the flagella direct inward, toward the center of the sphere. Thus, the Volvox embryo must entirely invert itself during morphogenesis. To do so, cells in a “bend region" adopt a wedge-shape, which creates a localized curvature that leads to an eventual instability reminiscient of snap-through [66, 67]. Depending on the species, the bend region either propagates from the open phialopore (located at the pole), where four lips peel back to drive type-A inversion, or begins at the equator, where invagination leads to type-B inversion [77]. Arrested inversion of mutant Volvox has been linked to insufficient size of the bend region or intrinsic curvature therein [67].

Like the Volvox embryo – and indeed many other living organisms including, famously, the Venus fly trap [50] – engineers use snap-through instability of shell structures for functionality. Snapping releases stored elastic energy and does not require a continuously applied stimulus to maintain an inverted shape in bistable structures. Thus, snap-through instability is a particularly attractive mehanism for e.g. robotic actuators or mechanical muscles [165, 62], optical devices [79], and dynamic building façades [175]. Each relies on a combination of geometry-endowed bistability [178] and a snap-inducing stimulus to acheive its purpose. The stimulus can be mechanical – *e.g.* an indentation force [191], pressure [62], or torque from a child’s hands inverting a jumping popper toy [141] – or non-mechanical, *e.g.* temperature [92], voltage [165], a magnetic field [163], or differential growth [60, 114] or swelling [148]. An important connection between these wide-ranging stimuli is that each destabilizes a shell by generating a change in the shell’s curvature relative to its original, stress–free curvature.

In particular, non-mechanical stimuli alter the stress-free reference state, producing spontaneous or *natural curvature*. A classic example is the bimetallic beam of Timoshenko,

which curves as its two layers experience different expansive responses to an increasing thermal stimulus [181]. The natural curvature may be observed as the shape that a beam adopts when free of external constraints and exposed to a stimulus that causes this beam to bend. In plates or shells, however, the natural curvature is generally not achievable at all points in the slender structure. In such *non-Euclidean* [46] plates and shells, geometric incompatibility leads to residual stresses and often complex reconfiguration [102, 166]. Still, the relationship between a stimulus and the corresponding natural curvature it induces in a residually-stressed structures can be discerned *via* simple experimental methods based on the bending deformation of an equivalent beam. Calibration can be performed as an independent experiment, or in a manner similar to the *opening angle method*, wherein an axial slice exposes stresses induced by differential growth in tubular biological structures like arteries [2]. Thus, natural curvature serves as useful “effective" stimulus, allowing for generalization of these many non-mechanical, curvature-inducing stimuli. This concept was recently formalized within a non-Euclidean theoretical framework based on Koiter shell theory, revealing that the *curvature stimulus* behaves like a mechanical potential [148, 80].

Advanced functional devices actuated by curvature-inducing stimuli often require significant energy input, or have high material costs. Common commerically available dielectric elastomer (DE) films require up to $150\,\mathrm{V\,\mu m^{-1}}$, resulting in driving voltages in the kV range for most applications [137, 121]. Using less of these smart materials can decrease both cost and the likelihood of device failure. This need has inspired custom production of ultrathin electroactive films via methods like pad-printing [150] or electrospraying [192]. Clearly, it is desirable to reduce power requirements and material needs for DEs and other stimulus-responsive devices without requiring such efforts. As the localized bend region of the developing Volvox suggests, snap-through behavior may be preserved in spherical caps while the size of the active region – that is, the portion of the shell subjected to an arbitrary

curvature-inducing stimulus – is significantly reduced.

In the present work, we show that when the active portion is strategically placed, the magnitude of the stimulus need not increase, thus allowing for significantly reduced energy and material needs overall. We demonstrate this with 1D numerical simulations performed in COMSOL Multiphysics, wherein a curvature stimulus acts on a section of an otherwise passive shell. We validate our numerics with experiments, in which shells respond to different curvature-inducing stimuli – this also serves to demonstrate the generality of our findings. In one series of experiments, we rely on localized differential swelling of silicone elastomers, and in the second we use a magneto-active elastomer. Our numerical and experimental methods are described in Sect. 5.2. In Sect. 5.3 we present our results to answer the question: Is the active region more effective when placed in the bulk of the shell, or at the edge? Next, we ask: What is the the ideal size of the active region? In other words, what is the smallest active region that preserves snap-through behavior, without requiring the magnitude of the stimulus to increase? In Sect. 5.4 we present a scaling solution for the ideal size of the active region *via* energy minimization. These findings, which our data support, offer a mechanics-informed route to optimization. The underlying physics revealed prompt an additional examination of how the critical curvature scales with the active area in each configuration (Sect. 5.5), which adds rigor to the comparison presented earlier (in Sect. 5.3).

5.2 Methods

In this work, we study spherical caps in two configurations: “active bulk" (Fig. 5·1a), and “active boundary" (Fig. 5·1b). We refer to the angular depth of the shell measured from the pole as θ. The angular extent of the active region is denoted by θ_a, and is measured either from the pole or from the end of the passive region for the active pole and edge configurations, respectively. The shell thickness is given by h and the radius of curvature

by R. Below, we describe our numerical and experimental methods.

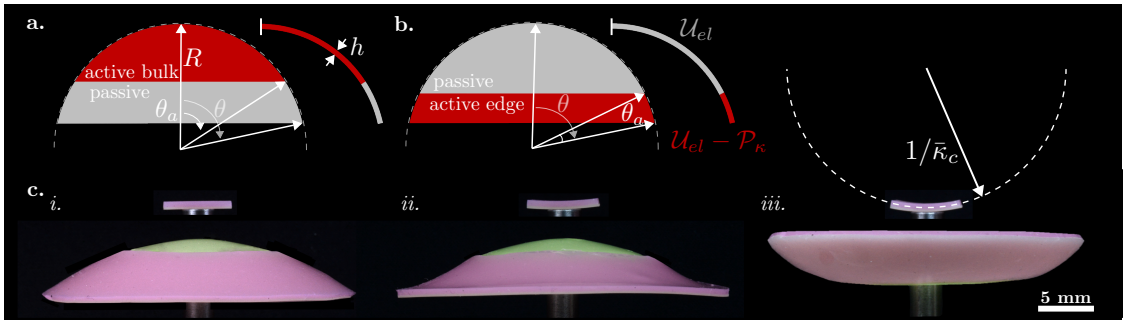

Figure 5·1: Schematics of the a. active bulk and b. active edge configurations of the partially active spherical cap, with corresponding profile curves used in FEM simulations. Relevant parameters are labeled: the angular shell depth θ measured from the pole, the angular size of the active (red) region θ_a, and the radius of curvature R and thickness h. As depicted in b., the COMSOL model minimizes the elastic energy U_{el} over the whole body, with an additional contribution from the curvature potential $\mathcal{P}_\kappa$ in the active region. c. Images from a typical experiment in the active edge configuration. In *i.*, the PVS beam (above), cut from the same cast as the partial bilayer shell (below) have just cured. The beam is free to adopt the curvature $\bar{\kappa} = 1/R + \kappa$, revealing the evolving natural curvature κ in active region of the shell. *ii.* In the bilayer region at the edge, the outer pink layer contracts while the green layer beneath it expands due to residual swelling. The resulting curvature (seen in the beam) creates a torque-like effect, causing the boundary of the shell to curl upward. The curvature evolves to a critical value $\bar{\kappa}_c$ when snap-through occurs, as shown in *iii.*

5.2.1 1D numerics

We performed finite element simulations in COMSOL Multiphysics 5.2. Following Refs. [148, 80], and because our experiments (Sect. 5.2.2) confirm that the shells we study retain rotational symmetry at least up to the point of snapping, the energy is minimized in the 1D profile curve of the shell. A circular segment with radius of curvature $R \in [9.65, 45.25]$ mm represents the midline of a spherical cap with an angular depth $\theta \in [0.52, 1.14]$ radians measured from the pole. This corresponds to $\theta/\sqrt{h/R} \in [2.2, 9.6]$, which covers most the range where curvature-induced snap-through occurs for fully active shells [148]. As

we discuss in Sect. 5.4, this parameter compares the depth of the shell to the characteristic size of its bending-dominated boundary layer, which becomes central to our analysis. The ratio θ_a/θ is between 0.3 and 1 for data presented herein, because we did not observe snapping for shells with $\theta_a/\theta < 0.3$. The shell thickness $h \in [0.5, 1.3]$ mm (so that to $h/R \in [0.015, 0.135]$) enters in the energy. The material is linear, elastic, isotropic, and has Poisson's ratio $\nu \in [0.25, 0.5]$. The Young's Moduli E_a and E_p of the active and passive regions were set to either $E_a = E_p \in [0.1, 20]$ MPa, or $E_a/E_p \in [0.005, 200]$. Despite that we assume a homogenous modulus (see Sect. 5.4, we observe no significant impact of the modulus on our results. A Dirichlet boundary condition is applied to the endpoint at the pole, while the edge end remains free.

Our model relies on the theoretical framework recently introduced by Pezzulla, *et al.* [148] and detailed further by Holmes *et al.* [80], which offers significant advantages for numerical energy minimization in the presence of non-mechanical stimuli. The authors demonstrate that in the absence of in-plane stretching of the middle surface, the curvature-inducing stimulus may be decoupled from Koiter's elastic energy and applied as a potential of the natural curvature κ. Thus, it is straightforward to selectively apply a curvature stimulus. The elastic energy ($\mathcal{U}_{el}$ in the schematic in Fig. 5·1b) must be minimized over the entire body, while the curvature potential $\mathcal{P}_\kappa \sim \kappa$ contributes to the total energy only in the active region. To capture the sudden, nonlinear snap-through instability, we use a custom arc-length method to vary the curvature stimulus κ [148]. A complete derivation of the equations used in COMSOL is provided in Ref. [80], and in Sect. 5.7.3.

5.2.2 Experiments

To validate our numerical results, we performed experiments in which shells are made, in part, of stimulus-responsive elastomers. To emphasize the generality of the curvature stimulus, we did this in two ways. In one set of experiments we used *residual swelling* of bilayer silicone elastomers [145, 146, 148, 176], wherein diffusion of free polymer chains causes

a geometric incompatibility resolved by curving. Deformation from residual swelling is growth-like and permanent. In additional experiments, we used magneto-active elastomers, which reversibly bend in response to a magnetic field. Below, we describe the methods used for each type of experiment.

5.2.3 Residual swelling experiments

It was previously demonstrated that residual swelling creates a curvature sufficient to drive inversion of full bilayer spherical caps [148]. In the present work, only a portion of the shell is subjected to residual swelling. Within this active region, we layer two polyvinylsiloxane (PVS) elastomers ($\nu = 0.5$), which we refer to as *green* (Zhermack Elite Double 32, E=0.96 MPa) and *pink* (Zhermack Elite Double 8, E=0.23 MPa). In a procedure detailed in Appendix 5.7.1, we cast the materials one-by-one in their fluid state over a metal ball bearing to form a nominally green cap with either a bilayer ring at the edge, or a bilayer cap at the pole. In the active region, the outer layer is pink (see Fig. 5·1c). After crosslinking (which occurs in about 20 minutes at room temperature), the pink elastomer is left with residual, uncrosslinked polymer chains. Thus, in the bilayer region where the pink and green material are in contact, there is a concentration gradient of free, polymer chains. To resolve this, chains flow from the pink to the green elastomer. As such, the pink region loses mass, or shrinks, while the green region grows. When this differential swelling occurs in an initially flat beam, the structure curves to accommodate the geometric mismatch, adopting the (evolving) natural curvature. In our spherical caps, the bilayer region around the boundary curls upward, forming a lip like that which appears when a jumping popper toy is inverted [141, 178]. Geometric constraints prevent the swelling bilayer cap from achieving its natural curvature, and the structure develops residual stresses as a result.

It is necessary that we measure the natural curvature in order to discern the magnitude of the curvature stimulus at a given time, which is central to our analysis. To do so, for the active edge experiments, we slice a small, vertical (initially curved) beam from the

material on the ball-bearing just below where the cut is made at the base of the spherical cap. The free, unconfined beam adopts a curvature $\bar{\kappa}$, which is the sum of the initial curvature $-1/R$ and the natural curvature κ. Thus, the (natural) curvature stimulus is $\kappa = \bar{\kappa} + 1/R$ [145, 146, 148]. We mount the shell and beam side-by-side and use a Nikon D610 DSLR Camera to take time-lapse images at a rate of one photo per minute. As residual swelling is a diffusive process, the time to deform scales with the square of the dimension across which swelling occurs [145]. In our experiments, that is the thickness h, and the shells in our experiments reach maximum deformation by about two hours post-cure. The critical curvature κ_c is identified in ImageJ by fitting a circle to the beam in the image when snap-through occurs (see Fig. 5·1c,iii.) – the radius of curvature is $1/\bar{\kappa}_c$. For the active bulk configuration, the beam is cut from the center of the shell immediately after snapping. Thus, unlike in the active boundary configuration where we track the natural curvature throughout deformation, only the critical curvature κ_c is obtained for these experiments. Residual swelling experiments produce curvatures up to $\kappa < \frac{1}{4h}$ [145, 146]. Deep shells require higher curvatures for snap-through [148], so the geometric range accessed in experiments is limited compared to simulations. We performed experiments with $h/R \in [0.02, 0.07]$, $\theta \in [0.58, 0.98]$ rad, and $\theta_a/\theta \in [0.38, 1]$.

5.2.4 Magneto-elastomer experiments

The magneto-active shells are fabricated using a similar bilayer casting approach to the residual swelling shells. In this case, the ferromagnetic active layer consists of iron oxide (Fe_3O_4) nanoparticles (Sigma-Aldrich 637106) mixed with green PVS at a weight ratio of 20%. A passive PVS cap is made first, followed by a ferromagnetic edge ring. Then, an additional PVS layer is added to join the two, resulting in a shell with relatively uniform thickness with a passive bulk and active edge. We did not study the active bulk configuration with magneto-elastomer shells. A 25.4mm cubic NdFeB magnet (N52 grade by SuperMagnetMan) is used to generate the magnetic gradient. The strength is measured by

the magnetic flux density $\mathcal{B}$, using a magnetometer (PCE Instruments Inc). The relative permeability and remanence of the NdFeB magnet are 1.04 and 1.45, respectively, giving $\mathcal{B} = 0.562$ T at the surface center of the magnets.

We tested five magnetic shells with with $h/R \in [0.02, 0.04]$, $\theta = 0.86$ rad, and an active boundary region such that $\theta_a/\theta \in [0.07, 1]$. The center of the magneto-active shell is mounted on a PVS column (diameter = 4.5 mm) to support the shell when magnetic field is applied. The NdFeB magnet is mounted vertically on Instron 5943 with a 5N load cell, then quasi-statically approaches the shell at a rate of 0.1 mm/s using the software Bluehill3. When the magnet reaches a critical distance from the shell, the magnetic body force acting on the ferromagnetic edge triggers snapping. The critical displacement is retrieved from the force-displacement curve. In order to find the corresponding critical $\mathcal{B}$, we simulate the magnetic field using the AC/DC module in COMSOL 5.6. This allows us to visualize the magnetic field and obtain $\mathcal{B}$ at given spatial points. To relate $\mathcal{B}$ to the curvature stimulus κ, we perform an additional set of experiments in which we measure the curvature in a ferromagnetic beam, oriented in the same direction as the edge of the shell, as the magnet approaches. For details on the magnetic field visualization and the magnetic flux-curvature calibration, see Appendix 5.7.2.

5.3 Comparison of active bulk and boundary

In Fig. 5·2, we compare the critical curvature κ_c to that for a fully active shell, $\kappa_c^{full} \equiv \kappa_c(\theta_a = \theta)$, for varied proportions of the angular active area to the total angular depth of the shell, θ_a/θ. In the active bulk configuration, a reduction of only about 5 percent in θ_a/θ causes the critical curvature κ_c to increase significantly above κ_c^{full}. Meanwhile, we observe that when the boundary is active and the passive region lies in the bulk, the active portion can be reduced to as low as 40 percent in some cases without requiring $\kappa_c/\kappa_c^{full} > 1$ for snap through.

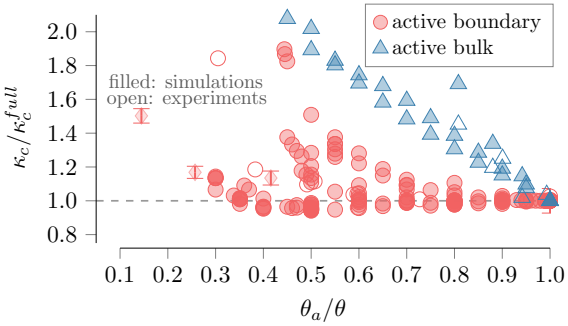

Figure 5·2: Comparison of the critical curvature κ_c compared to that for a fully active shell, $\kappa_c^{full} = \kappa_c(\theta_a = \theta)$, for varied sizes of the active region in the active bulk (blue triangles) and active boundary (green circles) configurations. Our results show a clear preference for the active boundary configuration: θ_a/θ can be reduced to as low as about 0.4 without requiring a higher curvature stimulus for snap-through, whereas if the bulk is active (and the boundary is passive), $\kappa_c/\kappa_c^{full} > 1$ for any $\theta_a/\theta < 1$. Error bars correspond to one standard devation, and are smaller than markers in all cases except the magneto-active experiments.

As discussed in Sect. 5.2.1, it has been shown that a stimulus which induces intrinsic curvature may be treated as a *curvature potential*, which is decoupled from Koiter's elastic energy [148]. Pezzulla *et al.* demonstrate that this curvature potential may be further decomposed into two work-like terms, *i.e.* $\mathcal{P}_\kappa = -\mathcal{W}_{bulk} - \mathcal{W}_{edge}$, which behave like an applied pressure in the bulk and a torque on the boundary. The pressure-like term scales as:

$$\mathcal{W}_{bulk} \sim h^4\kappa^2(1-\cos\theta), \tag{5.1}$$

and the torque-like term as:

$$\mathcal{W}_{edge} \sim h^4\kappa^2\left(\frac{R}{h}\right)^{3/2}\sin\theta. \tag{5.2}$$

Comparing the two contributions gives

$$\left|\frac{\mathcal{W}_{edge}}{\mathcal{W}_{bulk}}\right| \sim \frac{(R/h)^{3/2}}{\tan(\theta/2)} >> 1, \tag{5.3}$$

showing that the edge work dominates in thin shells [148].

The implication explains our findings in general: removing a portion of active area from the edge weakens the effect of the curvature stimulus more than if the same amount of area were removed from the bulk. Conversely, the inequity suggests that the active edge configuration is the more efficient choice for the design of structures that will snap with minimal energy needs. To clearly distinguish between these regimes, henceforth we will refer to the critical curvature in the active boundary configuration as κ_c^{edge}, and that in the active bulk configuration as κ_c^{bulk}. Despite this clear preference for an active boundary, the optimal size of the active region is not clear from the scattered data in Fig. 5·2. We investigate this in the following section.

5.4 Optimal size of active boundary *via* energy minimization

To discern the most efficient size of the active region at the shell boundary, we minimize the total potential energy in the system $\mathcal{U}$, which consists of the internal elastic energy, and the non-mechanical loading due to curvature [148, 80, 114]. In the latter, the torque-like contribution at the boundary dominates over the pressure-like effect in the bulk. This effect is amplified in the active edge configuration, as some or all of the bulk is passive. Accordingly, we observe very small bulk deformation compared to boundary rotation (see Fig. 5·5b.) As such, we neglect the pressure-like contribution in the bulk, but include the additional torque that arises at the boundary between the active and passive regions (Fig. 5·3a). This gives:

$$\mathcal{U} = \mathcal{U}_K - \oint_{out} B(1+\nu)\kappa(\Delta\beta_{out})\, d\mathring{s} - \oint_{in} B(1+\nu)\kappa(-\Delta\beta_{in})\, d\mathring{s} \tag{5.4}$$

where $\mathcal{U}_K$ is the Koiter shell energy [106], B is the bending rigidity, $\Delta\beta_{out}$ and $\Delta\beta_{in}$ are the angle change at the boundary and the active-passive interface, respectively, and $d\mathring{s}$ is the line element. The second and third terms quantify the torque-like contribution of the

non-mechanical loading induced by the natural curvature at either end of the active edge region. Note that a positive angle change corresponds to a counter-clockwise rotation.

Because we expect axisymmetric deformation up to snap-through, these non-mechanical loading terms can be collected into the free boundary line integral as

$$\mathcal{U} = \mathcal{U}_K - \oint_{out} B(1+\nu)\kappa\Delta\beta_{out}^{eq}\, d\mathring{s} \tag{5.5}$$

where $\Delta\beta_{out}^{eq} = \Delta\beta_{out} - \Delta\beta_{in}\left(1 - \frac{\theta_a}{\theta}\right)$. Physically, this corresponds to transforming the shell into an equivalent one that experiences only the angle change $\Delta\beta_{out}^{eq}$ at the boundary, and is fully active, *i.e.* the natural curvature κ acts on the whole body (see Fig. 5·3b). Then, from Ref. [148], we can postulate that the snapping occurs when the colatitude-direction tangent vector at the boundary of the equivalent shell approximately becomes horizontal, *i.e.* at $\Delta\beta_{out}^{eq} \sim \theta$. Note that this does not imply that $\Delta\beta_{out} \sim \theta$, which as we discuss in Sect. 5.5, is not necessarily the case.

For thin surfaces where the non-mechanical stimulus acts through-the-thickness, the contribution of the mid-surface stretch induced by the stimulus can be neglected [148, 80]. Then, assuming the colatitude-direction bending strain is much larger than the azimuthal one, the shell energy $\mathcal{U}$ scales as

$$\mathcal{U} \sim \frac{B}{2}\left(b_1^1\right)_p^2 A_p + \frac{B}{2}\left(b_1^1\right)_a^2 A_a - B(1+\nu)\kappa\left[\Delta\beta_{out} - \Delta\beta_{in}\left(1 - \frac{\theta_a}{\theta}\right)\right](2\pi R\theta) \tag{5.6}$$

where b_1^1 is the characteristic curvature in the colatitude-direction and the subscripts p and a denote the passive bulk and active edge regions. The curvature b_1^1 can be estimated as the angle change along an arc over its length, so that $(b_1^1)_p \sim \frac{-(\theta-\theta_a-\Delta\beta_{in})}{R(\theta-\theta_a)}$, and $(b_1^1)_a \sim \frac{-(\theta_a+\Delta\beta_{in}-\Delta\beta_{out})}{R\theta_a}$. The active area $A_a \sim 2\pi R^2\theta\theta_a$, and the passive area $A_p \sim \pi R^2\theta^2 - A_a$.

Inserting these scalings and minimizing Eq. (5.6) with respect to $\Delta\beta_{in}$ and $\Delta\beta_{out}$ – that is, setting $\partial\mathcal{U}/\partial\Delta\beta_{out} = \partial\mathcal{U}/\partial\Delta\beta_{in} = 0$ – gives the solutions for these angle changes in the deformed configuration. Evaluating the result at the presumed point of instability,

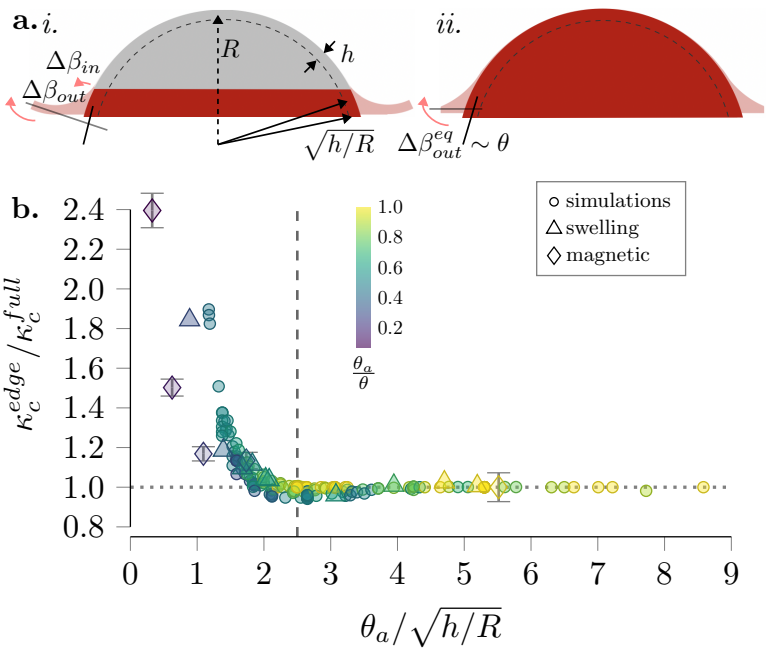

Figure 5·3: a. Schematic of the energy minimization scheme.*i.* shows the partially active shell, where κ delivers a torque-like effect (pink arrows) along the free boundary and at the active-passive interface, which drives the tangent to the edge (black line) to rotate an amount $\Delta\beta_{out}$ (to the gray line) and that at the interface a smaller amount $\Delta\beta_{in}$. The characteristic angular size of the natural boundary layer, $\sqrt{h/R}$ is labeled. *ii.* The equivalent fully active shell, which feels a torque from the curvature stimulus only about the free edge. Fully active shells snap-through when the tangent to the edge becomes approximately horizontal [148]. b. The normalized critical curvature for the active edge configuration *vs.* the active area θ_a compared to its theoretical optimal size θ_a^*, according to: (inset) the scaling result Eq.(5.9), and (main plot) the empirically-corrected expression given in Eq.(**??**). The minimum of $\kappa_c^{edge}/\kappa_c^{full}$ occurs at $\theta_a = \theta_a^*$, supporting the conclusion that the optimal size for the active boundary region coincides with the characteristic length of the natural boundary layer, up to a factor of $2(1+\nu)^{1/2}$. Error bars mark one standard devation, and are smaller than markers in residual swelling experiments and simulations.

$\Delta\beta^{eq}_{out} \sim \theta$, gives the critical natural curvature of the partially active shell at snapping as:

$$\kappa_c^{edge} \sim \frac{\theta}{\theta_a(1+\nu)R}. \tag{5.7}$$

Assuming the minimum critical curvature occurs at $\kappa_c = \kappa_c^{full}$, where from Ref. [148]:

$$\kappa_c^{full} \sim \frac{\theta}{(1+\nu)\sqrt{Rh}}, \tag{5.8}$$

we find that the optimal size of θ_a should scale as:

$$\theta_a^* \sim \sqrt{h/R}. \tag{5.9}$$

This result is shown in the Fig. 5·3c. We see a promising collapse of our data, and a minimum emerges at about 2.5 on the horizontal axis, indicating that the true optimal $\theta_a^* \approx 2.5\sqrt{h/R}$ for our shells, which vary in geometry, E, and ν. We note that for moderately deep shells, we observe critical curvatures even below the predicted κ_c^{full} (as low as $\kappa_c = 0.95\kappa_c^{full}$, for a shell depth $\theta/\sqrt{h/R} = 5.3$ when $\theta_a/\theta = 0.5$). We suspect that this results from additional destabilizing effects delivered by the torque at the active-passive interface, which tends to help flatten the bulk of the shell. We note that magneto-elastomer shells carry more error than the residual swelling experiments and simulations. This is largely due to the non-uniform magnetic gradient generated from the NdFeB magnet. Additionally, the shells are highly sensitive to fabrication errors, which can result in a nonuniform ferromagnetic boundary, when θ_a is small.

The result of our energy minimization scheme given in Eq. (5.9) coincides with the angular length scale of the bending-dominated *boundary layer* [51, 135] for a spherical cap, $\sqrt{h/R}$. In open shells, the characteristic length of the boundary layer is that which is close enough to the edge that the thickness “feels" relatively large in comparison [45]. In this region the energy balance shifts (thin shells are nominally stretching energy-dominated, preferring isometry), and so does the preferred deformation mode. The boundary layer is readily observed as the lip that curls upward when a spherical cap of finite thickness, *e.g.* a tennis ball sliced in half, is everted [178, 78]. In this region, the shell “tries" to return to its initial state, resolving some of the stress that arises due to stretching above the midline and

compression below it. Only if the boundary layer is large compared to the shell depth is the everted shell unstable, snapping back to its undeformed configuration. If the boundary layer is relatively small, the shell is bistable and can rest in its everted state indefinitely.

This scenario appears to be analogous to the non-everted, partially active shells we study: if the bending region is large, snap-through occurs easily, whereas a shell with a small active region is stable even against a higher stimulus. This points to an intuitive interpretation of our results: generally speaking, in the active edge configuration, if the active area meets or exceeds the boundary layer, the region predisposed to bending may do so. As a result, snapping is unaffected compared to a fully active cap. For $\theta_a < \theta_{bl}$, we interfere with the boundary layer – this can be seen as reducing the size of the effective boundary layer – and higher curvatures are required to drive snap-through. The efficacy of the geometric design, in sum, depends on how the effective boundary layer set by θ_a, where we *impose* bending, relates to the natural boundary layer that scales as $\sqrt{h/R}$, where the shell *prefers* bending. In the active bulk configuration, any $\theta_a < \theta$ disturbs the boundary layer, forcing the critical curvature upward. Thus, this interpretation also clarifies what we saw in Sect. 5.3. This prompts us to briefly revisit our comparison of the active bulk and boundary configurations.

5.5 Scalings for the critical curvature based on fully active shells

In light of the importance of the boundary layer discussed in Sect. 5.4, we may add rigor to our claim that the active boundary configuration is more efficient than the active bulk (Sect. 5.3). To do so, we rely on the established result [148] (from which we determined Eq. (5.8)) that the critical curvature for fully active shells scales as:

$$\kappa_c^{full} R \sim \frac{\theta}{(1+\nu)\sqrt{h/R}}. \tag{5.10}$$

This finding leans on the assumption that the pressure-like effect of curvature in the bulk may be negelected due to the dominant effect of curvature on the boundary, which we have similarly employed in Sect. 5.4. Additionally, it assumes based on empirical observations that the tangent vector to the boundary becomes approximately horizontal at the point of snap-through [148, 114].

In the active bulk configuration, we reduce size of the effective boundary layer. Accordingly, we observe that the tangent to the edge of the effective boundary layer – that is, the active-passive interface, and not the edge of the shell – becomes approximately horizontal at the point of snap-through. Assuming the effective angular width of the boundary layer scales as $(\theta_a/\theta)\sqrt{h/R}$, it follows from Eq. (5.10) that:

$$\kappa_c^{bulk} R \sim \frac{\theta^2}{\theta_a(1+\nu)\sqrt{h/R}}, \qquad \theta_p < \theta_{bl} \tag{5.11a}$$

$$\frac{\kappa_c^{bulk}}{\kappa_c^{full}} \sim \frac{\theta}{\theta_a}, \qquad \theta_p < \theta_{bl} \tag{5.11b}$$

where $\theta_p = \theta - \theta_a$ represents the passive portion of the shell. Eqs. (5.12a) and (5.12b) are shown in Fig. 5·4a&b, respectively. where indeed we see that the critical curvature increases linearly with θ/θ_a until the passive region reaches the approximate size of the boundary layer. At this point, where the entire boundary layer is inactive, the assumption that the edge work outweighs the bulk work breaks down and the critical curvature diverges.

For completeness, we also study the implications of Eq. (5.10) on shells with active boundaries. In Sect. 5.4 we used the horizontal tangent assumption ($\Delta\beta_{out}^{eq} \approx \theta$) for the equivalent fully active shell. We observe that for shells in the active edge configuration, this assumption breaks down, *i.e.* $\Delta\beta_{out} > \theta$, if θ_a approaches the size of the boundary layer (see Fig. 5·5). With this in mind, we expect as long as the coincident conditions that boundary layer is intact and the boundary tangent is approximately horizontal at snap-through ($\theta_a >> \sqrt{h/R}$), due to the dominance of the edge work we expect no change to

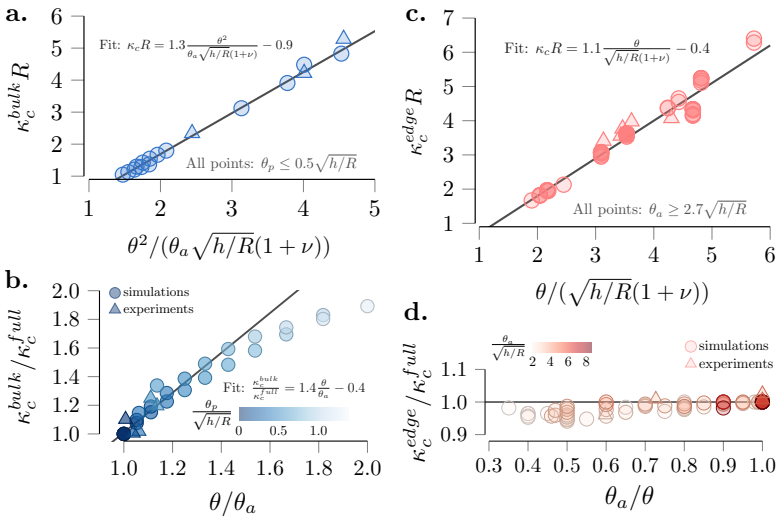

Figure 5·4: a. When the active portion of the shell is in the bulk, the size of the effective boundary layer is reduced. As a result, the critical curvature increases according to Eq. (5.11b), and any reduction in θ_a (greater than 1 on the x-axis) increases the the curvature stimulus κ_c^{bulk} required for snap-through, as shown in b. As Eq. (5.11a) predicts, the stimulus increase scales linearly with θ/θ_a when the passive edge region is smaller than the boundary layer size (darker blue points, $\theta_p/\sqrt{h/R} \lessapprox 0.5$; fit corresponds to this range.) c. If instead the boundary of the shell experiences the curvature stimulus, as long as θ_a exceeds the boundary layer, the behavior follows that of the fully active shell, *i.e.* Eq. (5.12a) [148]. d. As such, θ_a can be reduced to as much as 0.35θ before the critical curvature increases above that for a fully active shell, κ_c^{full}, in agreement with Eq. (5.12b).

the critical curvature from κ_c^{full}. That is,

$$\kappa_c^{edge} R \sim \frac{\theta}{(1+\nu)\sqrt{h/R}}, \qquad \theta_a > \theta_{bl} \tag{5.12a}$$

$$\frac{\kappa_c^{edge}}{\kappa_c^{full}} = 1, \qquad \theta_a > \theta_{bl} \tag{5.12b}$$

Note that Eq. (5.12b) is complementary to the result Eq. (5.7). Eqs. (5.12a) and (5.12b) are shown in Fig. 5·4c&d, respectively. Comparing Eqs. (5.11b) and (5.12b) confirms that for any small to moderate reduction of the active area, the active bulk configuration requires a higher curvature stimulus than the active boundary.

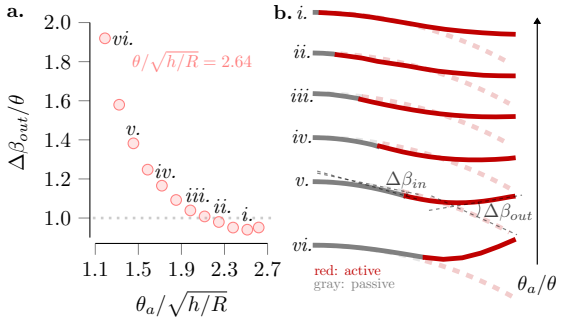

Figure 5·5: a. When the active area is larger than the boundary layer, the edge tangent requires a rotation $\Delta\beta_{out} \sim theta$ to snap through, which results in an approximately horizontal tangent. For $\theta_a \lessapprox 2\sqrt{h/R}$ in this case, the tangent undergoes additional rotation to trigger instability. Data is from simulations of a fixed shell geometry with changing active area. Roman numerals correspond to b., which shows the the initial (dashed) and pre-snap (solid) profile curves for $\theta_a/\theta = 0.95, 0.85, ..., 0.45$. The angle changes $\Delta\beta_{out}$ and $\Delta\beta_{in}$ are shown in *v.* The angle change $\Delta\beta_{out}$ increases from 0.35 rad in *i.* to 0.82 rad in *vi.*

5.6 Conclusion

The aim of the present work was to guide the design of efficient snapping structures, which simultaneously minimize the active area and the magnitude of stimulus needed. We studied partially active spherical caps in two configurations – active bulk and active boundary – with a combination of theory, 1D finite element simulations, and experiments. Shells respond to a non-mechanical, curvature-inducing stimulus in the designated active region, but are passive elsewhere.

Our mechanics-informed approach uncovered an analogy to the bending-dominated boundary layer in inverted spherical caps. This offered an intuitive interpretation of our work: selectively applying curvature amounts to setting the size of an effective boundary layer. Like for inverted, passive spherical caps, the size of the (effective) boundary layer is closely tied to stability [178]. Further, the location and size of the imposed bending region determines whether it competes or cooperates with the geometric boundary layer, wherein the shell inherently “wants" to bend. With this view, the design principles that follow are

straightforward. In the active cap configuration, some or all of the boundary layer is made passive, making snap-through harder to acheive. As a result, the active edge configuration is preferred for efficient snapping. The size of the optimal active region reaches scales with that of the natural boundary layer (Eq. (**??**)), with an empirical prefactor of about 2.5 for our shells.

We demonstrated the efficacy and generality of our findings using residually swelling and magneto-active shells. As we have shown, the curvature stimulus [148] may be easily mapped to any non-mechanical load, so we expect that these principles will apply widely to bistable actuators made of *e.g.* electro-active, thermally activated, or pneumatic materials.

In our energy minimization scheme (Sect. 5.4), we assumed that the minimimum curvature stimulus was that for the fully active shell. This allowed us to identify the minimizing active area. However, we observed critical curvatures even below this value. We speculate that depending on the geometry, the torque at the active-passive interface can help to destabilize the shell – despite that it ostensibly acts in opposition to the edge torque. We leave investigation of this effect, which may open the door to further reduction of the critical curvature, for future work.

5.7 Supplemental Information

5.7.1 Fabrication of non-homogenous residual swelling shells

The shell fabrication procedure for the active edge configuration is shown in Fig.5·6. The process is as follows: To begin, we coat a metal ball-bearing ($R_{sphere} \in [12,75]$ mm) with viscous polydimethylsiloxane (PDMS), ensuring a relatively uniform thickness [112]. Once the PDMS has cured, we use a laser-cut (Epilog Laser Helix, 75W) ring (inner radius $R_p \in [2,65]$ mm) as a stencil to guide a cut around the sphere's perimeter, resulting in a cap of opening angle $\theta_p = \theta - \theta_a = \sin^{-1}(R_p/R_{sphere})$.

Next, we coat a ball bearing of the same size with green polyvinylsiloxane (PVS)

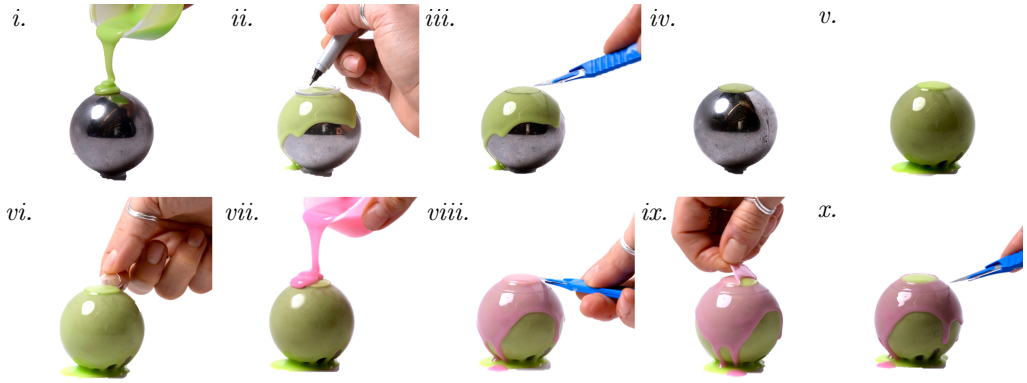

Figure 5·6: a. The fabrication process for a nonhomogeneous spherical cap with active edge: *i.* A layer of viscous green PVS is deposited over spherical metal ball-bearing. *ii.* After curing, a ring of radius R_p is centered at the top of the sphere and used as a stencil to mark θ_p. *iii.* A cut is made and *iv.* excess material is removed, leaving a green layer of angular width $0 \leq \theta \leq \theta_p$. *iv.* A second green layer is added. *v.* Once the green layer is cured, a PDMS cap (cut from a sphere of the same size, in the same manner as i.-iv.) of radius R_p is centered at the top of the sphere. *vii.* A pink layer of VPS is added. *viii.* After curing, a shallow cut allows for the removal *ix.* of the pink layer and the PDMS in the region $0 \leq \theta \leq \theta_p$. *x.* A cut is made at θ (following a line which was stenciled by a ring as in *ii*) through all material to free the shell from the ball bearing. A small beam is cut vertically from just below the shell.

(Fig. 5·6a,i) and again make a cap with opening angle θ_p. This time, the cap remains in place and the excess material is removed (Fig. 5·6a,iv). Since the active section is necessarily bilayer, this additional passive layer ensures a relatively homogeneous thickness throughout the shell.

With the green cap in place, a second layer of green PVS is added in the same manner (Fig. 5·6a,v) and cut to the edge angle, $\theta \geq \theta_p$. It fuses completely to the first layer, so in the bulk (the eventual passive region, up to θ_p) the material is thicker than at the edge at this stage of fabrication.

After the second green PVS layer has cured, the PDMS cap is centered at the north pole (Fig. 5·6a,vi) – it adheres to but does not fuse with the PVS. Next, we deposit a layer of pink PVS (Fig. 5·6a,vii). As soon as the pink is cured, a shallow cut is made around the

edge of the PDMS cap (at θ_p) (Fig. 5·6a,viii). Since the PDMS prevents crosslinking in the region it covers, we can peel the pink layer and the PDMS from this section (Fig. 5·6a,ix).

Another laser cut ring ($R \in [6,75]$ mm, $R > R_p$) is used to guide a deeper cut through both layers, forming the bottom boundary (Fig. 5·6a,x) – this sets the total opening angle of the shell to be $\theta = \sin^{-1}(R/R_{sphere})$. We are left with a spherical cap composed of only green PVS (two layers thick) from opening angle 0 to θ_p, and a bilayer ring of angular width $\theta_a = \theta - \theta_p$ at the edge. In order to quantify the evolving curvature stimulus, we slice a small vertical beam from the material that remains on the ball-bearing just below the cut.

A shell with an active cap region is made in much the same way, except that the protective PDMS layer is a ring around the edge of the cap. This method prevents excision of a reliable bilayer beam from the region beneath the cut, so the curvature was not measured throughout the swelling process. Instead, a beam was cut from the cap region immediately following snapping. Because the curvature develops at a much slower rate than that of snap-through, the difference between the curvature immediately before and after snapping is negligible.

5.7.2 Magnetic flux density as a curvature stimulus

In order to visualize the magnetic field and obtain the magnetic flux density $\mathcal{B}$ at given spatial points, we simulate the magnetic field using the AC/DC module in COMSOL 5.6 (see Fig. 5·7). The finite element model is calibrated with experimental measurements and material properties provided by the manufacturer. The critical $\mathcal{B} = \mathcal{B}_c$ at the edge of the shell at the point of snapping was calculated by inputting the critical displacement (meaured from the Instron experiments) to the FE simulation.

To obtain the relationship between the applied magnetic flux density and corresponding natural curvature of the shell, we fabricated a beam of length 6.1 mm, width 0.88 mm, and thickness $h = 0.42$ mm. The beam is cut from the same spherical ball bearing as the shells,

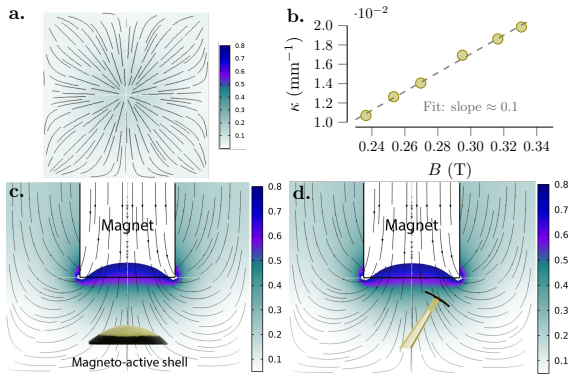

Figure 5·7: a. Finite element simulation showing the axially symmetric magnetic field generated from the NdFeB magnet. b. Calibration curve for magnetic flux density $\mathcal{B}$ *vs.* the curvature stimulus κ, based on measurements taken from the beam in d. c. Magneto-active shell in the magnetic field. d. Magneto-active beam the magnetic field, which is oriented to match the edge of the shell and used to calibrate the κ–$\mathcal{B}$ relationship. In our range the relationship is approximately linear, and for our shells we used the empirical fit indicated by the dashed line.

so the initial curvatures are equivalent ($1/R = 0.0787$ mm^{-1}). The arch is oriented at 0.639 rad with respect to the vertical center line to match the position of the corresponding ferromagnetic layer in the magnetic field (see Fig. 5·7c&d.) The magnetic field is generated using the same cubic NdFeB magnet as is used for the shell. Digital image processing is used to measure the change of curvature as we vary the distance between the magnet and the bottom edge of the beam. The distance is then converted to magnetic flux density $\mathcal{B}$ using the COMSOL FE simulation. The response curvature as a function of the applied magnetic flux density over the range relevant to our experiments is shown in Fig. 5·7b. In our range, a first order polynomial fits the data. We note that the intercept of our empirical fit, which has a slope of 0.097, is not zero, indicating that a linear fit would not be sufficient over a larger range.

5.7.3 The curvature potential & derivation of COMSOL model

Recall from Chapter 1 that Koiter's elastic energy may be written as:

$$\mathcal{U}_K = \underbrace{\frac{Y}{2}\int \left[(1-\nu)\gamma^{\alpha\beta}\gamma_{\alpha\beta} + \nu(\gamma^{\alpha}_{\alpha})^2\right] d\omega}_{\text{stretching}} + \underbrace{\frac{B}{2}\int \left[(1-\nu)\rho^{\alpha\beta}\rho_{\alpha\beta} + \nu(\rho^{\alpha}_{\alpha})^2\right] d\omega}_{\text{bending}} \tag{5.13}$$

where for a homogenous shell the stretching and bending rigidities are $Y = \frac{Eh}{1-\nu^2}$ and $B = \frac{Eh^3}{12(1-\nu^2)}$, respectively, with Young's modulus E and Poisson's ratio ν. The midsurface strain tensor is $\gamma_{\alpha\beta} = \frac{1}{2}(a_{\alpha\beta} - \mathring{a}_{\alpha\beta})$, and the curvature strains are quantified by the tensor $\rho_{\alpha\beta} = b_{\alpha\beta} - \mathring{b}_{\alpha\beta}$. The superscript "o" refers to the initial configuration, whereas no subscript denotes the current (deformed) state. The first fundamental form **a** quantifies distances between points, and the second fundamental form **b** accounts for curvatures.

As discussed in the main text, the potential from a curvature-inducing stimulus can be decoupled from Koiter's energy, so that the elastic energy takes the following form [148]:

$$\mathcal{U} = \mathcal{U}_K - \frac{Y}{2}\int \frac{1+\nu}{6}\kappa h^2 \rho^{\alpha}_{\alpha} d\omega \tag{5.14}$$

where $\mathcal{U}_K$ is (5.13), and the last term represents the curvature potential, where κ is the evolving natural curvature.

To describe the undeformed (pre-swelling) shell, we first adopt the usual parameterization for a spherical surface of radius R:

$$\mathring{\mathbf{r}}(\phi,\psi) = (R\cos\psi\sin\phi, R\sin\psi\sin\phi, R\cos\phi). \tag{5.15}$$

Here, ϕ is the polar angle ($0 \le \phi \le \pi$) and ψ the azimuth ($0 \le \psi < 2\pi$). (For background on the concepts from differential geometry that follow, see Appendix A.) The metric tensor (first fundamental form) is then given by:

$$\mathring{\mathbf{a}} = \begin{pmatrix} R^2 & 0 \\ 0 & R^2\sin^2\phi \end{pmatrix}, \tag{5.16}$$

and the curvature tensor, or second fundamental form, is

$$\mathring{\mathbf{b}} = \begin{pmatrix} -R & 0 \\ 0 & -R\sin^2\phi \end{pmatrix}. \tag{5.17}$$

We observe that up to the point of snapping (and, for shallower shells, after snapping), the deformed shapes maintain the sphere's rotational symmetry, and vary in shape only with respect to the polar angle [148]. The deformed shell can thus be parameterized (as a surface of revolution) in terms of functions f and g of ϕ:

$$\mathbf{r}(\phi,\psi) = (f(\phi)\cos\psi, f(\phi)\sin\psi, g(\phi)). \tag{5.18}$$

Then the metric for deformed spherical shells is

$$\mathbf{a} = \begin{pmatrix} f_{,\phi}^2 + g_{,\phi}^2 & 0 \\ 0 & f^2 \end{pmatrix}. \tag{5.19}$$

The curvature tensor is

$$\mathbf{b} = \frac{1}{\sqrt{f_{,\phi}^2 + g_{,\phi}^2}} \begin{pmatrix} g_{,\phi\phi}f_{,\phi} - f_{,\phi\phi}g_{,\phi} & 0 \\ 0 & fg_{,\phi} \end{pmatrix}. \tag{5.20}$$

The forms of (5.19) and (5.20) with (5.14) result in a second-order energy functional. To reduce the functional to first-order, we use the substitution $g'(\phi) = f'(\phi)\zeta(\phi)$ [46, 148] so that (5.19) and (5.20) become:

$$\begin{aligned} \mathbf{a} &= \begin{pmatrix} f_{,\phi}^2(1+\zeta^2) & 0 \\ 0 & f^2 \end{pmatrix} \\ \mathbf{b} &= \frac{1}{\sqrt{f_{,\phi}^2(1+\zeta^2)}} \begin{pmatrix} \zeta_{,\phi}f_{,\phi}^2 & 0 \\ 0 & \zeta f f_{,\phi} \end{pmatrix}. \end{aligned} \tag{5.21}$$

We impose the weak form of Koiter's energy (comprised of bending and stretching with no inelastic stimuli) upon the entire domain, with the additive curvature potential term only

acting in the active region. For the active edge configuration, with w_{Koiter} as the strain energy density, the equations (weak forms) to enforce are:

$$
\begin{aligned}
0 &= \int_0^{\theta} \frac{\partial}{\partial f}(w_{Koiter}) \cdot \tilde{f} + \frac{\partial}{\partial f'}(w_{Koiter}) \cdot \tilde{f}' \, d\theta \\
0 &= \int_0^{\theta} \frac{\partial}{\partial \zeta}(w_{Koiter}) \cdot \tilde{\zeta} + \frac{\partial}{\partial \zeta'}(w_{Koiter}) \cdot \tilde{\zeta}' \, d\theta \\
0 &= \int_{\theta-\theta_a}^{\theta} \frac{\partial}{\partial f}(p_{Pk}) \cdot \tilde{f} + \frac{\partial}{\partial f'}(p_{Pk}) \cdot \tilde{f}' \, d\theta \\
0 &= \int_{\theta-\theta_a}^{\theta} \frac{\partial}{\partial \zeta}(p_{Pk}) \cdot \tilde{\zeta} + \frac{\partial}{\partial \zeta'}(p_{Pk}) \cdot \tilde{\zeta}' \, d\theta.
\end{aligned}
\tag{5.22}
$$

Here, tildes denote test functions of the two unknowns, and p_{Pk} is the potential energy density of the natural curvature, given explicitly as the integrands of (5.13) and (5.14). The strains are calculated from the differences between (5.21) and (5.16)-(5.17). In the active bulk configuration, integration of the curvature potential equations (the last two lines of Eq. (5.22)) is from 0 to θ_a.

Chapter 6

Conclusion

The goal of this thesis was to advance our fundamental knowledge of how slender structures respond to confinement and stimuli, which can inform the design of shape-shifting devices. This was approached through four projects.

In Chapter 2, we used experiments, FE simulations, and a simple scaling model to study the global response of shells of varied Gaussian and mean curvatures to planar confinement. We found that the shells all buckle circumferentially, adopting a wavenumber that can be captured by a single geometric parameter which relates the overall size of the shell to the length scale associated with confinement.

In Chapter 3, we constrained intrinsically flat sheets to remain planar in their central region as they are forced through a ring. The sheets would form a single d-cone in the absence of added planar confinement. We saw in experiments and MD simulations that the additonal constraint forces the sheet to buckle periodically, which is acheived through striking sequential dynamics. We provided a scaling for the critical force at which the first wave forms, which was rationalized in the context of pressure buckling of an encased ring. From this, we determined a scaling based on energy minimization that shows how the buckling wavelength of this *annular d-cone* depends on the geometric parameters of the system. Together, Chapters 2 & 3 underscore the sensitivity of slender structures to small changes in confinement geometry.

Next, in Chapter 4, we studied the delayed buckling of step-loaded, defect-seeded elastomer spherical shells, which occurs in experiments at ostensibly sub-critical loads. We

show that the reduced pressure threshold can be determined directly from the viscoelastic material properties. Then, we introduced an analogy between viscoelastic creep deformation and an evolving defect in an equivalent elastic shell. This allowed us to capture the critical pole deflection and the critical time associated with buckling. This work was primarily addressed to the elastic buckling community: Our model for creep buckling maintains close ties to the concepts of elastic shell buckling, and relies on quantities which are readily determined in experiments, thus offering a route to incorporate tunable time delays in the design of elastomer devices.

Finally, in Chapter 5, we demonstrated with theory, 1D FE simulations, and two sets of experiments, that for efficient snapping actuation, a non-mechanical stimulus need only be applied near the boundary of a spherical cap. We showed that the optimal size of the active region coincides with the bending-dominated boundary layer inherent to the shell. This result offers an intuitive route to the design of bistable actuators with reduced energy input. Thus, Chapters 4 & 5 both demonstrate how mechanics can instruct the design of shape-shifting devices.

6.1 Future directions

Each of the studies presented in the last four Chapters raise new questions, which point to possible directions for future research. Some of these ideas are discussed below.

6.1.1 Geometrically confined shells

In Chapter 2, we focused on capturing the general behavior of confined shells. We highlighted the commonalities in the response to planar confinement for four types of shells: saddles, rolled sheets, cylinders, and spherical segments. We studied the confined saddles in the most depth, and others have studied how piece-wise isometries can allow for higher mode numbers in hyperbolic surfaces [1]. We note also that a recent study [172]

of radially curved ribbons concurs, at least qualitatively, with our experiments and simulations of confined rolled sheets in the limit of relatively small free length. Still, a more detailed investigation could be performed for each of these confined shells. Does the relationship between the free length and the size of the bending-dominated boundary layer affect shape-selection for confined cylinders and spherical segments, e.g. by setting the persistence length of circumferential bending?

In all cases, an important question we left unanswered is: How does the shell thickness affect the response to confinement? In the geometric range we studied, the wavenumber was unaffected by the thickness, but there almost certainly exist limits at which the evidently higher-order thickness dependence becomes relevant. Answering this question likely amounts to understanding the role of stretching, which could be studied in simulations [1], or possibly using experimental techniques like Digital Image Correlation (DIC). Understanding the stretching distribution could also resolve the contradiction we present in our scaling argument, i.e. that stretching is concentrated in a region near the clamp, but that we can approximate radial bending as being distributed over the free length. Other quantities that should be studied more closely are the mean and Gaussian curvature [52], and the elastic modulus.

Finally, we only studied the dynamic response to varied transverse confinement in experiments, and with negatively curved saddles. MD simulations, which handle contact well, could complement these experiments by providing information about stresses, strains, and the elastic energy distribution as the shell reconfigures. Due to unwanted contact, a similar study would likely be experimentally difficult for any of the other shells, besides perhaps rolled sheets with relatively low mean curvature. However, all confined geometries exhibit interesting shape-selection behaviors as the natural curvature increased due to residual swelling. We did not focus on these dynamics, and a closer look could make for an interest-

[1] Note that we performed FEM simulations for the three bilayer geometries for which residual swelling occurs through-the-thickness. This excludes the saddles that we built our scaling around, for which residual swelling occurs in-the-plane.

ing study related to confined differential growth. Further, as we saw in Chapter 5, a different curvature-inducing stimulus (e.g. a magnetic field applied to confined, magneto-responsive elastomer shells) could replace residual swelling to induce reversible reconfiguration. This could be relevant to, e.g., sea slug-like robotic locomotion [1].

6.1.2 Confined sheets

The work on the annular d-cone is ongoing, and we hope to improve upon the theoretical aspects of the work in Chapter 3. In particular, we believe we can: (1.) capture the small deflection state, including radial curvature which is not predicted in theoretical studies of the d-cone, (2.) perform a linear stability analysis about the small deflection state to predict the onset of wrinkling, and (3.) offer a complementary (and perhaps more straightforward) prediction for the opening angle based on the elastica. We also hope to understand (4.) when subsequent cones form, and (5.) how these dislocations are spatially distributed. Whereas confined saddles in Sect. 2 distribute waves evenly about the circumference, the annular d-cone can display small conical dislocations with opening angle $2\theta_c$ separated by angular distances greater than $2\theta_c$. This is particularly evident when the free length, and thus θ_c, is small. We leave systematic variation of the thickness and modulus in experiments to future work, and rely on simulations for this understanding.

Discrete, pre-folded analogs to the d-cone have emerged [164, 4, 163], which are informative from a geometric perspective. Related works, primarily aimed at studying the local mechanics of *kirigami*, add radial cuts to circular sheets [159]. These modifications free the packed sheet to either remain completely planar besides along folding ridges, or to accomodate excess length by simply overlapping. Similar approaches could be taken to study a discrete version of the annular d-cone. In particular, such *annular d-cone origami* or *kirigami* structures could offer intuition about the excess length during packing, perhaps helping to elucidate why subsequent cones form when they do.

6.1.3 Delayed buckling

We propose that our model in Chapter 4 can be extended to different loading methods and similar materials. However, we only verify our model for a single material and type of loading, and we study only relatively thick shells. Verifying the validity of our model over an extended parameter range would likely be worthwhile. The central concept, that creep deformation behaves like an evolving defect, applies in theory to shells of arbitrary geometry [71, 70]. Yet, the success of our model relies on (1.) Defect-like localization of creep deformation, which we ensured with our seeded geometric defect and (2.) An experiment-friendly understanding of how the knockdown factor depends on defect geometry [112]. Thus, slightly modified versions of our model could be tested on other geometries for which similar tools exist, e.g. an axially loaded cylindrical shell with a dimple defect [56].

Since the critical pressure decreases with time-dependent creep deformation, the energy barrier [91] to buckling lowers as well, and an increasingly small perturbation or probing force [56] can cause buckling. A future study could quantify this critical probing force, which likely depends on where it is applied, as creep progresses. This input force could be related to the energy released during buckling, with implications for tunable actuation. Various possible design routes for elastomer devices with tunable delays were discussed in the concluding remarks of Chapter 4.

6.1.4 Curvature-inducing stimuli

We demonstrated our key finding, that the optimal size of the active region for snapping spherical caps relates directly to the size of the boundary layer, using shells that respond to two different curvature-inducing stimuli. This affirmed that the non-mechanical stimulus is arbitrary, and that our results could be used to design actuators that respond to *e.g.* thermal, electrical, or chemical stimuli. As a general statement, the concept and the mathematical formulation of the curvature-inducing stimulus [147] is powerful, particularly for

simulations, and ought to be used more widely.

Appendix A

Differential geometry basics

The metric description of Koiter's elastic energy introduced in Chapter 1 offers a useful means to describe large deformations of arbitrary surfaces. Here, we introduce some of the basic concepts from differential geometry, primarly with illustrative examples. Einstein summation notation is assumed, i.e. we sum over indices that are repeated within a term, and the comma dentoes differentiation. As is relevant to shell and plate theories used and referenced within this thesis, we consider only 2D surfaces. Throughout this Appendix we follow Refs. [135] & [38].

A.1 First and second fundamental forms

Let $x^i = f^i(u^1, u^2)$ be a set of parametric equations (i.e. f^i are scalar functions) that define a coordinate transformation between Cartesian coordinates x^i, and a general (not necessarily Cartesian) 3D coordinate system u^i where u^3 is constant. The *first fundamental form* **a** contains all information about distances between points. It is defined as:

$$a_{\alpha\beta} = f^i_{,\alpha} f^i_{,\beta} \tag{A.1}$$

The *second fundamental form*, **b**, carries information about the curvatures, and is defined as:

$$b_{\alpha\beta} = N^i f^i_{,\alpha\beta} \tag{A.2}$$

where N^i is the normal unit vector, i.e. $N^i \equiv a^{-\frac{1}{2}} \varepsilon_{ijk} f^j_{,1} f^k_{,2}$ and $a \equiv \det(a_{\alpha\beta})$. Next, we provide a examples to illustrate how these quantities are computed for a flat sheet, a cylinder, and a sphere.

A.1.1 Flat plate

For a plane in Cartesian coordinates, $x^i = f^i(u^1, u^2) = f^i(x^1, x^2)$, and x^3 is constant. Thus,

$$(a_{\alpha\beta}) = \begin{pmatrix} f^i_{,1} f^i_{,1} & f^i_{,1} f^i_{,2} \\ f^i_{,2} f^i_{,1} & f^i_{,2} f^i_{,2} \end{pmatrix} = \begin{pmatrix} 1 & 0 \\ 0 & 1 \end{pmatrix}, \tag{A.3}$$

i.e the first fundamental form is the identity matrix for flat surfaces. The determinant $a = 1 \implies a^{-\frac{1}{2}} = 1$, so

$$N^i = \begin{pmatrix} 0 \\ 0 \\ 1 \end{pmatrix}, \tag{A.4}$$

thus

$$(b_{\alpha\beta}) = \begin{pmatrix} N^i f^i_{,11} & N^i f^i_{,12} \\ N^i f^i_{,21} & N^i f^i_{,22} \end{pmatrix} = \begin{pmatrix} 0 & 0 \\ 0 & 0 \end{pmatrix}, \tag{A.5}$$

which confirms that the curvatures are identically zero.

Consider also an alternative coordinate transformation applied to a flat plate, to cylindrical coordinates. Let initial coordinates $u^1 = r$ and $u^2 = \theta$ ($z\varepsilon$ constant). Then the Cartesian components x^i=$f^i(r, \theta)$ are:

$$(f^i) = \begin{pmatrix} r\cos\theta \\ r\sin\theta \\ z \end{pmatrix} \tag{A.6}$$

so the metric tensor for the flat plate in cylindrical coordinates is:

$$(a_{\alpha\beta}) = \begin{pmatrix} 1 & 0 \\ 0 & r^2 \end{pmatrix}, \tag{A.7}$$

and the normal vector is:

$$(N^i) = \begin{pmatrix} 0 \\ 0 \\ 1 \end{pmatrix}, \tag{A.8}$$

from which we find that the second fundamental form is, again,

$$(b_{\alpha\beta}) = \begin{pmatrix} 0 & 0 \\ 0 & 0 \end{pmatrix}. \tag{A.9}$$

A.1.2 Cylinder

We can represent a cylindrical shell by $x^i = f^i(\theta, z)$ where r is constant:

$$(f^i) = \begin{pmatrix} r\cos\theta \\ r\sin\theta \\ z \end{pmatrix}. \tag{A.10}$$

It follows that

$$(a_{\alpha\beta}) = \begin{pmatrix} 1 & 0 \\ 0 & r^2 \end{pmatrix}, \tag{A.11}$$

thus $a = r^2 \implies a^{-\frac{1}{2}} = \frac{1}{r}$, so

$$(N^i) = \begin{pmatrix} \cos\theta \\ \sin\theta \\ 0 \end{pmatrix}, \tag{A.12}$$

and therefore

$$(b_{\alpha\beta}) = \begin{pmatrix} 0 & 0 \\ 0 & r \end{pmatrix}. \tag{A.13}$$

Notice that the first fundamental forms of a flat sheet (Eq.(A.7)) and a cylinder (Eq. (A.7)) are identical. By definition, then, these two surfaces are *isometric* to one another. No stretching is required to roll a sheet into a cylinder, and vice-versa. Recalling the high energetic cost of stretching compared to bending explains why this is a preferred deformation for thin sheets.

A.1.3 Sphere

Let us parameterize a spherical shell according to $x^i = f^i(\phi,\theta)$ (ρ ε constant):

$$(f^i) = \begin{pmatrix} \rho\cos\phi \\ \rho\sin\phi\sin\theta \\ \rho\sin\phi\cos\theta \end{pmatrix}. \tag{A.14}$$

The first fundamental form is

$$(a_{\alpha\beta}) = \begin{pmatrix} \rho^2 & 0 \\ 0 & \rho^2\sin^2\phi \end{pmatrix}. \tag{A.15}$$

Then $a = \rho^4\sin^2\phi \implies a^{-\frac{1}{2}} = \frac{1}{\rho^2\sin\phi}$, and

$$(N^i) = \begin{pmatrix} -\cos\phi \\ -\sin\phi\sin\theta \\ -\sin\phi\cos\theta. \end{pmatrix} \tag{A.16}$$

The second fundamental form is:

$$(b_{\alpha\beta}) = \begin{pmatrix} \rho & 0 \\ 0 & \rho\sin^2\phi \end{pmatrix}. \tag{A.17}$$

A.2 Principal curvatures & invariants

The normal, or surface, curvature is defined as the ratio between the second and first fundamental forms. It is useful to know the extremal values and directions of this surface curvature. It can be shown that finding the extremal or *principal curvatures*, κ_n ($n \in \{1,2\}$) amounts to solving the following eigenvalue problem:

$$\det(b^\beta_\alpha - \kappa_n\delta^\beta_\alpha) = 0, \tag{A.18}$$

where δ^β_α is the Kroneker delta, and the raised index results from contraction with the contravariant form of the metric tensor, i.e. $b^\beta_\alpha = a^{\alpha\beta}b_{\alpha\beta}$. Roughly and practically speaking, $a^{\alpha\beta}$ is the matrix inverse of $\mathbf{a}$, so Eq. (A.18) can be thought of as $\mathbf{a}^{-1}\mathbf{b} - \kappa_n\mathbf{I}$ where $\mathbf{I}$ is

the identity matrix. The quantity b^{β}_{α} is sometimes called the *shape operator*. Thus, the eigenvectors of the shape operator give the directions in which the normal curvature is extremal, and the corresponding eigenvalues are the principal curvatures, κ_1 and κ_2.

The principal curvatures allow us to define the *mean curvature*, H:

$$H = \frac{\kappa_1 + \kappa_2}{2} = \frac{1}{2} b^{\alpha}_{\alpha}, \tag{A.19}$$

and the *Gaussian curvature*, K:

$$K = \kappa_1 \kappa_2 = |b^{\beta}_{\alpha}| = |b_{\alpha\gamma} a^{\gamma\beta}| = |b_{\alpha\gamma}||a^{\gamma\beta}| = \frac{b}{a} \tag{A.20}$$

where b is the determinant of the second fundamental form, and a is that of the first fundamental form. That is, the Gaussian curvature is the determinant of the shape operator, or equivalently, the product of the principal curvatures. The mean curvature is the trace of the shape operator, or their average. As H and K are functions of only invariants, they, too, are invariant under coordinate transformation.

We saw in Sect A.1 *via* direct comparison of the first fundamental forms that the cylinder is isometric to the plane. Notably, the principal curvature *does* change under deformation from a sheet to a cylinder. The fact that a slender structure can bend without stretching – which, as we have seen, is energetically preferable – is explained by Gauss's *Theorema Egregium*. The theorem, which is a main result of differential geometry, states that the Gaussian curvature of a surface is unchanged under isometry. Thus, the initially flat sheet avoids paying high stretching costs by bending in one principal direction while preserving zero curvature in the other, as the product of the two principal curvatures remains $K = 0$. Indeed, slender, bendy structures everywhere will agree with Gauss that this result is a "remarkable" and powerful one.

Bibliography

[1] A. Acharya and S. C. Venkataramani. Mechanics of moving defects in growing sheets: 3-d, small deformation theory. *Materials Theory*, 4(1), Apr. 2020.

[2] V. Alastrué, E. Peña, M. Á. Martínez, and M. Doblaré. Assessing the use of the "opening angle method" to enforce residual stresses in patient-specific arteries. *Annals of Biomedical Engineering*, 35(10):1821–1837, July 2007.

[3] M. B. Amar and Y. Pomeau. Crumpled paper. *Proceedings of the Royal Society of London. Series A: Mathematical, Physical and Engineering Sciences*, 453(1959):729–755, Apr. 1997.

[4] I. Andrade-Silva, M. Adda-Bedia, and M. A. Dias. Foldable cones as a framework for nonrigid origami. *Physical Review E*, 100(3), Sept. 2019.

[5] B. Audoly. *Elasticity and geometry : from hair curls to the non-linear response of shells*. Oxford University Press, Oxford New York, 2010.

[6] B. Audoly and J. W. Hutchinson. Localization in spherical shell buckling. *Journal of the Mechanics and Physics of Solids*, 136:103720, 2020. The Davide Bigoni 60th Anniversary Issue.

[7] J. B. Bard and J. Bard. *Morphogenesis: the cellular and molecular processes of developmental anatomy*, volume 23. Cambridge University Press, 1992.

[8] J. B. Bard and A. S. Ross. The morphogenesis of the ciliary body of the avian eye: I. lateral cell detachment facilitates epithelial folding. *Developmental Biology*, 92(1):73–86, 1982.

[9] J. B. Bard and A. S. Ross. The morphogenesis of the ciliary body of the avian eye: Ii. differential enlargement causes an epithelium to form radial folds. *Developmental Biology*, 92(1):87–96, 1982.

[10] W. Barros, E. N. de Azevedo, and M. Engelsberg. Surface pattern formation in a swelling gel. *Soft Matter*, 8(32):8511, 2012.

[11] Z. P. Bazant. *Stability of Structures: Elastic, inelastic, fracture, and damage theories*. WSPC, aug 2010.

[12] M. Ben Amar and M. Wu. Patterns in biofilms: From contour undulations to fold focussing. *EPL (Europhysics Letters)*, 108(3):38003–7, Nov. 2014.

[13] K. Bertoldi, V. Vitelli, J. Christensen, and M. van Hecke. Flexible mechanical metamaterials. *Nature Reviews*, 2:17066, 2017.

[14] D. L. Blair and A. Kudrolli. Geometry of crumpled paper. *Physical Review Letters*, 94(16), Apr. 2005.

[15] G. Boedec and J. Deschamps. Disk wrinkling under gravity. *arXiv preprint arXiv:2012.00537*, 2020.

[16] J. W. Boley, W. M. van Rees, C. Lissandrello, M. N. Horenstein, R. L. Truby, A. Kotikian, J. A. Lewis, and L. Mahadevan. Shape-shifting structured lattices via multimaterial 4d printing. *Proceedings of the National Academy of Sciences*, 116(42):20856–20862, Oct. 2019.

[17] A. Brinkmeyer, M. Santer, A. Pirrera, and P. Weaver. Pseudo-bistable self-actuated domes for morphing applications. *International Journal of Solids and Structures*, 49(9):1077 – 1087, 2012.

[18] D. Bushnell. Nonlinear axisymmetric behavior of shells of revolution. *AIAA Journal*, 5(3):432–439, Mar. 1967.

[19] G. Castori, A. Borri, and M. Corradi. Behavior of thin masonry arches repaired using composite materials. *Composites Part B: Engineering*, 87:311–321, Feb. 2016.

[20] E. Cerda. Mechanics of scars. *Journal of Biomechanics*, 38(8):1598–1603, 2005.

[21] E. Cerda, S. Chaieb, F. Melo, and L. Mahadevan. Conical dislocations in crumpling. *Nature*, 401(6748):46–49, 1999.

[22] E. Cerda and L. Mahadevan. Conical surfaces and crescent singularities in crumpled sheets. *Physical Review Letters*, 80(11):2358, 1998.

[23] E. Cerda and L. Mahadevan. Geometry and physics of wrinkling. *Physical Review Letters*, 90(7), Feb. 2003.

[24] E. Cerda and L. Mahadevan. Confined developable elastic surfaces: cylinders, cones and the elastica. *Proceedings of the Royal Society A: Mathematical, Physical and Engineering Sciences*, 461(2055):671–700, Mar. 2005.

[25] E. Cerda, L. Mahadevan, and J. M. Pasini. The elements of draping. *Proceedings of the National Academy of Sciences*, 101(7):1806–1810, Feb. 2004.

[26] S. Chaieb. From creases to conical deflections in a buckled thin sheet: stress focusing vs singularities in strong deformations of a thin elastic sheet. *Journal of the Mechanics and Physics of Solids*, 48:565–579, 2000.

[27] S. Chaïeb, F. Melo, and J.-C. Géminard. Experimental study of developable cones. *Physical Review Letters*, 80(11):2354, 1998.

[28] S. Chaïeb and F. Melo. Crescent singularities and stress focusing in a buckled thin sheet: Mechanics of developable cones. *Physical Review E*, 60(5):6091–6103, Nov. 1999.

[29] K. Che, M. Rouleau, and J. Meaud. Temperature-tunable time-dependent snapping of viscoelastic metastructures with snap-through instabilities. *Extreme Mechanics Letters*, 32:100528, 2019.

[30] K. Che, C. Yuan, H. J. Qi, and J. Meaud. Viscoelastic multistable architected materials with temperature-dependent snapping sequence. *Soft Matter*, 14:2492–2499, 2018.

[31] D. Chen, J. Yoon, D. Chandra, A. J. Crosby, and R. C. Hayward. Stimuli-responsive buckling mechanics of polymer films. *Journal of Polymer Science Part B: Polymer Physics*, 52(22):1441–1461, Sept. 2014.

[32] J. Y. Chung, A. Vaziri, and L. Mahadevan. Reprogrammable braille on an elastic shell. *Proceedings of the National Academy of Sciences*, 115(29):7509–7514, July 2018.

[33] G. Coupier, A. Djellouli, and C. Quilliet. Let's deflate that beach ball. *The European Physical Journal E*, 42(9), Sept. 2019.

[34] J. Dervaux and M. B. Amar. Mechanical Instabilities of Gels. *Annual Review of Condensed Matter Physics*, 3(1):311–332, Mar. 2012.

[35] J. Dervaux and M. Ben Amar. Buckling Condensation in Constrained Growth. *Journal of the Mechanics and Physics of Solids*, 59(3):538–560, Mar. 2011.

[36] J. Dervaux, Y. Couder, M.-A. Guedeau-Boudeville, and M. B. Amar. Shape transition in artificial tumors: from smooth buckles to singular creases. *Physical Review Letters*, 107(1):018103, 2011.

[37] J. Dervaux, J. C. Magniez, and A. Libchaber. On growth and form of Bacillus subtilis biofilms. *Interface Focus*, 4(6):20130051–20130051, Oct. 2014.

[38] M. Deserno. Notes on Differential Geometry, 2004. url: `https://www.cmu.edu/biolphys/deserno/pdf/diff_geom.pdf`. Last visited on 2021/03/19.

[39] M. A. Dias, J. A. Hanna, and C. D. Santangelo. Programmed buckling by controlled lateral swelling in a thin elastic sheet. *Physical Review E*, 84(3):036603, 2011.

[40] D. A. Dillard, B. Mukherjee, P. Karnal, R. C. Batra, and J. Frechette. A review of winkler's foundation and its profound influence on adhesion and soft matter applications. *Soft Matter*, 14(19):3669–3683, 2018.

[41] A. Djellouli, P. Marmottant, H. Djeridi, C. Quilliet, and G. Coupier. Buckling instability causes inertial thrust for spherical swimmers at all scales. *Physical Review Letters*, 119:224501, Nov 2017.

[42] P. Domokos, G; Holmes and B. Royce. Constrained Euler Buckling. *Journal of Nonlinear Science*, 7:281–314, 1997.

[43] S. J. DuPont, Jr, R. S. Cates, P. G. Stroot, and R. Toomey. Swelling-induced instabilities in microscale, surface-confined poly(N-isopropylacryamide) hydrogels. *Soft Matter*, 6(16):3876, 2010.

[44] D. M. J. Dykstra, J. Busink, B. Ennis, and C. Coulais. Viscoelastic snapping metamaterials. *Journal of Applied Mechanics*, 86(11), 09 2019.

[45] E. Efrati, E. Sharon, and R. Kupferman. Buckling transition and boundary layer in non-euclidean plates. *Physical Review E*, 80(1), July 2009.

[46] E. Efrati, E. Sharon, and R. Kupferman. Elastic theory of unconstrained non-euclidean plates. *Journal of the Mechanics and Physics of Solids*, 57(4):762–775, 2009.

[47] S. Farmer and C. Calladine. Geometry of "developable cones". *International Journal of Mechanical Sciences*, 47(4-5):509–520, Apr. 2005.

[48] C. Fei, S. Mao, J. Yan, R. Alert, H. A. Stone, B. L. Bassler, N. S. Wingreen, and A. Košmrlj. Nonuniform growth and surface friction determine bacterial biofilm morphology on soft substrates. *Proceedings of the National Academy of Sciences*, 117(14):7622–7632, Mar. 2020.

[49] B. Florijn, C. Coulais, and M. van Hecke. Programmable mechanical metamaterials. *Physical Review Letters*, 113(17), Oct. 2014.

[50] Y. Forterre, J. M. Skotheim, J. Dumais, and L. Mahadevan. How the venus flytrap snaps. *Nature*, 433(7024):421–425, Jan. 2005.

[51] Y. C. Fung and W. H. Wittrick. A boundary layer phenomenon in the large deflexion of thin plates. *The Quarterly Journal of Mechanics and Applied Mathematics*, 8(2):191–210, 1955.

[52] J. Gemmer and S. C. Venkataramani. Shape transitions in hyperbolic non-euclidean plates. *Soft Matter*, 9(34):8151, 2013.

[53] G. Gerard. A creep buckling hypothesis. *Journal of the Aeronautical Sciences*, 23(9):879–882, Sept. 1956.

[54] G. Gerard and A. C. Gilbert. A critical strain approach to creep buckling of plates and shells. *Journal of the Aerospace Sciences*, 25(7):429–434, July 1958.

[55] S. Gerasimidis and J. W. Hutchinson. Dent imperfections in shell buckling: The role of geometry, residual stress, and plasticity. *Journal of Applied Mechanics*, 88(3), Dec. 2020.

[56] S. Gerasimidis, E. Virot, J. W. Hutchinson, and S. M. Rubinstein. On establishing buckling knockdowns for imperfection-sensitive shell structures. *Journal of Applied Mechanics*, 85(9), June 2018.

[57] M. Gomez, D. Moulton, and D. Vella. Dynamics of viscoelastic snap-through. *Journal of the Mechanics and Physics of Solids*, 124:781–813, 2018.

[58] M. Gomez, D. E. Moulton, and D. Vella. Critical slowing down in purely elastic 'snap-through' instabilities. *Nature Physics*, 13(2):142–145, Oct. 2016.

[59] M. Gomez, D. E. Moulton, and D. Vella. Passive control of viscous flow via elastic snap-through. *Physical Review Letters*, 119(14), Oct. 2017.

[60] A. Goriely. *The Mathematics and Mechanics of Biological Growth*. Springer, May 2017.

[61] A. Goriely, M. G. D. Geers, G. A. Holzapfel, J. Jayamohan, A. Jérusalem, S. Sivaloganathan, W. Squier, J. A. W. van Dommelen, S. Waters, and E. Kuhl. Mechanics of the brain: perspectives, challenges, and opportunities. *Biomechanics and Modeling in Mechanobiology*, 14(5):931–965, Feb. 2015.

[62] B. Gorissen, D. Melancon, N. Vasios, M. Torbati, and K. Bertoldi. Inflatable soft jumper inspired by shell snapping. *Science Robotics*, 5(42), 2020.

[63] B. Gorissen, D. Reynaerts, S. Konishi, K. Yoshida, J.-W. Kim, and M. D. Volder. Elastic inflatable actuators for soft robotic applications. *Advanced Materials*, 29(43):1604977, Sept. 2017.

[64] T. Guo, X. Zheng, and P. Palffy-Muhoray. Measuring the lift-off force for d cones. In *APS Meeting Abstracts*, 2021. E16.00007.

[65] F. Haas and R. J. Wootton. Two basic mechanisms in insect wing folding. *Proceedings of the Royal Society of London. Series B: Biological Sciences*, 263(1377):1651–1658, Dec. 1996.

[66] P. A. Haas and R. E. Goldstein. Elasticity and glocality: initiation of embryonic inversion in volvox. *Journal of The Royal Society Interface*, 12(112):20150671, Nov. 2015.

[67] P. A. Haas and R. E. Goldstein. Embryonic inversion in volvox carteri: The flipping and peeling of elastic lips. *Physical Review E*, 98:052415, Nov 2018.

[68] S. Han and R. K. Mallampalli. The role of surfactant in lung disease and host defense against pulmonary infections. *Annals of the American Thoracic Society*, 12(5):765–774, May 2015.

[69] B. J. Hansen, C. J. Carron, B. D. Jensen, A. R. Hawkins, and S. M. Schultz. Plastic latching accelerometer based on bistable compliant mechanisms. *Smart Materials and Structures*, 16(5):1967–1972, Sept. 2007.

[70] B. Hayman. Aspects of creep buckling. i. the influence of post-buckling characteristics. *Proceedings of the Royal Society A: Mathematical, Physical and Engineering Sciences*, 364(1718):393–414, Dec. 1978.

[71] B. Hayman. Creep buckling — a general view of the phenomena. In *Creep in Structures*, pages 289–307. Springer Berlin Heidelberg, 1981.

[72] M. Heil, A. L. Hazel, and J. A. Smith. The mechanics of airway closure. *Respiratory Physiology & Neurobiology*, 163(1-3):214–221, Nov. 2008.

[73] N. J. Hoff. Forty-first wilbur wright memorial lecture: Buckling and stability. *The Journal of the Royal Aeronautical Society*, 58(517):3–52, 1954.

[74] N. J. Hoff. Creep buckling. *Aeronautical Quarterly*, 7(1):1–20, Feb. 1956.

[75] N. J. Hoff. Creep buckling of plates and shells. In *Theoretical and Applied Mechanics*, pages 124–140. Springer Berlin Heidelberg, 1973.

[76] N. J. Hoff. The effect of geometric nonlinearities on the creep buckling time of axially compressed circular cylindrical shells. *Journal of Applied Mechanics*, 42(1):225–226, Mar. 1975.

[77] S. Höhn, A. R. Honerkamp-Smith, P. A. Haas, P. K. Trong, and R. E. Goldstein. Dynamics of a Volvox Embryo Turning Itself Inside Out. *Physical Review Letters*, 114(17):178101, Apr. 2015.

[78] D. P. Holmes. Elasticity and stability of shape-shifting structures. *Current Opinion in Colloid & Interface Science*, 40:118–137, Apr. 2019.

[79] D. P. Holmes and A. J. Crosby. Snapping surfaces. *Advanced Materials*, 19(21):3589–3593, Nov. 2007.

[80] D. P. Holmes, J.-H. Lee, H. S. Park, and M. Pezzulla. Nonlinear buckling behavior of a complete spherical shell under uniform external pressure and homogenous natural curvature. *Physical Review E*, 102(2), Aug. 2020.

[81] D. P. Holmes, M. Roché, T. Sinha, and H. Stone. Bending and twisting of soft materials by non-homogenous swelling. *Soft Matter*, 7(11):5188, 2011.

[82] D. P. Holmes, B. Tavakol, G. Froehlicher, and H. A. Stone. Control and manipulation of microfluidic flow via elastic deformations. *Soft Matter*, 9(29):7049–7053, May 2013.

[83] P. Holmes, G. Domokos, J. Schmitt, and I. Szeberényi. Constrained Euler buckling: an interplay of computation and analysis. *Computer Methods in Applied Mechanics and Engineering*, 170(3-4):175–207, Mar. 1999.

[84] N. C. Huang. Axisymmetrical creep buckling of clamped shallow spherical shells. *Journal of Applied Mechanics*, 32(2):323–330, June 1965.

[85] N. C. Huang. Nonlinear creep buckling of some simple structures. *Journal of Applied Mechanics*, 34(3):651–658, Sept. 1967.

[86] J. Hure, B. Roman, and J. Bico. Stamping and wrinkling of elastic plates. *Physical Review Letters*, 109(5), Aug. 2012.

[87] J. W. Hutchinson. Imperfection sensitivity of externally pressurized spherical shells. *Journal of Applied Mechanics*, 34(1):49–55, Mar. 1967.

[88] J. W. Hutchinson. Buckling of spherical shells revisited. *Proceedings of the Royal Society A: Mathematical, Physical and Engineering Sciences*, 472(2195):20160577, Nov. 2016.

[89] J. W. Hutchinson. EML webinar overview: New developments in shell stability. *Extreme Mechanics Letters*, 39:100805, Sept. 2020.

[90] J. W. Hutchinson and J. M. T. Thompson. Nonlinear buckling behaviour of spherical shells: barriers and symmetry-breaking dimples. *Philosophical Transactions of the Royal Society A: Mathematical, Physical and Engineering Sciences*, 375(2093):20160154, Apr. 2017.

[91] J. W. Hutchinson and J. M. T. Thompson. Imperfections and energy barriers in shell buckling. *International Journal of Solids and Structures*, 148-149:157–168, Sept. 2018.

[92] M. Jakomin, F. Kosel, and T. Kosel. Thin double curved shallow bimetallic shell of translation in a homogenous temperature field by non-linear theory. *Thin-Walled Structures*, 48(3):243–259, Mar. 2010.

[93] S. D. Janssens, B. Sutisna, A. Giussani, J. A. Kwiecinski, D. Vázquez-Cortés, and E. Fried. Boundary curvature effect on the wrinkling of thin suspended films. *Applied Physics Letters*, 116(19):193702, May 2020.

[94] X. Jiang, M. Pezzulla, H. Shao, T. K. Ghosh, and D. P. Holmes. Snapping of bistable, prestressed cylindrical shells. *EPL (Europhysics Letters)*, 122(6):64003, 2018.

[95] F. L. Jiménez, J. Marthelot, A. Lee, J. W. Hutchinson, and P. M. Reis. Technical brief: Knockdown factor for the buckling of spherical shells containing large-amplitude geometric defects. *Journal of Applied Mechanics*, 84(3):034501, Jan. 2017.

[96] N. Jones. Creep buckling of a complete spherical shell. *Journal of Applied Mechanics*, 43(3):450–454, Sept. 1976.

[97] A. Kaplan and Y. Fung. A nonlinear theory of bending and buckling of thin elastic shallow spherical shells. 1954. NACA-TN-3212.

[98] T. V. Karman and H.-S. Tsien. The buckling of spherical shells by external pressure. *Journal of the Aeronautical Sciences*, 7(2):43–50, Dec. 1939.

[99] C. Keplinger, T. Li, R. Baumgartner, Z. Suo, and S. Bauer. Harnessing snap-through instability in soft dielectrics to achieve giant voltage-triggered deformation. *Soft Matter*, 8(2):285–288, 2012.

[100] A. D. Kerr. Analysis of thermal track buckling in the lateral plane. *Acta Mechanica*, 30(1-2):17–50, Mar. 1978.

[101] J. Kim, J. A. Hanna, M. Byun, C. D. Santangelo, and R. C. Hayward. Designing responsive buckled surfaces by halftone gel lithography. *Science*, 335(6073):1201–1205, Mar. 2012.

[102] Y. Klein, E. Efrati, and E. Sharon. Shaping of elastic sheets by prescription of non-euclidean metrics. *Science*, 315(5815):1116–1120, Feb. 2007.

[103] T. Koga and N. J. Hoff. The axisymmetric buckling of initially imperfect complete spherical shells. *International Journal of Solids and Structures*, 5(7):679–697, July 1969.

[104] W. T. Koiter. *Over de stabiliteit van het elastisch evenwicht*. PhD thesis, Delft University of Technology, 1945.

[105] W. T. Koiter. On the nonlinear theory of thin elastic shells. *Proceedings of the Koninklijke Nederlandse Akademie van Wetenschappen*, B79:1–54, 1966.

[106] W. T. Koiter and J. G. Simmonds. Foundations of shell theory. In *Theoretical and applied mechanics*, pages 150–176. Springer, 1973.

[107] M. Krenzke and T. Kiernan. The effect of initial imperfections on the collapse strength of deep spherical shells. 1965. DTMB Report 1757.

[108] R. S. Lakes. *Viscoelastic materials*. Cambridge University Press, Cambridge; New York, 2009.

[109] L. D. Landau. *Theory of elasticity*. Butterworth-Heinemann, Oxford England Burlington, MA, 1986.

[110] F. A. Leckie and B. Hayman. Creep instability of thick shell structures. In *Buckling of Structures*, pages 86–94. Springer Berlin Heidelberg, 1976.

[111] A. Lee, P. T. Brun, J. Marthelot, G. Balestra, F. Gallaire, and P. M. Reis. Fabrication of slender elastic shells by the coating of curved surfaces. *Nature Communications*, 7(1), Apr. 2016.

[112] A. Lee, F. L. Jiménez, J. Marthelot, J. W. Hutchinson, and P. M. Reis. The geometric role of precisely engineered imperfections on the critical buckling load of spherical elastic shells. *Journal of Applied Mechanics*, 83(11):111005, Sept. 2016.

[113] A. Lee, D. Yan, M. Pezzulla, D. P. Holmes, and P. M. Reis. Evolution of critical buckling conditions in imperfect bilayer shells through residual swelling. *Soft Matter*, 15(30):6134–6144, 2019.

[114] J.-H. Lee, H. S. Park, and D. P. Holmes. Elastic instabilities govern the morphogenesis of the optic cup. *Forthcoming*, 2021.

[115] M. M. Lee and S. Chien. Morphologic effects of pressure changes on canine carotid artery endothelium as observed by scanning electron microscopy. *The Anatomical Record*, 194(1):1–14, 1979.

[116] H. Liang and L. Mahadevan. The shape of a long leaf. *Proceedings of the National Academy of Sciences*, 106(52):22049–22054, Dec. 2009.

[117] T. Liang and T. A. Witten. Crescent singularities in crumpled sheets. *Physical Review E*, 71(1), Jan. 2005.

[118] I.-K. Lin, K.-S. Ou, Y.-M. Liao, Y. Liu, K.-S. Chen, and X. Zhang. Viscoelastic characterization and modeling of polymer transducers for biological applications. *Journal of Microelectromechanical Systems*, 18(5):1087–1099, Oct. 2009.

[119] Z. Liu, W. Hong, Z. Suo, S. Swaddiwudhipong, and Y. Zhang. Modeling and simulation of buckling of polymeric membrane thin film gel. *Computational Materials Science*, 49(1, Supplement):S60 – S64, 2010. Symposium Q: Computational Materials Design at All Scales: From Theory to Application.

[120] A. Love. XVI. the small free vibrations and deformation of a thin elastic shell. *Philosophical Transactions of the Royal Society of London. (A.)*, 179:491–546, Dec. 1888.

[121] T. Lu, C. Ma, and T. Wang. Mechanics of dielectric elastomer structures: A review. *Extreme Mechanics Letters*, 38:100752, July 2020.

[122] X. Lu, J. Zhao, and H. Gregersen. Small intestinal morphometric and biomechanical changes during physiological growth in rats. *Journal of Biomechanics*, 38(3):417–426, 2005.

[123] A. Lucantonio, P. Nardinocchi, and M. Pezzulla. Swelling-induced and controlled curving in layered gel beams. *Proceedings of the Royal Society of London A: Mathematical, Physical and Engineering Sciences*, 470(2171):20140467–20140467, Nov. 2014.

[124] L. Mahadevan, A. Vaziri, and M. Das. Persistence of a pinch in a pipe. *EPL (Europhysics Letters)*, 77(4):40003, Feb. 2007.

[125] J. Marthelot, P.-T. Brun, F. Lopez Jimenez, and P. M. Reis. Periodic buckling of constrained cylindrical elastic shells. In *APS Meeting Abstracts*, page C15.010, 2017.

[126] McMillen and Goriely. Tendril perversion in intrinsically curved rods. *Journal of Nonlinear Science*, 12(3):241–281, July 2002.

[127] T. Minahen and W. Knauss. Creep buckling of viscoelastic structures. *International Journal of Solids and Structures*, 30:1075–1092, 02 1993.

[128] N. Miyazaki and S. Hagihara. Creep buckling of shell structures. *Mechanical Engineering Reviews*, 2(2):14–00522–14–00522, 2015.

[129] N. Miyazaki, G. Yagawa, and Y. Ando. A parametric analysis of creep buckling of a shallow spherical shell by the finite element method. *Nuclear Engineering and Design*, 41(2):257–263, Apr. 1977.

[130] M. Mokbel, A. Djellouli, C. Quilliet, S. Aland, and G. Coupier. Post-buckling dynamics of spherical shells. Forthcoming, 2021.

[131] T. Mora and A. Boudaoud. Buckling of swelling gels. *The European Physical Journal E*, 20(2):119–124, June 2006.

[132] A. J. Mowitz. Finite curved creases in infinite isometric sheets. *arXiv preprint arXiv:2012.04834*, 2020.

[133] NASA. Buckling of thin-walled doubly-curved shells. NASA space vehicle design criteria (structures), Aug. 1969. NASA SP-8032.

[134] A. Nasto, A. Ajdari, A. Lazarus, A. Vaziri, and P. M. Reis. Localization of deformation in thin shells under indentation. *Soft Matter*, 9(29):6796–9, 2013.

[135] F. Niordson. *Shell theory*. North-Holland Sole distributors for the U.S.A. and Canada, Elsevier Science Pub. Co, Amsterdam New York New York, N.Y, 1985.

[136] H. Obrecht. Creep buckling and postbuckling of circular cylindrical shells under axial compression. *International Journal of Solids and Structures*, 13(4):337–355, 1977.

[137] A. O'Halloran, F. O'Malley, and P. McHugh. A review on dielectric elastomer actuators, technology, applications, and challenges. *Journal of Applied Physics*, 104(7):071101, 2008.

[138] B. O'Neill. *Elementary differential geometry*. Elsevier Academic Press, Amsterdam; Boston, rev. 2nd edition, 2006.

[139] J. T. B. Overvelde, T. Kloek, J. J. A. D'haen, and K. Bertoldi. Amplifying the response of soft actuators by harnessing snap-through instabilities. *Proceedings of the National Academy of Sciences*, 112(35):10863–10868, Aug. 2015.

[140] A. Pandey and D. P. Holmes. Swelling-induced deformations: a materials-defined transition from macroscale to microscale deformations. *Soft Matter*, 9(23):5524, 2013.

[141] A. Pandey, D. E. Moulton, D. Vella, and D. P. Holmes. Dynamics of snapping beams and jumping poppers. *EPL (Europhysics Letters)*, 105(2):24001, Jan. 2014.

[142] J. Paulose and D. R. Nelson. Buckling pathways in spherical shells with soft spots. *Soft Matter*, 9(34):8227, 2013.

[143] J. D. Paulsen. Wrapping liquids, solids, and gases in thin sheets. *arXiv preprint arXiv:1804.07425*, 2018.

[144] J. D. Paulsen, V. Démery, C. D. Santangelo, T. P. Russell, B. Davidovitch, and N. Menon. Optimal wrapping of liquid droplets with ultrathin sheets. *Nature Materials*, 14(12):1206, 2015.

[145] M. Pezzulla, S. A. Shillig, P. Nardinocchi, and D. P. Holmes. Morphing of geometric composites via residual swelling. *Soft Matter*, 11(29):5812–5820, 2015.

[146] M. Pezzulla, G. P. Smith, P. Nardinocchi, and D. P. Holmes. Geometry and mechanics of thin growing bilayers. *Soft Matter*, 12:4435–4442, May 2016.

[147] M. Pezzulla, N. Stoop, X. Jiang, and D. P. Holmes. Curvature-driven morphing of non-euclidean shells. *Proceedings of the Royal Society A: Mathematical, Physical and Engineering Sciences*, 473(2201):20170087, May 2017.

[148] M. Pezzulla, N. Stoop, M. P. Steranka, A. J. Bade, and D. P. Holmes. Curvature-induced instabilities of shells. *Physical Review Letters*, 120:048002, Jan 2018.

[149] A. Pocheau and B. Roman. Uniqueness of solutions for constrained Elastica. *Physica D: Nonlinear Phenomena*, 192(3-4):161–186, June 2004.

[150] A. Poulin, S. Rosset, and H. R. Shea. Printing low-voltage dielectric elastomer actuators. *Applied Physics Letters*, 107(24):244104, Dec. 2015.

[151] P. K. Purohit, J. Kondev, and R. Phillips. Mechanics of DNA packaging in viruses. *Proceedings of the National Academy of Sciences*, 100(6):3173–3178, Mar. 2003.

[152] C. Quilliet. Numerical deflation of beach balls with various poisson's ratios: From sphere to bowl's shape. *The European Physical Journal E*, 35(6), June 2012.

[153] P. M. Reis. A perspective on the revival of structural (in)stability with novel opportunities for function: From buckliphobia to buckliphilia. *Journal of Applied Mechanics*, 82(11), Sept. 2015.

[154] P. M. Reis, H. M. Jaeger, and M. Van Hecke. Designer matter: A perspective. *Extreme Mechanics Letters*, 5:25–29, 2015.

[155] B. Roman and A. Pocheau. Buckling cascade of thin plates: Forms, constraints and similarity. *EPL (Europhysics Letters)*, 46(5):602–608, June 1999.

[156] B. Roman and A. Pocheau. Postbuckling of bilaterally constrained rectangular thin plates. *Journal of the Mechanics and Physics of Solids*, 50(11):2379–2401, Nov. 2002.

[157] D. Rosenthal and H. Baer. An elementary theory of creep buckling of columns. In *Journal of Applied Mechanics-Transactions of the ASME*, volume 18, pages 321–321. ASME, 1951.

[158] S. Sacanna, W. T. M. Irvine, P. M. Chaikin, and D. J. Pine. Lock and key colloids. *Nature*, 464(7288):575–578, Mar. 2010.

[159] S. Sadik and M. A. Dias. On local kirigami mechanics i: Isometric conical solutions. *Journal of the Mechanics and Physics of Solids*, 151:104370, June 2021.

[160] J. L. Sanders. Nonlinear theories for thin shells. *Quarterly of Applied Mathematics*, 21(1):21–36, Apr. 1963.

[161] M. Santer. Self-actuated snap back of viscoelastic pulsing structures. *International Journal of Solids and Structures*, 47(24):3263 – 3271, 2010.

[162] R. D. Schroll, E. Katifori, and B. Davidovitch. Elastic building blocks for confined sheets. *Physical Review Letters*, 106(7), Feb. 2011.

[163] K. A. Seffen. Fundamental conical defects: The d-cone, its e-cone, and its p-cone. *Physical Review E*, 94(1), July 2016.

[164] K. A. Seffen. Spherical images and inextensible curved folding. *Physical Review E*, 97(2), Feb. 2018.

[165] H. Shao, S. Wei, X. Jiang, D. P. Holmes, and T. K. Ghosh. Bioinspired electrically activated soft bistable actuators. *Advanced Functional Materials*, 28(35):1802999, 2018.

[166] E. Sharon and E. Efrati. The mechanics of non-euclidean plates. *Soft Matter*, 6(22):5693, 2010.

[167] E. Sharon, B. Roman, M. Marder, G.-S. Shin, and H. L. Swinney. Buckling cascades in free sheets. *Nature*, 419(6907):579–579, Oct. 2002.

[168] E. Sharon, B. Roman, and H. L. Swinney. Geometrically driven wrinkling observed in free plastic sheets and leaves. *Physical Review E*, 75(4), Apr. 2007.

[169] J. J. J. Shi, C. D. Johnson, and N. R. Bauld. Application of the variational theorem for creep of shallow spherical shells. *AIAA Journal*, 8(3):469–476, Mar. 1970.

[170] J. Shim, C. Perdigou, E. R. Chen, K. Bertoldi, and P. M. Reis. Buckling-induced encapsulation of structured elastic shells under pressure. *Proceedings of the National Academy of Sciences*, 109(16):5978–5983, Mar. 2012.

[171] J. Sieber, J. W. Hutchinson, and J. M. T. Thompson. Nonlinear dynamics of spherical shells buckling under step pressure. *Proceedings of the Royal Society A: Mathematical, Physical and Engineering Sciences*, 475(2223):20180884, Mar. 2019.

[172] E. Siéfert, I. Levin, and E. Sharon. Euclidean frustrated ribbons. *arXiv preprint arXiv:2102.07194*, 2021.

[173] M. Smith, G. Yanega, and A. Ruina. Elastic instability model of rapid beak closure in hummingbirds. *Journal of Theoretical Biology*, 282(1):41–51, Aug. 2011.

[174] K. Son, J. S. Guasto, and R. Stocker. Bacteria can exploit a flagellar buckling instability to change direction. *Nature Physics*, 9(8):494–498, July 2013.

[175] J. Y. Song, S. Heo, and J. Shim. Snapping facades: Exploring elastic instability for the building envelope. *Technology Architecture + Design*, 2(1):45–54, Jan. 2018.

[176] L. Stein-Montalvo, P. Costa, M. Pezzulla, and D. P. Holmes. Buckling of geometrically confined shells. *Soft Matter*, 15(6):1215–1222, 2019.

[177] W. J. Stronge, M. P. F. Sutcliffe, and T. X. Yu. Wrinkling of elastoplastic circular plates during stamping. *Experimental Mechanics*, 26(4):345–353, Dec. 1986.

[178] M. Taffetani, X. Jiang, D. P. Holmes, and D. Vella. Static bistability of spherical caps. *Proceedings of the Royal Society A: Mathematical, Physical and Engineering Sciences*, 474(2213):20170910, May 2018.

[179] D. Terwagne, M. Brojan, and P. M. Reis. Smart morphable surfaces for aerodynamic drag control. *Advanced Materials*, 26(38):6608–6611, June 2014.

[180] S. Tibbits. 4d printing: Multi-material shape change. *Architectural Design*, 84(1):116–121, Jan. 2014.

[181] S. Timoshenko. Analysis of bi-metal thermostats. *Journal of the Optical Society of America*, 11(3):233–255, Sep 1925.

[182] H.-S. Tsien. A theory for the buckling of thin shells. *Journal of the Aeronautical Sciences*, 9(10):373–384, Aug. 1942.

[183] E. Y. Urbach and E. Efrati. The metric description of viscoelasticity and instabilities in viscoelastic solids. *arXiv preprint arXiv:1806.01237*, 2018.

[184] E. Y. Urbach and E. Efrati. Predicting delayed instabilities in viscoelastic solids. *Science Advances*, 6(36):eabb2948, Sept. 2020.

[185] W. M. van Rees, E. Vouga, and L. Mahadevan. Growth patterns for shape-shifting elastic bilayers. *Proceedings of the National Academy of Sciences*, page 201709025, 2017.

[186] H. Vandeparre, M. Piñeirua, F. Brau, B. Roman, J. Bico, C. Gay, W. Bao, C. N. Lau, P. M. Reis, and P. Damman. Wrinkling hierarchy in constrained thin sheets from suspended graphene to curtains. *Physical Review Letters*, 106(22), June 2011.

[187] A. Vaziri and L. Mahadevan. Localized and extended deformations of elastic shells. *Proceedings of the National Academy of Sciences*, 105(23):7913–7918, 2008.

[188] D. Vella. Buffering by buckling as a route for elastic deformation. *Nature Reviews Physics*, 1(7):425–436, May 2019.

[189] D. Vella and B. Davidovitch. Regimes of wrinkling in an indented floating elastic sheet. *arXiv preprint arXiv:1804.03341*, 2018.

[190] H. Wagner, C. Hühne, J. Zhang, and W. Tang. On the imperfection sensitivity and design of spherical domes under external pressure. *International Journal of Pressure Vessels and Piping*, 179:104015, Jan. 2020.

[191] G. Wan, Y. Cai, Y. Liu, C. Jin, D. Wang, S. Huang, N. Hu, J. X. Zhang, and Z. Chen. Bistability in popper-like shells programmed by geometric defects. *Extreme Mechanics Letters*, 42:101065, Jan. 2021.

[192] F. M. Weiss, T. Töpper, B. Osmani, S. Peters, G. Kovacs, and B. Müller. Electrospraying nanometer-thin elastomer films for low-voltage dielectric actuators. *Advanced Electronic Materials*, 2(5):1500476, Feb. 2016.

[193] B. R. Wiggs, C. A. Hrousis, J. M. Drazen, and R. D. Kamm. On the mechanism of mucosal folding in normal and asthmatic airways. *Journal of Applied Physiology*, 83(6):1814–1821, Dec. 1997.

[194] T. A. Witten. Stress focusing in elastic sheets. *Reviews of Modern Physics*, 79(2):643–675, Apr. 2007.

[195] Z. L. Wu, M. Moshe, J. Greener, H. Therien-Aubin, Z. Nie, E. Sharon, and E. Kumacheva. Three-dimensional shape transformations of hydrogel sheets induced by small-scale modulation of internal stresses. *Nature Communications*, 4:1586–7, 2013.

[196] P. Xirouchakis and N. Jones. Axisymmetric and bifurcation creep buckling of externally pressurised spherical shells. *International Journal of Solids and Structures*, 16(2):131–148, 1980.

[197] F. Xu, C. Fu, and Y. Yang. Water affects morphogenesis of growing aquatic plant leaves. *Physical Review Letters*, 124(3), Jan. 2020.

[198] D. Yan, M. Pezzulla, L. Cruveiller, A. Abbasi, and P. M. Reis. Magneto-active elastic shells with tunable buckling strength. *arXiv preprint arXiv:2012.01163*, 2020.

[199] D. Yan, M. Pezzulla, and P. M. Reis. Buckling of pressurized spherical shells containing a through-thickness defect. *Journal of the Mechanics and Physics of Solids*, 138:103923, 2020.

[200] D. Yang, M. S. Verma, J.-H. So, B. Mosadegh, C. Keplinger, B. Lee, F. Khashai, E. Lossner, Z. Suo, and G. M. Whitesides. Buckling pneumatic linear actuators inspired by muscle. *Advanced Materials Technologies*, 1(3):1600055, June 2016.

[201] W. Yang, T. Fung, K. Chian, and C. Chong. Instability of the two-layered thick-walled esophageal model under the external pressure and circular outer boundary condition. *Journal of Biomechanics*, 40(3):481–490, Jan. 2007.

[202] H. Yuk and X. Zhao. A new 3d printing strategy by harnessing deformation, instability, and fracture of viscoelastic inks. *Advanced Materials*, 30(6):1704028, Dec. 2017.

[203] C. Zener. *Elasticity and anelasticity of metals*. University of Chicago Press, 1948.